THRUST FAULTING ON THE TERRESTRIAL PLANETS: STRUCTURAL AND TECTONIC STUDIES OF MERCURY AND THE COLUMBIA RIVER BASALT PROVINCE

by

KELSEY WARDEN

(Under the Direction of Christian Klimczak)

ABSTRACT

The exterior of a planet often reflects its internal workings. On planets with little to no erosion, the surface geology can record billions of years of planetary evolution. Mercury, the smallest planet in our solar system, has not experienced aqueous erosion and as such, is an ideal site for exploring the longest-lived and most ancient planetary processes. These include global contraction (a decrease in planet volume), tidal despinning (slowing of the planet's rotation), and reorientation (a shift in the orientation of the rotational axis). Each of these processes contributes to stresses that have influenced the tectonic development of structures like faults and folds in the rocks, often basalts, that cover the surface of the planet. On Earth, regional processes are also recorded in local structures. Studying the development of faults and folds is important for understanding the tectonic context of their structural evolution.

Research presented in this dissertation ties together Earth and other-planetary tectonism, deciphering what structures are telling us about planetary evolution. By describing how basalts deform, I relate their deformation to more widespread processes. I present the first quantitative estimates for strain rates from global contraction on Mercury ranging back ~4 Ga, and describe the likely structural style of faulting based on the most detailed tectonic map ever produced of another planet. Results from mapping have also allowed for the constraint of the timing of despinning and reorientation. An investigation of an Earth analogue to these structures, the Yakima Fold Province of central Washington state is also carried out. The structures are represented with a three-dimensional model produced from structural data collected in the field and ~44 km of seismic profile interpretations. Insight into the distribution of deformation across these folds and faults has allowed me to intimately relate the strain observed in the belt to the tectonic setting of the Cenozoic northwest, including the opening of the Basin and Range, subduction of the Juan de Fuca and Farallon plates, and hotspot volcanism in the Snake River Plain.

INDEX WORDS: Planetary tectonics, structural geology, Mercury, Yakima Fold Province, Columbia River Basalt Province, Thrust Fault

THRUST FAULTING ON THE TERRESTRIAL PLANETS: STRUCTURAL AND TECTONIC STUDIES OF MERCURY AND THE COLUMBIA RIVER BASALT PROVINCE

by

KELSEY WARDEN

BS, University of Tennessee, 2012

MS, Purdue University, 2014

A Dissertation Submitted to the Graduate Faculty of The University of Georgia in Partial Fulfillment of the Requirements for the Degree

DOCTOR OF GEOLOGY

ATHENS, GEORGIA

2019

THRUST FAULTING ON THE TERRESTRIAL PLANETS: STRUCTURAL AND TECTONIC STUDIES OF MERCURY AND THE COLUMBIA RIVER BASALT PROVINCE

by

KELSEY WARDEN

Major Professor:	Christian Klimczak
Committee:	Alberto Patiño Douce
	Steve Holland
	Paul Byrne

Electronic Version Approved:

Suzanne Barbour
Dean of the Graduate School
The University of Georgia
May 2019

DEDICATION

For Max

ACKNOWLEDGEMENTS

I am incredibly thankful for the support of my dissertation committee: Dr. Christian Klimczak, Dr. Steve Holland, Dr. Alberto Patiño Douce, and Dr. Paul Byrne. These individuals have advised me, challenged me, and supported me in becoming an independent academic. I am especially grateful to Dr. Christian Klimczak, who I believe I may have put through hell a few times but who has always found a way to calm me down and help me see where I can improve. He has welcomed me as a woman and mother into the sciences without judgement and is a model for how male scientists can be an ally to their female collaborators. Dr. Klimczak has pushed me and helped me grow, and he has respected me when I have pushed back. I am also thankful for the support of Dr. Rob Hawman. Although Dr. Hawman was not on my committee, he has been a constant source of support through the last four years. He has modelled truly great teaching, and shows us all how to stay humble and kind while celebrating our successes.

I also appreciate funding for research and the opportunity to teach provided by the Department of Geology, the Graduate School, and the Freshman College. Thanks also to the Planetary Geology Division of the Geological Society of America for funding my travel to conferences and for providing me leadership experience during my PhD.

This work would not have been possible without the love and support of my friends and family. I would like to thank my parents, Bob and Kim Crane, for believing in me, encouraging me to try new things, and putting up with me as a teenager. I want to thank my sister, cousins, grandparents, aunts and uncles, and in-laws for not making me explain my dissertation too many times, and for loving me for who I am. Thank you to the graduate students who have helped me along the way- in particular, Quentin Anlian, Corbin Kling, Kelly Cronin, Chris Smith, Garrett Brown and Pedro Monarrez. Pedro and Kelly have been remarkable friends who have offered advice and support, and have made a PhD fun. I also want to thank my students for reminding me how important it is to learn and to stay excited about learning.

Finally, I would like to thank my husband and best friend Jayson who has been my rock (no geology pun intended) of encouragement and patience, always putting my dreams first. Without him, I would never have been able to see my way through graduate school. He has had faith in me when I did not, and he has loved me even when I have been (and continue to be) a challenging person. He is the strongest person I know, and I admire him and love him with all my heart.

TABLE OF CONTENTS

LIST OF TABLES

LIST OF FIGURES

CHAPTER 1

INTRODUCTION AND LITERATURE REVIEW

Faulting, the brittle deformation of rock characterized by shear displacement along a planar surface or within a zone (Fossen, 2016), is a common response to stresses that build in the lithosphere of Earth and other planets. Thrust faulting in particular results when the maximum compressive stresses are oriented horizontally and exceed the frictional resistance to sliding of the host rock. Thrust faulting is characterized by the displacement of the hanging wall (rock volume above the fault) above the footwall (rock volume below the fault plane). This process is interpreted to occur on many terrestrial bodies in our solar system including Earth, Mars, the Moon, Mercury, Venus, the moons of other planets, and large asteroids (Strom et al., 1975; Cordell and Strom, 1977; Binder and Gunga, 1985; Crumplet et al., 1986; Watters, 1988, 2010, 2015; Schultz and Watters, 2001; Sperner et al., 2003; Kattenhorn and Prockter, 2014; Buczkowski et al., 2016, among many others). Studying fault subsurface geometry, surface expressions, and growth informs our understanding of planetary geologic evolution. As faulting results from thermal, orbital, and tectonic influences, thrust faulting is a lense for interpreting the internal and dynamic evolution of planets. This dissertation describes the evolution of the planets Mercury and Earth through local, regional, and global analyses of thrust faulting.

Thrust fault-related landforms are often characterized by linear, elevated topography and fault surface breaks. Dimensions of elevated topography can be measured using Digital Elevation Models (DEMs) and imagery collected from spacecraft. Based on comparisons to similar landforms on Earth (example shown in Figure 1), these other-planetary landforms are interpreted to represent crustal shortening. Earth analogues are established based on similar topographic, morphologic, or geographic characteristics. The geologic structures— faults and folds— that produce observed morphology and topography of analogues are often applied in modeling efforts to describe the formation of thrust fault-related landforms (e.g. Plescia and Golombek, 1986; Watters, 1988; Mège and Reidel, 2001; Watters, 2004).

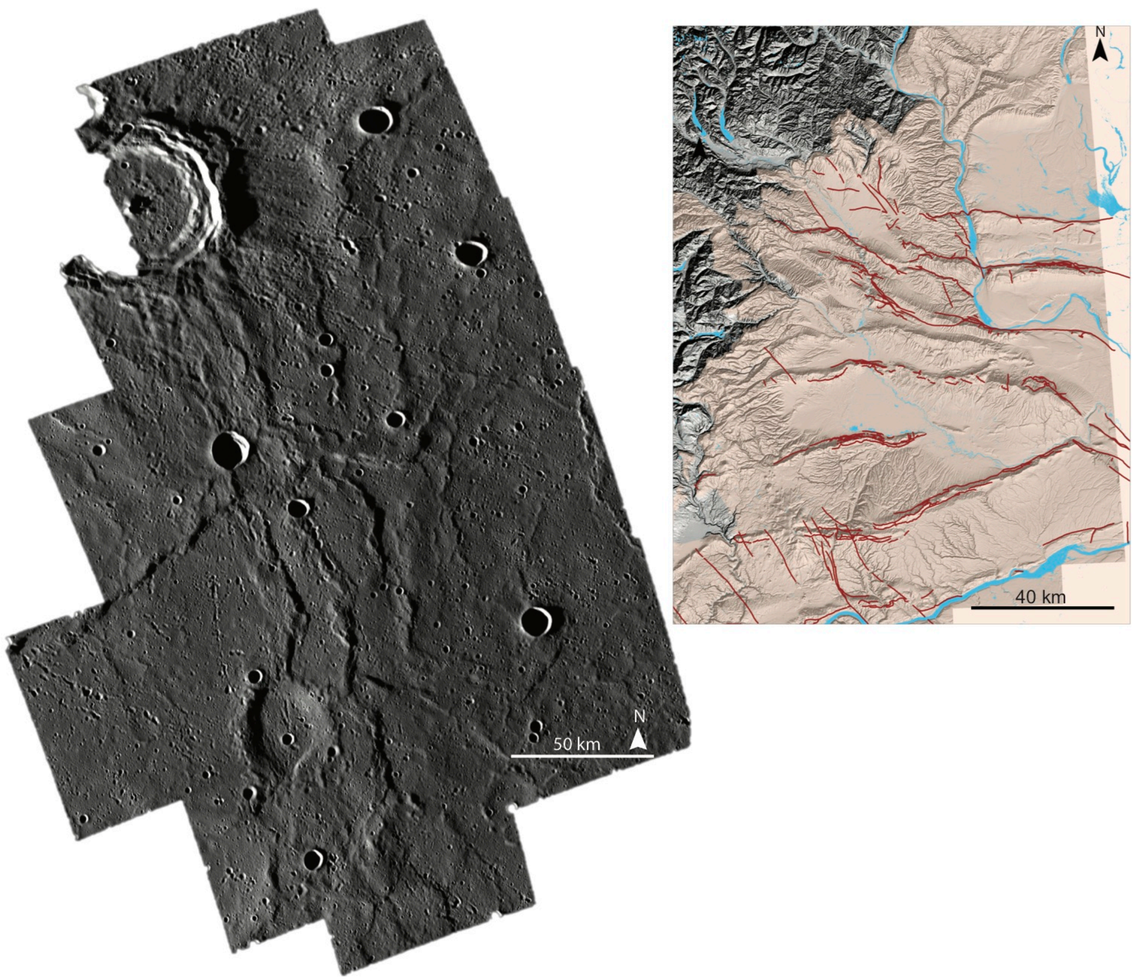

Figure 1.1 Imagery (left) and a hillshade (right) of fold provinces illustrate similarities between parallel, linear thrust fault-related landforms on Mercury (left) and Earth (right). La Dauphine Rupes (left) is a series of thrust fault-related landforms in a flood basalt

province in Mercury’s northern hemisphere. This image was created from orthographically projected Mercury Dual Imaging System imagery (166 m/pixel) centered at 68° N, 28° E. The Yakima Fold Province (right) is a series of mostly north-verging anticlines in the Columbia River Flood Basalt Province in south-central Washington State. This 10-meter digital elevation model shows highlights the parallel ridges as well as active Quaternary faults (crimson) and extent of flood basalts (blue).

Most studies of extraterrestrial thrust faulting aim to describe the geometry of faults. These works typically use finite element models to demonstrate how a wide range of geometric fault parameters such as depth and dip reproduces observed topography and morphology of landforms interpreted to be underlain by thrust faults (e.g. Schultz, 2000; Watters, 2004; Okubo and Schultz, 2004; Banks et al., 2012). Parameters determined from these models are then applied with topography to measure displacement and calculate the ratio of displacement to length for faults (Watters et al., 2000; Schultz et al., 2006; Grott et al., 2007; Klimczak et al., 2018). This ratio and the pattern of displacement across the fault can provide information about fault growth, fault linkages, and the mechanical stratigraphy of the host-rock. Fault parameters are also used to describe planetary thermal parameters (e.g. Grott et al., 2007) and estimate global contraction, the negative volumetric change a planet undergoes during extensive cooling (e.g. Watters et al., 2004; Byrne et al., 2014). Other studies focus on the geographic arrangements of thrust-fault related landforms. They analyze the spatial distribution and orientation of mapped landforms, and then compare observations to models which predict tectonic patterns resulting from geologic, thermal, and orbital phenomena (Chicarro et al., 1985; Bilotti and Suppe, 1999; Watters et al., 2015).

In this work, I expand on these studies by generating and investigating global datasets of thrust fault-related landforms and analyzing Earth analogues in detail. The results of this dissertation include describing the timing and rate of global contraction on Mercury, interpreting the style of tectonics on Mercury through comparison to Earth analogues, describing the regional map patterns of thrust fault-related landforms in the Northern Smooth Plains volcanic units on Mercury, and developing a structural model of an important Earth analogue. Chapter 2 provides the first quantitative estimates for strain rates due to global contraction on Mercury. Chapter 3 uses high resolution mapping to describe tectonics on Mercury as thin-skinned, similar to shallowly rooting fold and thrust belts on Earth. Chapter 4 demonstrates how the distribution of displacement on fault surfaces can illustrate multi-stage deformational histories and how the topography of thrust fault-related landforms can be explained through multiple faults at varying depths.

Chapter 2 Overview

All planets loose heat over time. Cooling causes planetary contraction, commonly referred to as global contraction. If a lithosphere, the mechanical shell of the planet, has developed, global contraction is recorded through the formation of thrust faults. Mercury has experienced cooling and global contraction (Solomon, 1977), and thrust fault-related landforms have been mapped (Watters et al., 2004; Byrne et al., 2014). Global contraction is expected to produce a global population of randomly oriented thrust faults (Melosh and Dzurisin, 1978). Although many studies have recognized that the global population of faults on Mercury may not be random (e.g. Dombard and Hauck, 2008), these faults are still assumed to have primarily originated due to global contraction. A global map of thrust fault-related landforms was used to estimate the amount of radius change that has occurred on Mercury, 3.1–7.1 km (Byrne et al., 2014).

Thermal evolution models (Hauck et al., 2004, Grott et al., 2011; Tosi et al. 2013) and geologic observations (Banks et al., 2015) have been used to estimate when contraction began. Thermal models in particular produce a wide range of solutions for onset and rate of global contraction, as prior to research presented in Chapter 2, geological observations had not constrained these models. We used a global database of impact craters (Spudis and Guest, 1988; Kinczyk et al., 2016) to describe the stratigraphic relationships of craters and thrust fault-related landforms. Each crater in the database had been assigned an age based on its morphology (Kinczyk et al., 2016). Assessments of a total of 6000 of such stratigraphic relationships allowed me to assess geometric probabilities of craters being cut by faults. With knowledge of the different degradation stages of these craters that have previously been tied to time-stratigraphic systems (Kinczyk et al., 2016), I determined the amount of planetary radius change accommodated by faults cutting each age group of craters during each of Mercury's time systems. This not only helped determine the onset of global contraction, but allowed me to calculate the total radius change per time system, and to convert this value to a global strain rate.

These results are the first to quantitatively describe global strain rate through time on Mercury. I calculated that faulting due to global contraction began during Mercury's third time system, the Calorian, and that although strain rates were initially high, they have slowed toward present day. The results of this analysis are important for constraining thermal models of planetary evolution, and the original methods can be applied to other planetary bodies in the future.

Chapter 3 Overview

I recognized through observations of many thrust fault-related landforms in Chapter 2 that global contraction was likely not the only process motivating the formation of thrust fault-related landforms on Mercury. I investigated which other processes influenced the formation of these landforms by generating and analyzing a detailed map of fault-related landforms in the Northern Smooth Plains. This map allowed me to address important questions related to the style and geometry of faults and other structures on Mercury. I mapped ~4,900 thrust fault-related landforms at 1:1,000,000 scale in the Northern Smooth Plains, a smooth, dark flood basalt unit covering 7% of the planet's surface (Head et al., 2011; Ostrach et al., 2015). Surface breaking faults and anticline crests were mapped using ArcGIS and organized into 20° longitude by 20° latitude bins. Orientations and density of structures were calculated for each bin. The map patterns and morphology of these landforms were also described and compared with Earth analogues.

Six common landform map patterns were described: (1) thrust fault-related landforms following the boundary of volcanically flooded impact craters, (2) sigmoidal rises bounded by fault-related landforms, (3) V-shaped rises composed of two landforms terminating at a single sharp point, (4) broad arcuate rises of nearly equal width, (5) parallel, evenly-spaced ridges, and (6) landforms showing alternation in direction of tectonic transport along strike. Earth analogues to these landforms are characterized by faults that extend only to near surface décollements, and thus the tectonic style is referred to as “thin-skinned”. Results also suggest that there are no systematic patterns in density of landforms in the Northern Smooth Plains, but that there are important latitudinal patterns in landform orientation. Landforms near the north pole are more likely to be oriented East–West, while landforms nearer to the equator are more likely to be oriented North–South. While traditionally this pattern has been attributed to the process of tidal despinning (Pechmann and Melosh, 1979), the slowing of the planet’s rotation due to changes in its orbit, other authors have found that this process would have only produced jointing near the poles (Klimczak et al., 2015) without some additional stress to overcome the frictional resistance to sliding or increased pore pressure from magma. This analysis provides the first quantitative evidence of a non-random global tectonic fabric on Mercury.

Chapter 4 Overview

In comparisons to Earth analogues in Chapter 3 research, the Yakima Fold Province (YFP) of south-central Washington was often referenced as an important analogue site (e.g. Plescia and Golombek, 1986; Watters, 1988). These equally spaced, asymmetric ridges deform the Columbia River Flood Basalts (Reidel, 1984), and thus share morphologic characteristics and geologic setting with thrust fault-related landforms on Mercury. However, open questions about the tectonic context that lead to the growth of structures in the YFP, timing of their uplift, and structural geometry within the ridges produce doubt in the analogy between these and other-planetary landforms.

The study of these landforms is important for societal and other scientific reasons. Faults within the YFP surround the Hanford Nuclear Site and likely extend as part of a regional fault network toward the Seattle-Puget Sound area (Blakely et al., 2011; Pratt, 2012; Sherrod et al., 2016). Studying the structures of the YFP, particularly the deep, ancient structures and their connection and contrast to more shallow, modern structures, allows us to describe how this tectonic environment has changed overtime. Deep structures provide insight into the clockwise rotation of the Pacific Northwest, connecting the compressional tectonic regime of the YFP to the extensional tectonic environment of the northern Basin and Range (Wells and McCaffrey, 2013; McCaffrey et al, 2013; 2016). I developed a three-dimensional model of the structures in one YFP ridge so that geometry and timing of uplift could be analyzed in greater detail.

The Saddle Mountains is a 110 km-long East–West striking anticline in the northern region of the YFP. I interpreted 44 km of seismic profiles crossing or near the Saddle Mountains, and collected 384 structural orientation measurements in the field. I also gathered stratigraphic data from geologic maps and 13 well logs. Three wells were greater than 4 km deep. I used this data to construct 10 balanced cross sections, and interpolated across the cross sections to produce 3D representations of the tops of volcanic horizons and four major fault surfaces. These folded horizons and faults were used to deconstruct the deformation represented in the structures of the ridge. I calculated strain due to faulting and folding and the direction of that strain.

The two most prominent faults were sub-parallel, listric faults shallowing to 4 km and 8 km depth. Relatively horizontal strata separate these two faults. The deeper fault displays increased displacement to the west, while the more near surface fault shows deformation increased in the center of the study area. These results indicate the YFP development is related to the clockwise rotation of the North American plate, with the deeper thrust representing early deformation associated almost solely with block rotation and the upper thrust representing more northward directed deformation. These results not only allow for future modeling of other-planetary structures, but they also place the YFP in the context of the more regional history of deformation in the Cenozoic Northwest.

Expressions of Thrust Faulting and Folding

Thrust faults accommodate brittle shortening. They are often recognized at the surface by the juxtaposition of older rock units above younger rock units and increased topography due to folding or bending of the shortened surface (Fossen, 2016, Figure 1.2A). The morphology of the topography associated with faulting is affected by physical characteristics of faults and folds. Fault dip, depth, geometry, relationship to other faults and reactivation vary with tectonic setting and produce differing subsurface geometry and surface topography.

Anderson's theory of faulting (1951) states that thrust faults form in tectonic regimes where the maximum compressive principal stresses are oriented horizontally and the minimum compressive principal stresses are oriented vertically, such that such structures propagate at a 30° angle to a horizontal plane. This means that they are typically observed as shallowly dipping faults. The fault plane may not be a simple plane dipping 30°, but rather be divided into ramps and flats. Ramps are fault surfaces that are characterized by dips greater than zero degrees, and flats are fault surfaces that propagate horizontally. A simple fault plane may be conceptualized as a fault composed of one ramp or one flat.

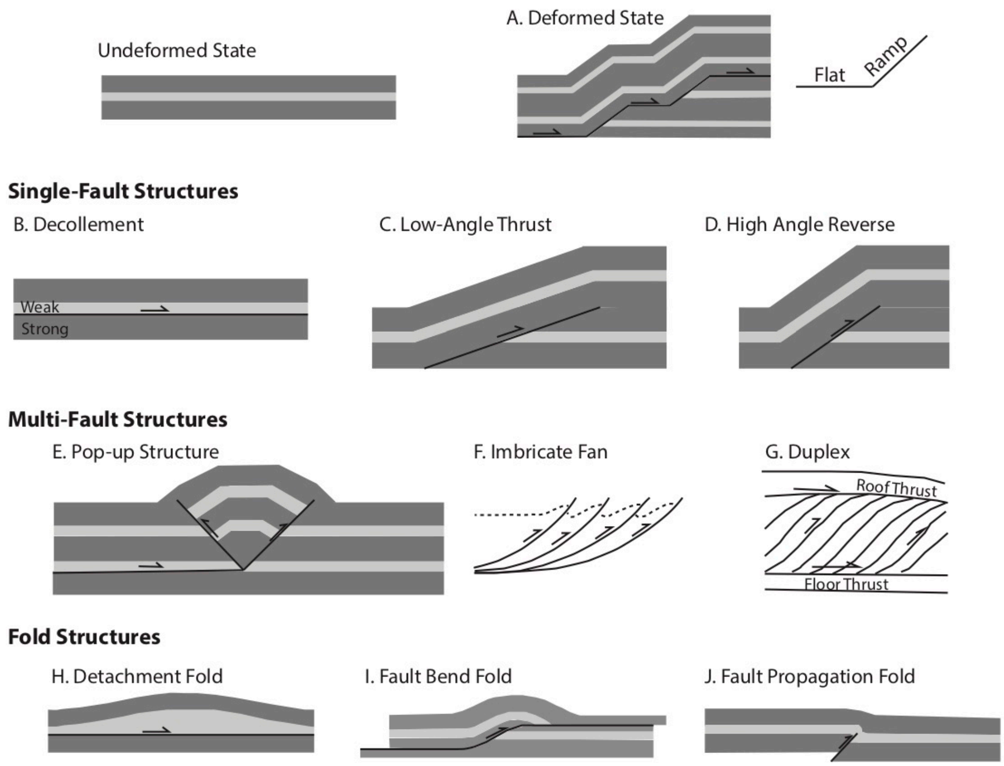

Figure 1.2 This figure shows the geometry of single-fault structures, multi-fault structures, and fold structures. In each case, the geometry and characteristics of the fault(s) affect the geometric properties of the deformed strata. These diagrams are modified from (Boyer and Elliot, 1982; Butler, 1982; and Brandes and Tanner, 2014).

Thrust faults composed of one flat or very shallowly dipping ramp are called décollements (Figure 1.2B). Décollements develop when faulting preferentially occurs in a weak rock layer above a more competent stratum. Horizontal compressive stresses and continuity of the weak layer encourage the fault to continue to propagate horizontally, and can result in the lateral transport of rock units several kilometers. For example, new faults in the toe of fold and thrust belt forelands propagate upward from basal décollements (Dahlen et al., 1984). Weak layers that act as hosts for décollements include sedimentary sequences above crystalline basement (ex. Cordilleran foreland, Price and Fermor, 1985) and evaporite deposits, where the friction between layers of cover and basement is reduced (Costa and Vendeville, 2002). When these layers are also weaker than the overlying stratum, décollement folding, also called detachment folding, may develop (Costa and Vendeville, 2002, Dahlstom, 1970, Figure 1.2H). As deformation along the fault continues, the folds or buckles in overlying competent strata increase in wavelength and amplitude (Mitra, 2003), and the voids between the waveforms and décollement fill with less competent rock materials from the décollement layer (Costa and Vendeville, 2002).

When thrust faults are mainly composed of a single, shallowly dipping ramp (< 45°), they are referred to as low-angle thrust faults (Figure 1.2C). These faults may not originate as shallowly dipping planes, but instead only follow weak zones in less competent strata and propagate upward through more competent strata. Low-angle thrusts preferentially propagate through weak layers and will only propagate upward in short jumps. Collectively, this combination of short ramps and long flats results in a shallowly dipping fault plane or zone (King, 1960). If the fault steepens as it nears the surface, the fault geometry is referred to as listric (Cardozo and Brandenburg, 2014).

Thrust faults that dip at high angles are called reverse faults (Figure 1.2D) and are not predicted by Anderson’s theory of faulting (1951). These faults may represent the reactivation of normal faults in shortening tectonic regimes (Williams et al., 1989), transpression across initially strike-slip faults, or steepening of thrust sense in shear zones (Sibson et al., 1988).

Reactivation is typically associated with a change in tectonic regime, but changes in pore fluid pressure and decreases in friction along the fault plane can also contribute to changes in the sense of fault slip (Sibson et al., 1988; Smith et al., 2017). For example, faults with longer histories of fault activity tend to develop smoother surfaces and more developed fault zones, making them more easily reactivated (Kelly et al., 1999). Deeper faults may also be more likely to be reactivated if the stresses driving faulting originate in the basement rock. Fluid flow is also a preferred condition for reactivation (Sibson, 1995), as it indicates a higher degree of fault connectivity and it reduces the normal and shear strength of the rock (Kelly et al., 1999; De Paola et al., 2006). Graben, linear depressions formed by two oppositely dipping normal faults, may also be reactivated when horizontal compressive stresses rotate perpendicular to the graben trend (Brun and Nalpas, 1996). On a larger scale, basin inversion also reactivates normal faults with thrust senses of slip. Antithetic normal faults, minor faults with opposite senses of slip from the master fault, typically exhibit more shallow dips and therefore may be more likely to be reactivated and result in domino block rotation (Buchanan and McClay, 1991; Alder et al., 2016).

Reactivated graben are often called pop-up structures (Figure 1.2E) , but this term also refers to zones of transpression in strike-slip regimes. The stepover region between two strike-slip faults may produce a flower structure, a positive topographic landform resulting from the upward propagation of steep thrusts with opposing senses of vergence. A change in strike of a strike-slip fault may also result in some thrusting motion and positive topographic relief expressed as a restraining bend (McClay and Bonora, 2001; Schellart and Nieuwland, 2002).

Although the dip of a thrust fault may imply an aspect of its tectonic history, the connection or linkage between multiple thrust faults also places the fault within its tectonic setting. High rheologic contrasts between basement rock and more surficial rock units encourage the development of décollements (Bauville and Schmalholz, 2015). As slip continues along a décollement, successive ramps may propagate upward toward the foreland resulting in repeated sequences of tilted strata back toward the hinterland (Shaw et al., 1999). This series of faults and their associated folds is referred to as a fold and thrust belt. When each of these faults roots into the same décollement, the belt is also called an imbricate fan (Pfiffner, 1993, Figure 1.2F), and when a thrust fault connects the upper surfaces of faulted units (a roof thrust), the series is referred to as a duplex (Figure 1.2G. The blocks of rock bounded by faults are called horses (Coward, 1983).

Multiple fault surfaces may also connect in the transition zone between fold and thrust belts and foreland basins. Vertically stacked horses produce duplexes above the lower décollement, and when horses alternate vergence, faulting towards the hinterland and foreland, the total structure builds in amplitude and width (Stockmal et al., 2001). These duplexes may be internally folded, and may be present on multiple scales in the foreland (Tanner et al., 2010). These structures are called triangle zones and require that the upper thrust verges away from the foredeep, toward the hinterland (Stockmal et al., 2001).

Folding style is often indicative fault characteristics. Fault-bend folding and fault-propagation folding are both common types of folds observed in relation with thrust faults. A fault-bend fold results when a fault block moves over a non-planar surface (i.e. at least one ramp and one upper flat, Figure 1.2I). Horizontal strata are translated parallel to the ramp surface, and turn back toward the horizontal where they continue to translate toward the foreland along a flat. This results in an anticline or anticlinal stack (Suppe, 1983). Fault-propagation folding occurs when at least one ramp is present without an upper flat (Figure 1.2J). The lack of an upper flat restricts the slip at the fault tip (Suppe and Medwedeff, 1990). Horizontal strata translated parallel to the ramp surface turn sharply toward the horizontal and do not continue to translate toward the foreland. This results in steep or overturned forelimbs and more gently dipping back limbs. The ratio of the ramp length to the flat length determines the asymmetry of fold limbs. Thus, mature fault-bend folds tend to be more symmetric than fault-propagation folds (Suppe, 1983).

Thrust Fault-Related Landforms on Other Planets

The inability to perform fieldwork on other planetary bodies has limited investigations of structures to morphologic descriptions of landforms and their comparisons to terrestrial analogues (e.g. Plescia and Golombek, 1986). Two types of thrust-fault related landforms have been observed on many solar system bodies including Mercury, the Moon, and Mars: lobate scarps and wrinkle ridges. Although the structural interpretation of these landforms is different, no study has ever quantified the differences between the groups, and often these landforms are observed transitioning into one another (Watters and Nimmo, 2010; Byrne et al., 2018; Crane and Klimczak, 2019).

Lobate scarps are linear to arcuate, asymmetric ridges interpreted to be the geomorphologic expressions of surface-breaking thrust faults (Strom et al., 1975; Watters et al., 2010; Egéa-Gonzalez et al., 2012; Banks et al., 2012; Watters et al., 2015). Modeling studies have estimated the dip of these faults to vary between 20° and 35° and the depth to extend to the base of the lithosphere (Watters et al., 2000; Watters et al., 2002). These parameters are derived from models of lobate scarps (Schultz and Watters, 2001), which estimate fault dip and depth based on iterative attempts to reproduce surface topography by translating the rock mass along the fault surface. On Mercury, the formation of lobate scarps has been primarily attributed to global contraction (Watters et al., 2004).

Wrinkle ridges exhibit far more variability in morphology than lobate scarps. These landforms are observed as linear to anastomosing, asymmetric to symmetric ridges. Unlike lobate scarps, wrinkle ridges are proposed to result from a combination of folding and faulting in surface units (Schultz, 2000; Golombek et al., 2001), and may involve multiple surface-breaking and blind, non-surface-breaking (Thompson, 1981), thrust faults (Plescia and Golombek, 1986; Watters, 1988; Schultz, 2000; Walsh et al., 2013). Wrinkle ridges may result from global contraction (Byrne et al., 2014), but also may relate more directly to localized processes such as subsidence in volcanic plains (Watters, 1993). As such, faults associated with wrinkle ridges are often proposed to extend only shallowly into the lithosphere, possibly soling into décollements (Alleman and Thomas, 1992; Mangold et al., 1998; Okubo and Schultz, 2004; Watters, 2004).

Significance

The faults on the surface of a planet record the history of stresses in its lithosphere, stresses that result from a multitude of processes, each of which leaves a signature of its magnitude, orientation, and location upon the morphologic expression of those faults. This dissertation explores the connection between those processes, their timing, and rates, and the thrust-fault related landforms they produce on Mercury and Earth. The research presented here describes planetary evolution through the lense of tectonics and thrust faulting, and enhances our understanding of the ties between internal and external planetary processes.

Chapters 2 and 3 specifically address thrust faulting on Mercury. In Chapter 2, we derive the timing and rate of global contraction on Mercury. Global contraction is a fundamental process that operated throughout the planet's geologic history, and in Chapter 3, we investigate in detail how this process and other global processes have been expressed in thrust faulting at Mercury's surface. We describe the geometry of these faults, and find fault geometry to be intimately tied to a shallow décollement surface. In Chapter 4, we describe fault and fold geometry of an Earth analogue to these landforms in the Yakima Fold Province on Earth. Collectively, these studies help us describe the architecture of thrust faulting in flood basalts, and present fault geometry as a property of deformation that can be inherited through time.

CHAPTER 2

TIMING AND RATE OF GLOBAL CONTRACTION ON MERCURY[1]

[1]Crane, K.T. and C. Klimczak. 2017. *Geophysical Research Letters*. 44:3082-3089.
Reprinted here with permission of the publisher.

Abstract

Impact bombardment and global contraction due to planetary cooling have both shaped the surface of Mercury over very long time scales. Landforms associated with these processes, i.e., impact craters and thrust fault-related escarpments, and their mutual geologic relationships were analyzed to gain insight into the temporal relationships between the two. We assess stratigraphic relationships of ~6000 thrust fault-related landforms with all 20-km-diameter and larger craters to statistically evaluate the timing and rate of contraction on Mercury. Geometric probabilities were computed for thrust faults cross-cutting craters of different degradation stages that correspond to different time-stratigraphic systems, which allow determination of the onset and time derivative of global contraction. Results show that this process had begun after the late heavy bombardment of the inner solar system and likely gradually slowed toward the present. Implications arise for thermal history models as well as slip rates and quake recurrence intervals along thrust faults on Mercury.

Mercury's Record of Craters and Thrust Faults

Thrust faulting caused by planetary cooling and associated global contraction (Solomon, 1977) and impact cratering (Morbidelli et al., 2012; Marchi et al., 2013) are two processes that have modified Mercury's surface throughout much of its geologic past. Thrust faulting is known to produce positive-relief linear to arcuate ridges. More than 6000 such landforms have previously been mapped and, when related to a given set of subsurface fault geometries, are estimated to accommodate a 3.1 to 7.1 km planetary radius decrease (Byrne et al., 2014). Thrust fault activity caused by global contraction on

Mercury was found by both thermal modeling and geologic studies to have begun by or near the end of the late heavy bombardment (LHB) of the inner Solar System (Hauck et al., 2004; Tosi et al., 2013; Banks et al., 2015a).

The slow and incremental development of relief associated with thrust faults stands in stark contrast to the nearly instantaneous formation of impact craters. During and before the LHB, the vast majority of Mercury's craters and basins formed, with fewer large craters emplaced in recent times (Morbidelli et al., 2012). While the well-studied cratering record and rate on the Moon (e.g. Trask, 1967) have motivated investigations into cratering fluxes (Strom and Neukum, 1988; Marchi et al., 2013) and crater morphology (e.g. Trask, 1971; Trask and Guest, 1975; Spudis and Guest, 1988) the onset and especially the rate of global contraction have not been approached with such rigor. However, results of thermal evolution models produce a wide range of solutions for contraction amount, onset, and rates (e.g. Hauck et al., 2004; Grott et al., 2011; Tosi et al., 2013) that can be compared to geologic observations. Using MErcury Surface, Space, ENvironment, GEochemistry, and Ranging (MESSENGER) data, we establish and statistically investigate stratigraphic relationships of impact craters and basins with all detected thrust faults to deduce the timing and rate at which global contraction operated throughout Mercury's geologic history. These results are then used to calculate variations in contraction rate over time that have acute implications for thermal models.

Craters and Mercury's stratigraphy

Mercury's craters vary in size and morphology, ranging from large, heavily degraded basins to small, morphologically crisp craters. This observation has led to categorization of impact structures into five morphologic classes since the return of

Mariner 10 images (Wood et al., 1977; McCauley et al., 1981; Barnouin et al., 2012). Recently, Kinczyk et al. (2016) categorized all craters greater than 40 km in diameter using MESSENGER data. Their classification scheme closely followed that described by Spudis and Guest (1988) in which craters belonging to classes 1 and 2 are the most degraded, with discontinuous rims and many superposing craters (Figures 1a,b). Class 3 craters show slumped wall terraces, central peaks, and fewer superposing craters (Figures 1c,d), class 4 craters have well defined peaks and slightly degraded rim crests and terraces (Figures 1e,f), and class 5 craters, the least degraded of all craters on Mercury, have the same characteristics as class 4 craters, but also display rays and lighter colored ejecta (Figure 1g). These five classes are generally interpreted to coincide with Mercury's five time-stratigraphic systems: (1) the Pre-Tolstojan (> ~ 4 Ga), (2) Tolstojan (~ 4 - 3.9 Ga), (3) Calorian (3.9 − ~3.5 to 3 Ga), (4) Mansurian (~3.5 to 3 Ga − 1 Ga), and (5) Kuiperian (< 1 Ga) (Spudis and Guest, 1988), but recent investigations found that there may be greater variability in the absolute ages of these systems than previously established (Braden and Robinson, 2013; Banks et al., 2016).

Stratigraphic relationships of craters with thrust faults

We conducted a geospatial analysis to locate where thrust faults and craters showed stratigraphic relationships and distinguished between craters that are cut by faults and those that superpose faults (see supplementary materials for details). Craters cut by faults (Figures 1a,c,e) must have been emplaced before or at a time of active thrust faulting, whereas craters superposing faults (Figures 1b,d,g) supersede thrust fault activity at that location. The oldest superposing craters mark the earliest evidence for thrust fault activity and thus provide a lower bound for the onset of global contraction.

Importantly, faulting is a long-lived, periodic process (Cowie and Scholz, 1992) and so a fault deforming a Tolstojan crater, for example, may have developed as early as the Tolstojan, but could have formed or accommodated strain during any subsequent period as well. Thrust fault-related landforms could have also existed prior to the impact event and may have partly or entirely been erased by the cratering process. But the age of a crater deformed by a fault nevertheless provides information on the time during or after which the fault was active, irrespective of whether some portion of that fault could have existed prior to the impact event.

Kinczyk et al. (2016) mapped craters as small as 20 km and classified craters with diameters greater than 40 km. We classified the 20 to 40 km-diameter craters that displayed stratigraphic relationships with faults using global MESSENGER image mosaics. From a total of 3112 craters and basins ranging from 20 to 2000 km in diameter, 2310 structures were categorized into classes 1 and 2 (Kinczyk et al., 2016), placing their formation likely during or before the Tolstojan (Spudis and Guest, 1988). Of this combined subset of craters, 1196 were spatially correlated with faults, with 1192 cut (Figure 1a), and four interpreted to be superposing faults (Figure 1b). The combination of a rapid early cratering rate with so few fault-superposing craters indicates that most faults formed after these craters were emplaced and thus that thrust faulting may have been active but was likely not a planet-wide process before and during this time-stratigraphic system. Among 536 identified class 3 craters, 370 craters were spatially associated with faults, where 266 were cut (Figure 1c) and 104 superposed faults (Figure 1d). Class 3 craters are widely thought to have been emplaced during the Calorian, and the number of fault-superposing class 3 craters shows that a substantial amount of faulting must have occurred prior to the emplacement of craters of this class. This relationship indicates that thrust faulting was well underway during this time-stratigraphic system and so marks an increase in contractional tectonic activity following the Tolstojan. Of 244 identified class 4 craters, 104 were associated spatially with faults, where 49 were cut by (Figure 1e) and 55 superposed faults (Figure 1f). Craters with such morphological characteristics are thought to have been emplaced during the Mansurian. Because over half of these craters superpose faults, substantial faulting must have occurred before the end of the Mansurian, with some faulting potentially occurring after. The increasing proportions of craters superposing faults indicate that global contraction, although active during the Mansurian, had likely slowed. The influx of large impactors had also decreased by this time, so relative percentages of stratigraphic relationships are used in our analysis instead of absolute counts (further discussed in section 2: Timing of Thrust Faulting). Of 22 identified class 5 craters only three were associated spatially with thrust faults; all of them superposed a fault (Figure 1g). With a low impact flux during the Kuiperian, the time-stratigraphic system during which class 5 craters are thought to have been emplaced, it is statistically unlikely that craters of this category would be associated spatially with a fault. Given the numerical relationship of these craters to faults, however, thrust fault activity induced by global contraction was low across Mercury’s surface during this system. These relationships agree with a previous, qualitative assessment of stratigraphic relationships of craters and thrust faults (Banks et al., 2015a).

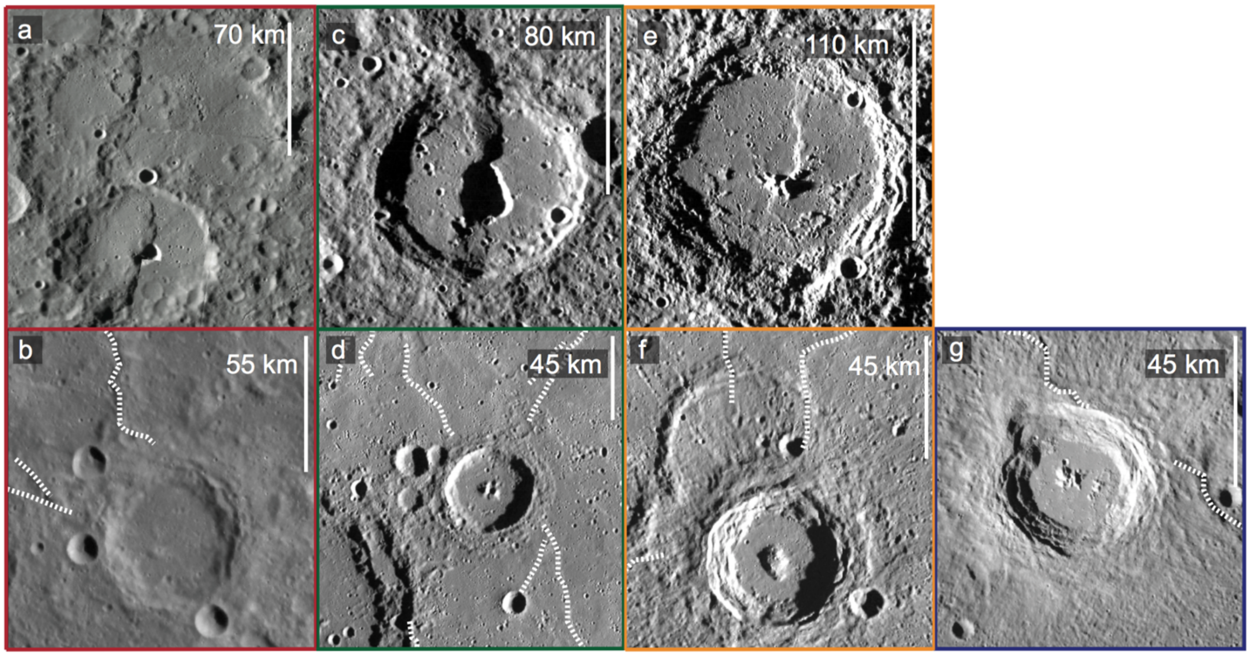

Figure 2.1 Stratigraphic relationships between faults and craters include craters cut by faults and craters superposing faults. (a) Tolstojan crater “Rumi” centered at 105° W, 24° S superposing an unnamed Pre-Tolstojan crater. Sometime after emplacement, both craters were cut by Palmer Rupes. (b) An unnamed Tolstojan crater centered at 53° E, 40° S potentially superposing three degraded thrust fault-related landforms. (c) The Calorian crater “Geddes” located at 30° W, 27° N cut by Antoniadi Dorsum. (d) An unnamed Calorian crater superposing a thrust fault-related landform located at 17° E, 45.5° N. (e) Mansurian crater “Ts'ai Wen-Chi” located at 23° W, 23 ° N cut by an unnamed thrust fault-related landform. (f) and (g) are unnamed Mansurian and Kuiperian craters centered at 13° E, 49° N, and 65° E, 48° N, respectively, superposing unnamed thrust fault-related landforms. Degradation stages of all craters shown here were

classified originally by Spudis and Guest (1988) and most recently by Kinczyk et al. (2016).

Timing of Thrust Faulting

The thrust fault-related landforms superposed by craters cannot be younger than the craters themselves, providing evidence that global contraction was underway at the time such craters formed. Out of a total population of 2310 preserved craters likely emplaced during and before the Tolstojan, we located only four craters that we interpret to superpose faults. Such a small number of craters indicates that although fault activity potentially predated the crater formation and thus occurred within this time system, the activity only occurred in isolated localities. Arguably, evidence for Pre-Tolstojan and Tolstojan thrust fault-related landforms and their stratigraphic relationships with craters — if present — may have been erased from the geologic record. But given that large fault-related landforms likely degrade at rates comparable to crater rims and the large number of preserved crater rims from that time, it is unlikely that only four such relationships were preserved if faulting had been a widespread and active process during and before the Tolstojan. The much higher number of fault-superposing craters in the Calorian instead indicates that thrust faulting and thus global contraction was well underway during this time-stratigraphic system. Prior to the onset of thrust faulting, however, the lithosphere likely elastically supported an initial radius decrease from cooling of up to 2.1 km (Klimczak, 2015), showing that global contraction was likely initiated prior to the Calorian already.

We statistically verified that the geographic distribution of craters across Mercury is similar throughout each time system and evaluated the geographic distribution of thrust fault-related landforms with a Bootstrap (repeated cluster) analysis (see supporting information). Tidal despinning and variations in crustal thickness may produce a non-random (clustered) fault distribution (Watters et al., 2015). Our analysis identifies a uniform distribution of thrust fault-related landforms with clusters only present in Mercury's smooth plains units. Faults within these clusters do not form enough stratigraphic relationships with craters to significantly impact our results (see supplementary materials). For a uniformly distributed population of thrust faults, one would expect that the population of craters present at the onset of global thrust fault activity would be more or less equally affected by the faults and that different sub-populations of craters would display that same relationship. The ratios of cut craters to total craters emplaced during the Pre-Tolstojan, Tolstojan, and Calorian systems are 0.53, 0.50, and 0.49, respectively. The ratios drop noticeably for the Mansurian (0.2) and Kuiperian (0). These numbers reflect that the first three populations of craters were likely exposed to the same degree of faulting, showing once more that thrust faulting likely began during the Calorian. The decrease in these ratios for the Mansurian and Kuiperian systems indicates that a substantial amount of the fault activity had already occurred before these time-stratigraphic systems, with the Kuiperian being tectonically quiet (supported in more detail in section 3: Strain and Strain Rate). Evidence for local, small-scale thrust fault activity, however, was interpreted to have occurred during the Kuiperian to as recent as 50 Ma ago (Banks et al., 2015a; Watters et al., 2016), but as our statistical analysis focuses on craters with diameters of 20 km and larger, any small-scale fault activity is not captured with our approach.

Strain and Strain Rate

Strain is a measure of deformation of an object relative to its original size. For a contracting planet, the term refers to its radius change compared to the radius of the planet prior to contraction. The permanent, brittle strain Mercury's lithosphere experienced from global contraction was accommodated by many thrust faults. For a geographically uniformly distributed population of faults (see supporting information), larger and older craters have greater probabilities of being spatially associated with thrust faults. For example, Pre-Tolstojan and Tolstojan craters, which have been exposed on Mercury's surface for billions of years, and thus they have a much greater probability of being spatially associated with thrust faults than younger, generally smaller Mansurian or Kuiperian craters.

Stratigraphic relationships between craters and faults are determined by geometric probabilities and are a function of the cratering rate and the strain accommodated by faults over time. To account for the cratering rate, we calculated the areas associated with craters of each of the systems (see supporting information). As crater degradation stages are generally correlated with Mercury's stratigraphic systems (Spudis and Guest, 1988), only classes 1 and 2 craters would have been present prior to the Calorian, and by the end of the Calorian all class 3 craters were emplaced. Preserved craters emplaced in the Pre-Tolstojan and Tolstojan occupied an area 4.62 times larger than that covered by Calorian craters. By the end of the Mansurian, all class 4 craters were emplaced and Calorian craters covered 3.25 times as much area as Mansurian craters, with the area ratio of Pre-Tolstojan/Tolstojan to Calorian craters being 4.60:1. This ratio is lower because craters emplaced in the Mansurian covered more area on Pre-Tolstojan and Tolstojan surfaces than on Calorian surfaces. At present, where class 5 craters are added to the total crater population, the Mansurian to Kuiperian crater area ratio is 19.15:1, the Calorian to Kuiperian crater area ratio is 62.31:1, and the Pre-Tolstojan/Tolstojan to Kuiperian crater area ratio is 286.53:1. The ratios of areas with respect to the Kuiperian result from the small size and frequency of craters in this time-stratigraphic system.

The crater area ratios provide a measure of the likelihood for a thrust fault population active during a given time-stratigraphic system to also have accommodated strain in craters that were already emplaced during any of the preceding systems. As impacts erase any pre-existing landforms, the strain expressed by a thrust fault-related landform inside a crater must have entirely been recorded after the crater was emplaced. Because we assume that crater area ratios are mostly consistent with global terrain ratios, they allow the calculation of the geometric probabilities for thrust faulting to accommodate strain within terrain associated with each of the time-stratigraphic systems. Combined with the previously established stratigraphic relationships, they then permit us to calculate the rate at which thrust faulting accommodated global contraction through time.

Out of the total population of studied craters, about 38% of Pre-Tolstojan/Tolstojan, 8.5% of Calorian, 1.5% of Mansurian, and 0% of Kuiperian craters are cut by thrust faults. These sub-populations of faults have the same slopes in their cumulative length distribution to one another and to the total fault population (see supporting information). This finding indicates that, despite differences in the absolute fault count in each of the fault sub-populations, each of the crater sub-populations is associated with the same ratio of small to long faults, so that the above percentages may be directly related to the strain accommodated within the cratered areas. Statistically, this means that 79.10% of the total population of thrust fault-related landforms mapped by Byrne et al. (2014) are expected to be associated with Pre-Tolstojan and Tolstojan terrains, 17.65% with Calorian, 3.25% with Mansurian, and 0% with Kuiperian terrains. For a total amount of 5.1 ± 2 km of radius change accommodated by thrust faults on Mercury (Byrne et al., 2014) then 4.0 ± 1.6 km are expected to be accommodated within Pre-Tolstojan/Tolstojan terrain, and 0.90 km $\pm$ 0.35 km, 0.17 ± 0.07 km, and 0 km are expected to be accommodated within Calorian, Mansurian, and Kuiperian terrains, respectively. Importantly, these numbers of radius change are associated with faults present in the different terrains, but the faults themselves could have accommodated the strain at any time during and after the formation of these terrains. To deduce the actual amount of radius change per time-stratigraphic system, we begin with estimating present day contraction and cumulatively calculate our way backward through time.

From the observed timing relationships, there are no faults cutting Kuiperian craters and so 0 km of Mercury's radius change is expressed in Kuiperian-aged terrains on the scale of observation of this study. In Mansurian terrain, $\sim 0.17 \pm 0.07$ km of radius change is expected to be expressed by thrust faults, all of which must have been accommodated during that system. Accounting for the area ratios of all present craters during the Mansurian, geometric probabilities allow for up to $\sim 0.54 \pm 0.21$ km of radius change accommodated by faults in Calorian terrain and $\sim 2.47 \pm 0.97$ km radius change accommodated by faults in Pre-Tolstojan/Tolstojan terrain to also have occurred during the Mansurian (see supporting information), summing to a total of 3.18 ± 1.20 km of contraction ($-0.13\% \pm 0.05\%$ strain) likely being accommodated during that system.

Since 0.54 ± 0.21 km of the 0.9 ± 0.35 km of radius change expressed by faults in Calorian terrain are likely to already have occurred during the Mansurian and faults cutting Calorian craters do not express strain that occurred during the Pre-Tolstojan and Tolstojan systems, the remaining 0.36 ± 0.14 km of contraction associated with those faults must have been accommodated during the Calorian. Again, accounting for the area ratios of all studied craters that were present in the Calorian, geometric probabilities allow for up to 1.67± 0.65 km radius change accommodated by faults in Pre-Tolstojan/Tolstojan terrain to have occurred during the Calorian, summing to a total of 2.03 ± 0.79 km of contraction (−0.08% ± 0.03% strain) likely being accommodated during that system.

The cumulative amount of radius change accommodated during the Calorian and Mansurian systems equates to 5.21 ± 2.0 km, which is approximately equal to the amount of 5.1 ± 2 km that formed the basis of the calculations. This indicates that faults in Pre-Tolstojan/Tolstojan terrain accumulated displacements well after those periods, and that no strain was accommodated by the mapped thrust faults during those early time systems. The discrepancy of our cumulative amount of radius change and the 5.1 km observed by Byrne et al. (2014) is likely a function of the onset of thrust faulting not coinciding with the Tolstojan/Calorian boundary and this may indicate that thrust faulting was initiated somewhat after the beginning of the Calorian. This finding is consistent with our observations for the onset of global-contraction-induced thrust faulting taking place during the Calorian, with minimal, local thrust faulting activity occurring prior to this system. The calculated radius change of 2 km for the Calorian over a relatively short period of time and of 3 km for the Mansurian over a respectively long period of time supports the inference from the stratigraphic record (see section 2) that thrust faulting was a very active during the Calorian compared to the thrust fault activity during Mansurian.

To quantify the change in strain for each time-stratigraphic system, i.e., the strain rate, we totaled the radius change accumulated during each system and related that amount to Mercury's initial radius and the length of time of each system (Figure 2). Recent estimates in lengths of Mercury's time systems using updated cratering chronologies for the inner Solar System indicate a greater uncertainty of absolute ages, including much shorter Mansurian and Kuiperian systems (Braden and Robinson, 2013; Banks et al., 2016). We represent these ranges of lengths in time using uncertainty regions surrounding our average strain rates (Figure 2, upper panel). During the Pre-Tolstojan and Tolstojan systems, strain accommodated prior to thrust faulting (0.3 to 2.1 km) could have accumulated over the entirety of these systems or in as little as 100 Ma (Klimczak, 2015). The strain rates for this early time range from $5.4 \cdot 10^{-20}$ s^{-1} to $2.2 \cdot 10^{-19}$ s^{-1} (red dots, Figure 2). Our calculations show that Mercury's lithosphere experienced average strain rates of $4.1 \cdot 10^{-20} \pm 1.6 \cdot 10^{-20}$ s^{-1} during the Calorian (green dots, Figure 2) resulting in thrust fault formation, after which the strain rate slowed to $1.8 \cdot 10^{-20} \pm 0.7 \cdot 10^{-20}$ s^{-1} during the Mansurian (orange dots, Figure 2). This decrease in strain rate indicates that global contraction slowed considerably during the Mansurian. Higher initial strain rates would have translated to a fast radius decrease during and before the Calorian, and a much slower radius decrease in the Mansurian (Figure 2, colored, gray, and gray dashed curves). Since no strain was resolved on the scale of our analysis for the Kuiperian, the radius decrease for this system is shown to drop to 0 km to indicate that global contraction, if still ongoing, has not substantially contributed to the strain and tectonic uplift accommodated by the large-scale thrust fault-related landforms on Mercury in its recent geologic history. Byrne et al. (2014), De Achille et al. (2012), and Watters et al. (2013) estimate different amounts of radius change for Mercury. These three estimates produce different strain rates per time-stratigraphic system, but they all show the general pattern of a strain rate decrease over time (Figure 2).

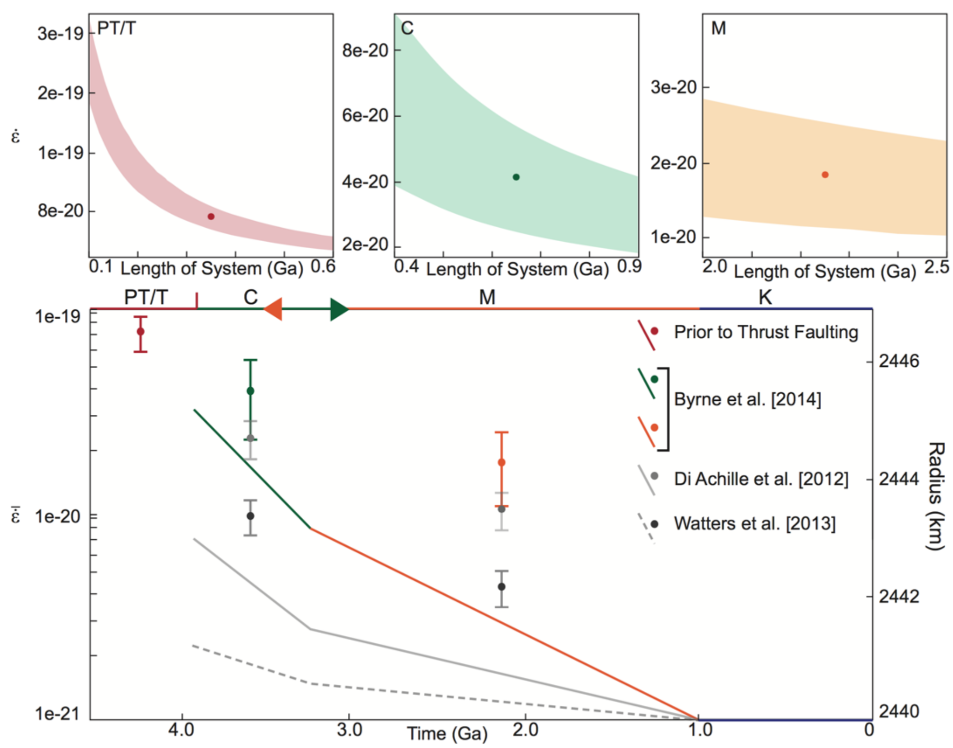

Figure 2.2 Timing and rate of Mercury's global contraction as a function of time before present, with time systems indicated as Pre-Tolstojan/Tolstojan = PT/T, Calorian = C, Mansurian = M, and Kuiperian = K. Red, green, and orange uncertainty regions in the upper plots bound strain rate estimates based on total radius change (7.1 km ≈ upper edge, 3.1 km ≈ lower edge (Byrne et al., 2014)) and the length of time system (shortest ≈

left edge, longest ≈ right edge) (Spudis and Guest, 1988). Average values for strain rates with respect to length of system and radius change are shown as darker points and correspond to colored points in the lower plot. Lower plot shows strain rate averages for Byrne et al. (2014), and those calculated for estimates from Di Achille et al. (2012), and Watters et al. (2013) as dots in color, light gray, and dark gray, respectively. Curves show Mercury's radius expected from the start of the Calorian to present calculated from each of the three sets of estimates.

Implications

Implications for slip rates and duration of development of thrust fault-related landforms

We can utilize our calculated strain rates to gain insight into the time it took to build observed fault-related topography. For example, Adventure Rupes, a thrust fault-related landform ~ 270 km-in-length and showing a topographic expression of ~ 1.3 km has been dated to have formed during the Calorian using crater counting techniques (Banks et al., 2015b). For that, the fault would have taken as little as 5 ± 1 Ma to build to its present structural relief. Similarly, Enterprise Rupes, a large fault-related landform with a length of ~800 km and a vertical relief of ~ 3 km, was previously dated using buffered crater counting to date back to ~3.5 − 3.7 Ga (Giacomini et al., 2015), or to the early Calorian, possibly pre-dating the emplacement of the Rembrandt Basin (Ferrari et al., 2014). For this time frame, it would have taken about 45 ± 10 Ma to establish the present-day topography, if the fault system producing the landform was continuously active within the Calorian. Ferrari et al. (2014) estimated that if the fault system had been active prior to Rembrandt's emplacement, it might have been tectonically active for up to 200 million years, which is broadly consistent with our estimate. Given that some faults have been found to cut young craters smaller than 20 km (Banks et al., 2015a; Watters et al., 2016), it is possible that fault growth has not been continuous, but instead included long periods of quiescence of tectonic activity and subsequent reactivation on Mercury's thrust faults.

Thrust fault growth on Mars has been compared to intraplate thrust faults on Earth with slip rates ~ 0.01 – 1 mm/yr and strain rates between 10^{-17} and 10^{-19} s^{-1} (Schultz, 2003). Faults on Mercury likely grew at comparable rates during the Calorian, where we estimate slip rates for Adventure and Enterprise Rupes to fall between 0.1 mm/yr and 0.4 mm/yr with strain rates at around 10^{-20} s^{-1}. During this system, Mercury quakes may have been on the order of 100 quakes with surface wave magnitudes between 3 and 7 per ten year period, similar to the frequency of Mars quakes estimated from strain rates of ~ 10^{-19} s^{-1} due to global and lithospheric cooling (Phillips, 1991). For slower strains rates in the Mansurian and Kuiperian, and consequently lower slip rates of thrust faults, Mercury quakes triggered by global contraction are likely rare events.

Implications for Mercury's thermal evolution

The magnitude and onset time of global contraction as well as its rate as a function of time can provide important geologic bounds for thermal models and thus for the evolution of Mercury's interior. Most models for Mercury's thermal history recognize two stages of radius evolution: radial growth due to planetary heating, and contraction due to cooling (e.g. Hauck et al., 2004; Grott et al., 2011; Tosi et al., 2013); however, some only allow for contraction with more subdued contraction during initial phases (e.g. Grott et al., 2011). These models often convey results through radius change curves. These curves have positive slopes caused by interior heating and global expansion before peaking and then display negative slopes due to interior cooling and global contraction. Our radius change curves, shown in Figure 2, account for rates of contraction-induced thrust faulting during the cooling period of Mercury's thermal history, and thus have overall negative slopes. Many thermal evolution models display relatively constant radius change following prolonged expansion or periods of little radius change.

While the early phase of expansion is not characterized in this study, the most recent time at which this phase ended must fall prior to the onset time of global contraction-induced thrust faulting. This time and the time derivative of global contraction, represented by the shape of the negative slope — a function of the strain rate — are both constrained with geologic observations of this study. Multiple lines of evidence point to an onset time of global contraction-induced thrust faulting during the Calorian, which, for established crater chronologies, may be as early as 3.9 Ga ago (Spudis and Guest, 1988). This shows that global contraction may have operated much earlier than many of the thermal models predict. After the onset of global contraction, thrust faulting operated at its fastest rate. The process slowed during the Mansurian and slowed even further during the Kuiperian (Figure 2, colored and solid and dashed gray lines). Our results allow future thermal evolution models to be constrained by and assessed with these geologic findings.

Conclusions

Stratigraphic relationships of faults and craters of different degradation stages were used to interpret Mercury's history of global contraction. Heavily degraded, older craters covering a higher portion of surface area on Mercury tend to be cross-cut by thrust faults, whereas fresh, younger craters cover a smaller area but tend to superpose thrust fault-related landforms. Quantification of these relationships allowed us to derive the geometric probabilities for thrust faults to cut craters through time and to relate this finding to the onset time and strain rates of thrust faulting that resulted from global contraction. Our results indicate that global contraction likely began prior to the Calorian, but that thrust faults did not begin to accommodate shortening until the early Calorian. Calculated strain rates show that global contraction slowed toward present day. These results provide geologically constrained estimates of Mercury's timing and rate of contraction, which may serve to check the plausibility of thermal evolution models of the planet. They also advise our interpretations of landform development and slip rates, with the largest faults having the potential to have grown in as little as 50 Ma.

Acknowledgments and Data

We thank Mallory Kinczyk, Caleb Fassett, and Louise Prockter for providing helpful input with the crater classification. This manuscript benefitted from detailed and thoughtful comments from two anonymous reviewers. The methods and data used to produce the results of this paper are derived from freely available sources in the published literature and planetary data system. Datasets and computer code to generate our results are provided in the supporting information. Global thrust fault data set is available from Byrne et al. (2014).

CHAPTER 3

TECTONIC PATTERNS OF SHORTENING LANDFORMS IN MERCURY'S NORTHERN SMOOTH PLAINS[2]

[2]Crane, K.T. and C. Klimczak. 2019. *Icarus*. 317:66-80.
Reprinted here with permission of the publisher.

Abstract

Mercury's northern smooth plains are volcanically emplaced units characterized by ghost craters, volcanically buried impact basins, and thrust fault-related landforms. We analyzed the thrust fault-related landforms, traditionally categorized as lobate scarps and wrinkle ridges, within the northern plains in order to describe trends in how these landforms are organized and oriented and what style of deformation (either thin or thick-skinned) their map patterns represent. Our analysis also establishes geologic constraints for which global processes may have produced stresses contributing to these tectonic patterns. We mapped 4,853 thrust fault-related landforms in the northern plains at a map scale of 1:1,000,000 using three MErcury Surface, Space, ENvironment, GEochemistry, and Ranging (MESSENGER) global monochrome mosaics. These landforms, described as curvi-linear asymmetric ridges, frequently occur in complex geometrical arrangements that are interpreted to share similar structural characteristics. We called these arrangements "compound landforms". Like prior studies, we observed thrust faults to follow rims of buried craters. We also observed (1) sigmoidal rises bounded by fault-related landforms, (2) v-shaped rises composed of two landforms terminating at a single sharp point, (3) broad arcuate rises of nearly equal width, (4) parallel, evenly-spaced ridges, and (5) landforms showing alternation in direction of tectonic transport along strike. Respectively, we interpreted these landforms as transpressional uplifts, faults with sharply juxtaposing ramps, pop-up structures, fold and thrust belts, and antithetic fault intersections. By comparison with Earth analogues and patterns produced in numerical and physical models, our results suggest that deformation in the NSPs is thin-skinned. Orientation analysis showed that the northernmost landforms (90°-70° N) were

predominantly oriented east−west while most of the landforms between 50°-30° N were oriented north−south. Variations in orientation with latitude indicate that the growth of thrust fault-related landforms was influenced by sources of stress other than global contraction. If reorientation of the pole due to the formation of the Caloris basin did occur, the pattern of fault orientations indicates that geologic processes producing the pattern operated after reorientation.

Northern Smooth Plains Background

Mercury's Northern Smooth Plains (herein referred to as the northern plains) is an expanse of smooth terrain deposited by multiple volcanic events (Head et al., 2011) with very few superposing impact craters (Ostrach et al., 2015) and small, isolated regions of rough topography (Susorney et al., 2017). These plains embay heavily cratered terrain producing gradational to sharp physiographic boundaries (Denevi et al., 2013). The northern plains are abundant with ghost craters, volcanically flooded craters recognized by rings of high topography likely localized above buried crater rims and lower topography interior to the rings, and volcanically flooded impact basins with rims jutting above the volcanic units (e.g. Freed et al., 2012; Klimczak et al., 2012; Watters et al., 2012). This suggests that heavily cratered terrain once extended up to the north pole, and then was buried by widespread effusive volcanism between ~3.7 – 3.9 Ga (Denevi et al., 2013; Ostrach et al., 2015). As evidenced by the sharp contrast in the frequency of superposing craters between the northern plains and heavily cratered terrain, the northern plains are inferred to be younger than their underlying units. Regionally, the northern plains units are estimated to be ~1 – 2 km thick (Ostrach et al., 2015). The topography of the northern plains averages 2 km deeper and is characterized by lower slopes than surrounding terrains. This region also contains the northern rise, a ~950 km diameter, ~1.5 km high dome (Zuber et al., 2012).

In addition to fresh and buried impact craters, thrust fault-related landforms are also prevalent in the northern plains (Byrne et al., 2014). These thrust fault-related landforms have traditionally been categorized into three groups based on morphology (Strom et al., 1975; Dzurisin, 1978; Watters et al., 1988; Watters et al., 2004; Watters et al., 2009 and many others): wrinkle ridges, lobate scarps, and high relief ridges. Wrinkle ridges have often been observed as anastomosing, arcuate, asymmetric ridges. They are interpreted to be anticlines above blind thrust faults, but for many of these landforms, a surface breaking fault is visible (Watters, 1988; Golombek et al., 1991; Schultz, 2000; Walsh et al., 2013; Watters et al., 2015a). They are more commonly observed in younger volcanic plains than heavily cratered terrains, older and more degraded volcanic plains, on Mercury and other bodies (Strom et al., 1975; Watters, 1988; Golombek et al., 2001; Byrne et al., 2014) and are distinguished from the other common thrust fault-related landforms on Mercury, lobate scarps and high relief ridges, by their complicated, sinuous morphology. In contrast, lobate scarps are linear to arcuate asymmetric ridges with a fault trace intersecting the surface immediately in front of the steeper slope. High relief ridges are symmetric in cross section and rare compared to the previously discussed landforms. They are interpreted to be anticlines overlying high-angle reverse faults. Although their individual morphologies (e.g. Walsh et al., 2013) have been described, wrinkle ridges, lobate scarps, and high relief ridges are not discrete, clearly distinguishable landform types. End member landforms do exist as exemplars within each category, but we observe the vast majority of thrust fault-related landforms within the northern plains to exist on a spectrum between the three groups. For this reason, we do not categorize our mapped thrust fault-related landforms in the traditional sense. Rather, we map fault surface breaks and anticline crests and identify isolated landforms and larger, more complex landforms, which we call compound landforms. Compound landforms consist of geometrically related anticlines and traces that, by comparison with analogues, are interpreted to share a structural relationship.

Within the traditional taxonomy of landform classification, most if not all of the isolated landforms we map would fall on a spectrum from wrinkle ridge to lobate scarp, and furthermore, their location within that spectrum would change along their length. However, in using a single term to describe the landform, most of these landforms would have been classified as wrinkle ridges, and the detail of their structure would have been lost. To incorporate the classifications of wrinkle ridges and lobate scarps into our descriptions of compound landforms would have been exponentially more exhaustive as more landforms would have to be categorized along this gradient. The use of this language also would not enable the discussion of structural linkage within a compound landform. Classification of landforms as wrinkle ridges or lobate scarps does not facilitate the mapping process or our understanding of how the underlying structures form and link, and thus, we do not attend to the traditional terminology, but rather, make use of more general language.

Thrust fault-related landforms in the northern plains on Mercury have not previously been mapped in sufficient detail to describe map patterns and regional trends in landform morphology and orientation. Detailed morphological descriptions, identification of map patterns, and structural interpretations of these landforms can constrain their subsurface fault architecture, thickness and geometry of the plains deposits, and details of the global or regional processes associated with their formation.

In particular, observational and statistical analyses of morphologies and map patterns and comparison of landform characteristics with planetary analogues could suggest whether faults below northern plains structures are confined within the volcanic plains units or whether they root deeper into the subsurface. Based on results from elastic dislocation modeling and comparison with Earth analogues, Watters (2004) proposed that thrust faults in the Martian plains shallowly root into upper volcanic units Other studies have also suggested that ridges on Mars are underlain by faults that penetrate primarily upper units and regolith, evidenced by modeling, landform geometry, and again, the resemblance of these structures to terrestrial landforms (e.g. Plescia and Golombek, 1986; Watters et al., 1988; Mangold et al., 1998). Comparisons indicate that structural styles in these terrains are similar to thin-skinned tectonics on Earth. For example, the Yakima fold and thrust belt in the Columbia Plateau of eastern Washington has been suggested as an analogue to wrinkle ridges due to their basaltic composition, systems of parallel ridges, and low-lying, only slightly deformed regions between those ridges (Plescia and Golombek, 1986; Watters et al., 2004). The faults underlying this thrust belt shallow into a décollement less than 10 km below the surface (Casale and Pratt, 2015). In contrast, Peterson et al. (2017) contend that northern plains thrust faults extend deeper into regolith and cratered units underlying the plains because elastic dislocation modeling results best reproduce observed topography when model faults are deep-seated. Similar conclusions have been drawn by Schultz (2000), Golombek et al. (2001), and Montési and Zuber (2003b) for thrust fault-related landforms on Mars based on kinematic model results best resolved by faults that do not shallow into décollements and spatial and topographical relationships between parallel landforms which could result from deeply rooted faults. A similar deformation style to that suggested has been observed on Earth in the Rocky Mountains of Wyoming, and is called thick-skinned tectonism, in which thrust faults extend down to a crystalline basement (e.g. Pfiffner, 2017). Landforms like the Wind River thrust fault share similar topography and length relationships to thrust fault-related landforms on Mercury (Watters and Robinson, 1999), and thus can be suggested as analogues to northern plains thrust fault-related landforms. Contrasting analogues and a lack of detailed mapping have limited consensus for the depth of faulting underlying the northern plains structures.

Tectonic Processes and Associated Stress States on Mercury

The tectonics of Mercury have been influenced by many global and regional processes, including impact cratering, tidal despinning, and cooling, subsidence, and changes in orbital parameters that lead to differential surface temperature conditions and changes in solar tides. Each of these processes induces a unique set of stresses within the lithosphere. Impact shock waves propagate from the location of impact and excavate rock, producing the negative topography associated with impact craters (Melosh, 1989). For the remainder of these processes, the orientations and magnitudes of the greatest and weakest stresses control whether lithospheric strain is accommodated by shortening or extension. To initiate faults, these stresses must not only exist, but they must also be of sufficient difference to one another to overcome the strength properties of the host rock. The orientation of the intermediate stress determines the 3D geometry of those faults (Anderson, 1951; Jaeger et al., 2007). Once a fault has formed, it may continue to grow or new similarly oriented faults may propagate until the directions of stresses change or until stresses are no longer sufficiently large to promote failure.

Impact cratering and global cooling are the geologic processes that likely operate over the longest time-scales on Mercury. During the first ~0.5 Ga of solar system history, impacts were more frequent and destructive due to a more substantial population of impactors and a higher concentration of larger-bodied impactors within that population (Marchi et al., 2013). These impacts drove the formation of impact craters and basins, which have degraded over time (e.g. Fassett, 2012; Kinczyk et al., 2016). Global cooling would have prompted global contraction, that is found to have lead to widespread thrust faulting with increased activity early in Mercury's history that slowed down substantially by ~ 3 Ga (Banks et al., 2015; Crane and Klimczak, 2017). Stresses from global contraction are estimated to be horizontally isotropic, and therefore, if large enough, these stresses should have formed a planet-wide distribution of randomly oriented thrust fault-related landforms (Solomon, 1976; Solomon, 1978; Watters et al., 2001; Watters et al., 2004). Dzurisin (1978) and many others after have observed that the tectonic patterns on Mercury are not random, and so other sources of stress must have contributed to the observed landform types and orientations.

Tidal despinning, subsidence, reorientation, and changes in orbital parameters lead to different stress states in the lithosphere than those caused by cooling and crystallization in the interior of Mercury and therefore these processes may have exerted some influence on the pattern of landforms in our study area. A tidal despinning pattern, in particular, has been proposed for Mercury (Melosh and Dzurisin, 1978; Dombard and Hauck, 2008; Matsuyama and Nimmo, 2009; Beuthe, 2010). When operating alone tidal despinning is predicted to cause tensile stresses at the poles that when interpreted with Anderson's Theory of Faulting (Anderson, 1951) are predicted to cause circumpolar graben (Melosh, 1977; Pechmann and Melosh, 1979; Beuthe, 2010) or when assessed with failure criteria are found to produce a random set of joints (Klimczak et al., 2015).

However, a commonality amongst all stress models for the geologic evolution of Mercury is that thermal stresses are expected to result from global contraction due to cooling and that at least part of this contraction was recorded in the formation of thrust faults (Dzurisin, 1978; Dombard and Hauck, 2008; Matsuyama and Nimmo, 2009; Klimczak et al., 2015; and many others). Thrust faulting resulting from global contraction is estimated to have begun as early as ~3.9 Ga (Crane and Klimczak, 2017) near the time of the Caloris impact (Spudis and Guest, 1988). If reorientation due to the Caloris basin formation happened, it could have only happened after this impact occurred. Some studies conclude that tidal despinning must have predated northern plains emplacement and pole reorientation (e.g. Pechmann and Melosh, 1979) while others suggest that reorientation preceded tidal despinning (e.g. Matsuyama and Nimmo, 2009). Large horizontal compressional stresses from global contraction are estimated to have counteracted stresses that would have otherwise caused opening-mode fractures and normal faulting due to despinning and reorientation (Dombard and Hauck, 2008; Beuthe, 2010; Klimczak et al., 2015). Such opening mode fractures would facilitate the transport of volcanic materials to the surface to form the plains, and these materials must have been present to induce subsidence. With a well-established age for the northern plains, the map patterns of shortening landforms within its borders could establish the relative timing of tidal despinning, pole reorientation, and global contraction.

Goals of the Work

Thrust fault-related landform morphologies and map patterns within the northern plains have yet to be described in detail using MErcury Surface, Space, ENvironment, GEochemistry, and Ranging (MESSENGER) datasets. Analyses and descriptions of the morphology of the landforms can indicate the style of deformation within the northern plains: either thick- or thin-skinned, with faults extending below the northern plains or shallowing at the base of these volcanic units. It is also possible to describe geologic controls on the strike (orientation), sinuosity, breadth, and depth of faulting by characterizing these morphologies and when possible, relating them to Earth analogues. The aim of this work is two-fold:

(1) Describe the common shortening-related landform morphologies and their map patterns within the northern plains and discuss their implications for deformation styles and subsurface fault geometry.

(2) Assess combinations of geologic processes which either contemporaneously, temporally overlapping, or in succession could have produced stresses that, if great enough in magnitude, could have contributed to the observed tectonic patterns.

Mapping and Interpretation Methodology

We mapped landforms, including faults with clear surface breaks and broad ridges with no clear surface breaks interpreted to be anticlines, at the 1: 1,000,000 scale. All thrust fault-related landforms with any component of their length extending into the northern plains were included in our mapping process. Faults were mapped where a clear transition between a steep scarp and what can be interpreted to be the fault footwall is observed. These transitions are often linear and sharp, possibly indicating a fault surface break. When the contact is less morphologically crisp, but the sense of asymmetry along the ridge was apparent, we inferred a fault to be present (Figure 1). The direction of more gradually increasing elevation across the ridge was interpreted to be the direction of tectonic transport, or fault vergence. When landforms occurred in linear arrangements, such as faults en echelon or multiple surface breaking faults below a single anticline, a network number was assigned to each fault or anticline within the arrangement to indicate that they belong to a group. Each fault was then assigned an identification number. When crests of anticlines were adjacent to a fault trace such that they clearly belonged to the same structure, they were mapped and labeled with the same identification number as the associated fault. When multiple anticlines were associated with a single fault trace, all associated anticlines were assigned the same identification number as the corresponding fault. When multiple fault surface breaks were visible below a single anticline, the anticline was assigned the same identification number as the longest adjacent fault trace. Anticlines not associated with surface-breaking faults were assigned a unique identifying number.

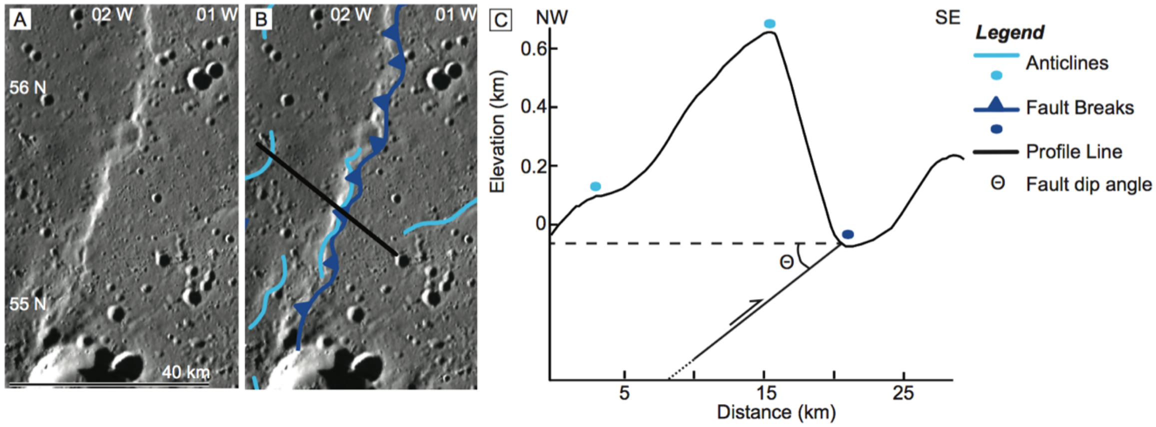

Figure 3.1 This figure shows examples of the types of thrust fault-related landforms mapped in this study. (A) The bright, sharp contrast between the westward-dipping scarp and the flat, eastern terrain indicates that a fault surface break is likely present. The rounded, high topography above the break, along with three additional topographic rises without apparent scarps, were recognized as anticlines. Using traditional taxonomy, this landform would be classified as a lobate scarp. (B) The fault break and associated anticlines (light blue) were mapped at 1:1,000,000 scale (as shown here). The teeth on the dark blue fault trace line indicate the direction opposite of vergence. Both (A) and (B) are images from the MDIS monochrome global mosaic, shown in orthographic projection centered at 0° E, 5° N. The black line crossing (B) corresponds to the profile line shown in (C). (C) The shallowly dipping back slope and steeply dipping scarp associated with the landform shown here is displayed as a MLA topography profile. Light and dark blue dots indicate where anticlines and fault were mapped on the image. Thrust fault-related landforms are hypothesized to be underlain by thrust faults, which do not necessarily break the surface, but dip at approximately the same angle as the overlying slope (Watters, 1988; Golombek et al., 1991; Schultz, 2000; Walsh et al., 2013; Watters et al., 2015a).

We took three additional precautions to lessen uncertainty associated with mapping. First, we mapped anticlines and fault surface breaks as polylines in ArcMap using the streaming function, which automatically produced equally spaced nodes along each polyline. The projection and center of projection used can also greatly affect the accuracy of the mapping process. The northern plains were divided into 10 by 10 degree bins, and the center location of each bin was used as the center of a orthographic projection of the mosaics and hillshades. This minimized mismatch between the imaged landforms and the polylines we drew to indicate their locations. All landforms within each bin were mapped before the projection was changed to center upon the next bin. Finally, we utilized multiple mosaics and thus illuminations in the mapping process: the Mercury Dual Imaging System (MDIS) MESSENGER global mosaic basemap data record (version 1), eastern illumination mosaic, and western illumination mosaic (all 166 m/pixel). When observing our mapping locations, we viewed each mosaic separately, determined which mosaic was the most continuous and displayed the sharpest visualizations of landforms, and used that mosaic in mapping. Occasionally, some landforms could be observed in one mosaic, but not in the other two. When this occurred, multiple illumination mosaics where used consecutively to capture all landforms in our map. These mosaics were supported by multiple hillshades created from the Mercury MESSENGER global Digital Elevation Model (DEM, 665 m/pixel, Becker, et al., 2016). Using a DEM facilitated the recognition of landforms during mapping.

Identification, Mapping, and Description of Compound Landforms

Once all landforms were mapped, each bin was visually assessed for trends in map patterns and in morphology associated with those landforms. During the initial mapping process, the entirety of each bin was not visible at the 1:1,000,000 scale, and therefore, the connectivity of landforms across multiple bins or even across longer distances within the same bin was not apparent during the mapping process. However, upon increasing our scale of view, we were able to describe what we term "compound landforms". Whereas an individual landform may not link to any other landforms, the morphology of compound landforms and the geometry of their associated map patterns allow us to interpret the faults and/or anticlines to be structurally related based on comparison with terrestrial and planetary analogues. In each bin, observations of compound landforms and other structural patterns were recorded. Our descriptions included size (where we could confidently take measurements because the landform had not been too degraded or reshaped by impacts), shape, position, relationship to topography, relationship to gravity (where Earth analogues prompted that this property should be investigated), and spatial relationship to other compound landforms and the northern plains boundaries. After all bins had been assessed, we reviewed our observations for patterns, for compound landforms and/or landform characteristics that were observed multiple times across the northern plains.

Identifying Earth and other planetary analogues for compound landforms and the structural characteristic was an iterative process. Detailed descriptions for each of the compound landforms were composed first, and then extensive literature searches for key terms within the descriptions were conducted. Once potential analogues were identified, we scanned the examples within the literature for descriptions of morphology and setting. These descriptions and accompanying images were compared to our observations of landforms on Mercury. We also searched for the analogues described in the literature using Google Earth Pro, and compared satellite images from Earth to our Mercury mosaics. When key characteristics from potential Earth analogues differed from our observations, we searched the literature for sandbox and computer models that generated landforms with similar morphology and/or tectonic pattern. For some compound landforms, model parameters that caused morphological variations from the previously investigated Earth analogues were able to accommodate the observed differences between our compound landforms and the analogues. After locating analogues that reflected our observations of Mercury, we searched within the literature for proposed structural interpretations and subsurface geometry of those landforms. We purposefully conducted this portion of the literature review second so that the process of identifying analogues was not biased by our preconceptions of what the depth and style of faulting in the northern plains might be.

Map and Landform Description

In total, we mapped 2053 scarps with surface breaks and clear directions of vergence and 2800 anticlines within the northern plains (Figure 2, included as a supplementary shapefile). The longest mapped fault surface break was ~255 km and the shortest was ~3 km. The longest mapped anticline was 211 km and the shortest mapped anticline was ~3 km. We identified 218 linear to curvilinear groups of landforms, such as en echelon fault-related landforms or multiple anticlines along a single fault trace. The cumulative lengths of fault surface breaks and anticlines were 61,265 km and 72,336 km, respectively. Five common compound landforms and one common structural characteristic were identified in our analysis. The compound landforms described here represent end-member cases; however, across the northern plains these landforms are observed in gradients, transitioning between morphologic classifications.

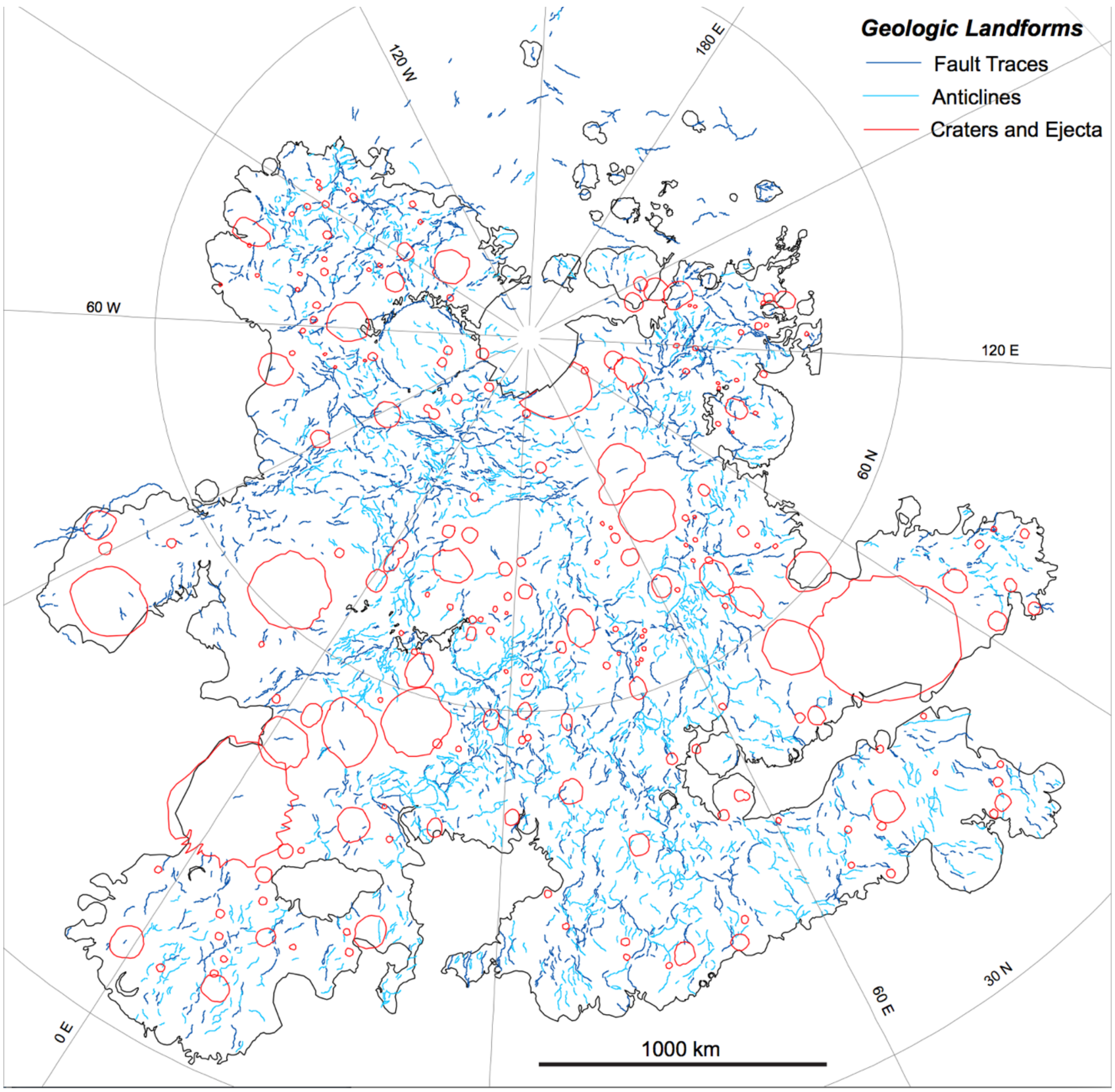

Figure 3.2 This map displays the thrust fault-related landforms we identified in the northern smooth plains and mapped on a scale of 1:1,000,000. The nearly 5,000 structures are shown in blue, and craters and crater ejecta are outlined in red (Denevi et al., 2013). Map is shown in stereographic projection centered at 30° E, 66° N.

Below we describe in detail (1) number and dimensions of identified compound landforms for which we felt accurate measurements could be taken, (2) the morphologies and map patterns of the compound landforms, (3) analogues to the compound landforms observed, and (4) the structural interpretation of those analogues and their implications for landform development on Mercury. The locations of these landforms are included as a supplementary shapefile.

<u>Faults Following Crater Rims</u>

We identified 429 circular rings of thrust fault-related landforms (e.g. Figure 3). For 422 of these landforms, we measured the diameters of the rings using the geodesic length tool in ArcMap. These values range from 5 to 589 km. We observe an abundance of smaller diameter rings and progressively fewer large diameter rings. We calculated the mean diameter to be 38.1 km, the median to be 24.5 km, and the standard deviation to be 46.7 km. The observation of skewed diameter distribution is supported by plotting the cumulative frequency distribution of diameters and calculating its slope, a steep ~-3.3. Although there is a wide variation in diameter, we do not observe or record wide variation in elevations associated with these rings.

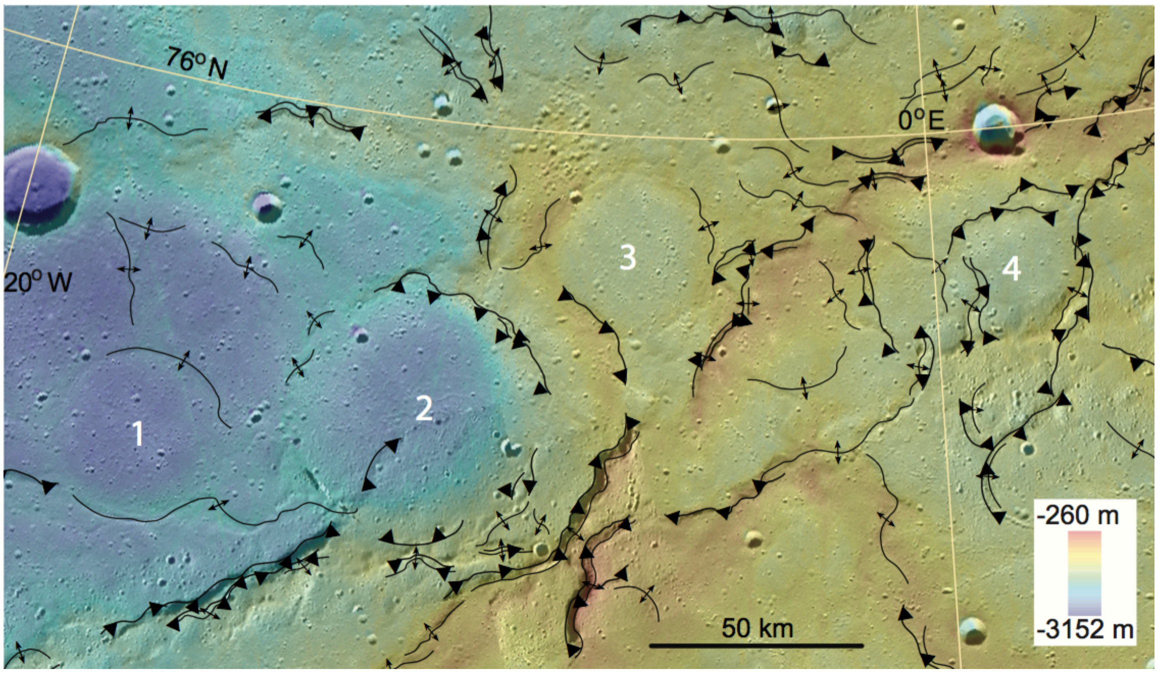

Figure 3.3 Multiple buried impact craters bordered by thrust fault related landforms are highlighted in this MDIS monochrome global mosaic overlain with MLA topography. These examples display the breadth of ways in which shortening landforms outline buried impact craters. Example 1 shows a ghost crater with a rim composed of two anticlines. Anticlines and surface breaking faults bound the rims of examples 2 and 3, and example 4 is nearly completely outlined with thrust fault-related landforms with fault traces verging outward from the crater interior. The mosaic is shown in orthographic projection centered at 74° N, 4° W. *Size 13.2 cm in width x 7.7 cm height, 1.5 column width*

Each ring is composed of varying numbers and lengths of fault traces and anticlines. When rings of landforms with visible fault surface breaks are observed, faults typically verge outward from the center of the ring implying that their slip surfaces dip toward the center of the buried crater. Anticlines are distinguishable from buried crater rims by their symmetry and pronounced topography. Smaller rings (< 15 km) are often composed of a single, curved anticline. Moderately sized rings (15 - 100 km) typically include a combination of fault traces and anticlines. For example, in Figure 3, at least four rings each ~ 50 km in diameter can be seen. One of these example rings (labeled “1”) is entirely composed of anticlines, two are produced by a combination of anticlines and fault traces (labeled “2” and “3”), and a fourth is a nearly complete ring of surface breaking faults (labeled “4”). The largest mapped rings (> 100 km) is outlined by multiple traces and anticlines, sometimes en echelon. Landforms surrounding larger rings do not appear longer or to have more associated topography than those associated with smaller rings. Rings of all diameters are observed in each of the analyzed bins, and are very common throughout the plains except in regions interpreted to be floors of large impact basins.

These rings are interpreted to be wrinkle ridge rings- landforms that follow the rims of buried impact craters. Wrinkle ridge rings have previously been observed on Mercury (Freed et al., 2012; Klimczak et al., 2012; Watters et al., 2012; Wright et al., 2018), Mars (Watters, 1993; Neel and Mueller, 2007), and the Moon (Wood et al., 2005; Byrne et al., 2015). Similar to other rings on other bodies, the wrinkle ridge rings on Mercury are characterized by broad topographic depressions within the more elevated rims (Freed et al., 2012). They have also been observed to host graben interior to the ring (Klimczak et al., 2012; Watters et al., 2012) and more rarely, to be bounded by graben rather than thrust fault-related landforms (Klimczak et al., 2012).

Schultz (2000) as well as Allemand and Thomas (1995) suggest that the rims of impact craters act as stress concentrators. The effectiveness of concentration was estimated in these studies by comparing crater rims to punched holes in metal sheets, which were then stressed. Comparing impact craters to notches rather than holes, it is possible that stresses are three times as great or more at the base of a bowl shaped crater than within the terrain surrounding the crater. Studies of stress concentrations along notches with level basins suggest that craters with more subtly concave floors (e.g. flat-floored craters) concentrate stresses closer to their rims (Young and Budynas, 2002). If faults are produced by stress concentrations along craters, faults should root near the center of crater floors or crater floor-wall contacts and verge outward, away from the crater center. Models specific to Mercury (those discussed in the previous paragraph) also show that stronger volcanic units that overly weaker crustal layers, thinning of volcanic units over rims, and thinner crustal units such as volcanic units within impact craters concentrate stresses within crater rims to five times the level in plains exterior to those rims.

Faults tend to propagate along favorably oriented pre-existing weaknesses (e.g. Cowie and Scholz, 1992; Vermilye and Scholz, 1998; Jaeger et al., 2007). Faults may use the boundaries between crater fill, floor, and walls as pre-existing weaknesses along which to propagate. We acknowledge that faults bounding larger basins such as Mare Crisium on the Moon have been found to verge inward toward the crater center, but these faults are predicted to utilize the boundary between the crust and uplifted mantle as a pre-existing weakness (Byrne et al., 2015). Buried craters within the northern plains are not as large as the basin hosting Mare Crisium and the faults at these craters are not likely associated with mantle uplift, such as suggested for those in Mare Crisium. We interpret the uniformity of topography despite the variability of associated crater diameter to be a consequence of larger craters lacking substantially larger depth to diameter ratios than smaller craters and level floors. Thus, faults associated with larger craters may not reach depths substantially deeper than faults propagating through smaller craters.

<u>Broad, Linear to Arcuate Rises of Equal Width</u>

Networks of broad, linear to arcuate rises bounded laterally by thrust fault-related landforms verging away from the rise are observed near regions with an increased density of impact related landforms throughout the northern plains. Of the 71 landforms we identified, 44 were measured because they have both clear lateral boundaries, such as where a steep scarp face sharply met more gentle terrain, and locations where the lengths of the rise terminated, lost topography, or transitioned into another landform are visible. The lengths of measured landforms are widely distributed with a mean of 50.7 km and standard deviation of 35.6 km. The widths, however, are more narrowly distributed with a mean of 12.6 km, a median of 10.7 km, and a standard deviation of 7.5 km. For example, two of the longest rises (measuring 100 and 111 km) have widths of 9.5 and 9.3 km. The longest rise (146 km long) has a width of 39.5 km, but this landform is much wider than all others we observe.

Rises link and terminate into each other and into other landforms, producing their networked structural patterns. Smooth, sometimes arcuate transitions link multiple rises. Where rises meet flooded or buried craters, four different transition morphologies are observed: (1) the rise ends abruptly along the rim of the crater; (2) one of the two bounding thrust fault-related landforms links to a through-going landform within the crater; (3) the rise itself follows the crater rim curving through the crater interior and continuing beyond the other side of the crater or (4) one of the two landforms links to a wrinkle ridge ring. In cases (2) and (4), small en echelon anticlines indicate stepover regions between the two landforms. Each case is exemplified in Figure 4, and the landforms are labeled with corresponding numbers.

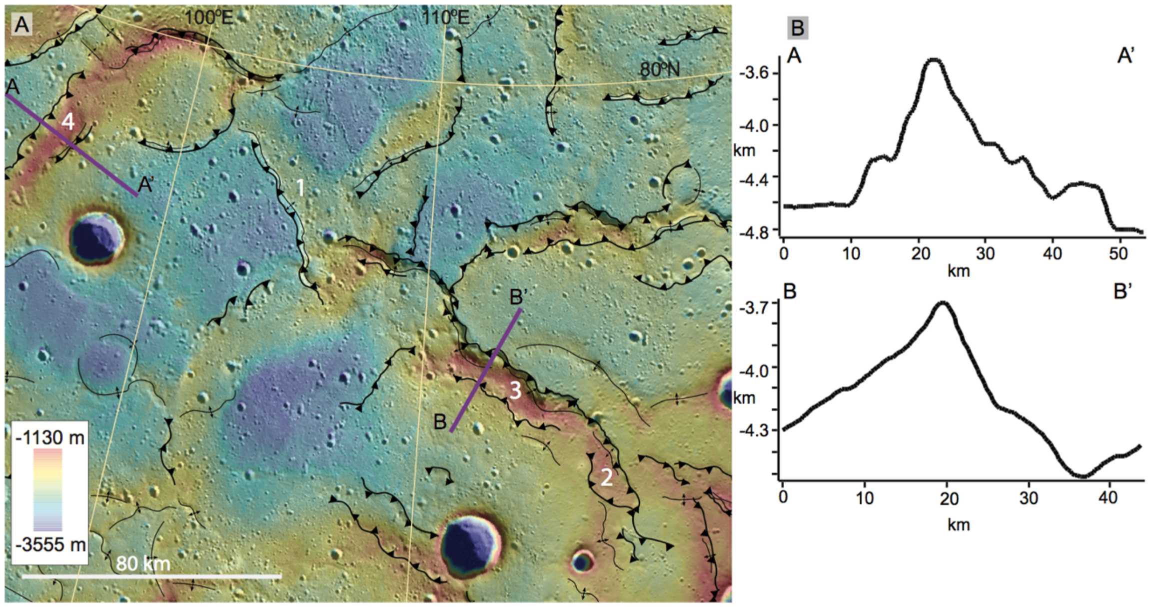

Figure 3.4 This figure shows a mosaic with many examples of broad, equal-width rises in a linked arcuate network with topographic profiles corresponding to two rises in the image. Structural mapping shows that some rises are bounded by two outward verging thrust fault-related landforms, while others are only clearly bounded on one side. (A) A section of one of these networks just south of Yoshikawa crater is shown in an MDIS monochrome global mosaic overlain with MLA topography in orthographic projection centered at 79° N, 114° E. Profile lines are shown in purple. (B) Topographic profiles corresponding to lines A-A' and B-B' show that these landforms are approximately symmetric compared to other thrust fault-related landforms and have distinct peaks.

We interpret the broad rises to be pop up structures. Due to their consistent width throughout the northern plains, it is likely that the structures root into the same layer or have similar depth extents. Assuming fault dips of 60, 45, 30, or 20 degrees, the depth of that layer would be ~9, ~5, ~3, or ~2 km respectively. These depths are of the same order of magnitude as the estimated depths of the volcanic units of the northern plains. Pop up networks, such as the Mari Bugdi Pop Up Zone within the Sulaiman Fold and Thrust belt, have also been shown to root into a single layer and to dip as steeply as 60 degrees (Jadoon et al., 1994). In this zone, passive roof deformation generated pop ups solely within geologic units above one specific décollement. By analogy, the proposed pop up networks in the northern plains could root into the base of the northern plains volcanic units.

V-Shaped Rises

Twenty V-shaped rises are observed in groups within the northern plains. All groups are north of 70° N or south of 40° N. The landforms are composed of two thrust fault-related landforms meeting at a sharp intersection point (e.g. Figure 5). The landforms verge away from the central angle between the two landforms, and the bisector of the angle is typically oriented to the north. The back limbs of the two landforms are often characterized by anticlines in smaller structures (~ 10 km across the widest span of the "V") and both anticlines and plateaus in larger structures (~ 150 km across the widest span of the "V"). The highest topography along the rise occurs at the landform intersection point. In larger structures, a small plateau can be observed at this intersection interior to the central angle. For example in Figure 5, the westernmost V-shaped rise has a small plateau visible within the central angle, while the southernmost rise does not. Away from the vergence direction, the landform elevation gently tapers off.

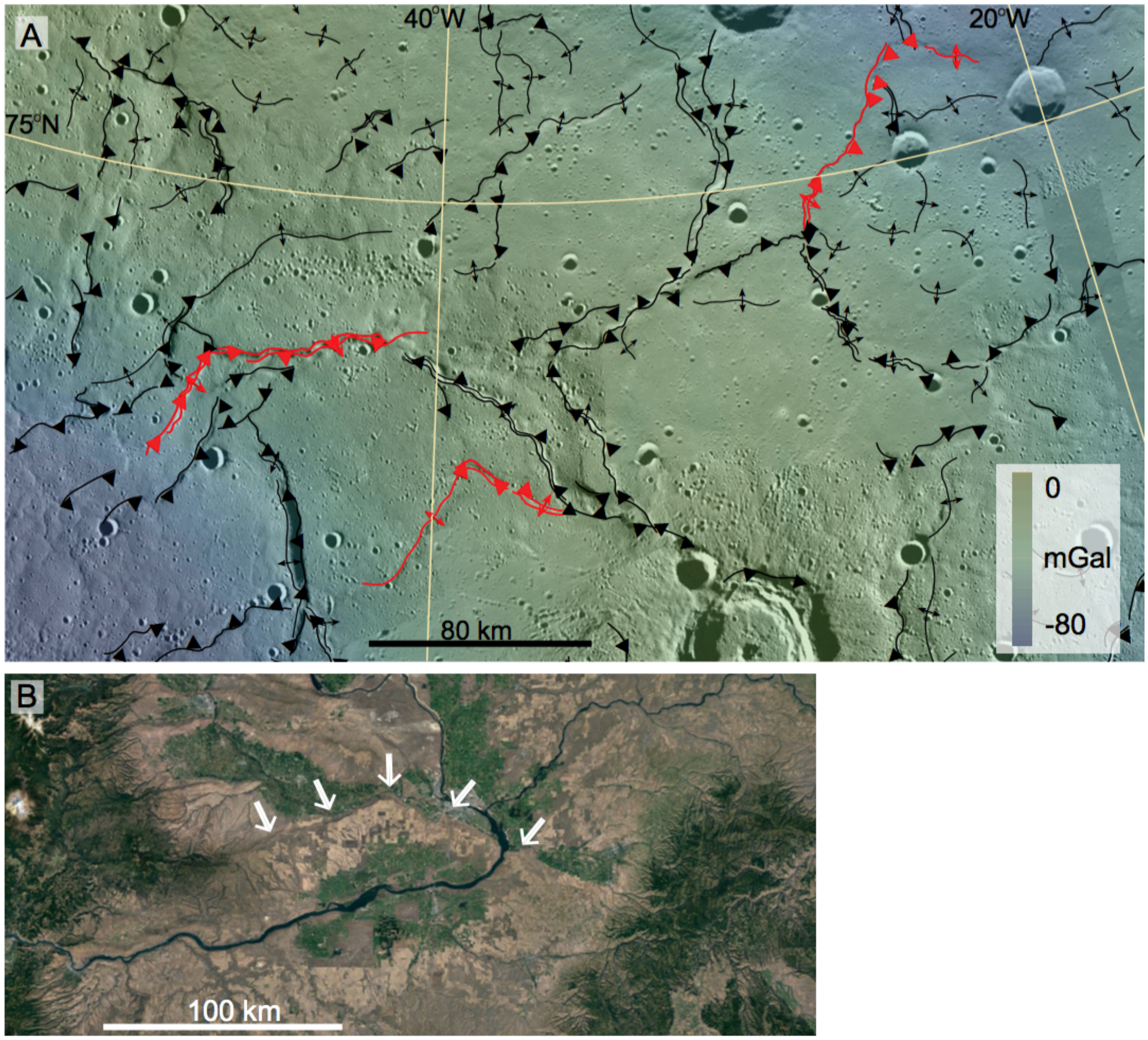

Figure 3.5 V-shaped rises composed of two landforms terminating at a single point. (A) Three examples are highlighted with red symbology on an MDIS global mosaic overlain with gravity anomaly field (Mazarico et al., 2014). Structural interpretations show that one of the two adjoining landforms in each example terminates near a negative gravity anomaly. The mosaic is centered at 73° N, 46° W in orthographic projection. (B) A Google Earth image of the Horse Heaven Hills anticline, a possible Earth analogue, clearly displays a similar v-shaped morphology. The anticline limbs and intersection point of the landforms composing its limbs are indicated with white arrows.

We suggest two possible formation mechanisms for these landforms. One possibility is that two independent faults grew towards each other and their growth along strike ended once they linked. Anticlines developed above the faults as they propagated. Typically though, linkage is characterized by restraining bends and stepovers—landforms that tend to be more arcuate than the crisp intersection points observed (e.g. Mann, 2007). A second possible mechanism is that as a single fault grew it was deflected or redirected along strike. Impact craters, basins, and/or pre-established fault systems could cause this redirection. A similar landform, the Horse Heaven Hills Anticline, is observed within the Yakima Fold and Thrust Belt (YFP, Figure 5), a set of terrestrial thrust fault-related landforms within the Columbia River flood basalts. This anticline was likely redirected along the Olympic Wallowa Lineament (OWL) and pre-existing Wallowa Fault (Casale and Pratt, 2015). A separate study suggested that the termination and redirection of the YFP landforms was caused by both the presence of the OWL and the gravity low associated with the Pasco basin (Blakely et al., 2014). We analyzed the locations of V-shaped rises in relation to the gravity anomaly field of Mercury (Mazarico et al., 2014). In some cases, such as those shown in Figure 5a, large V-shaped rises terminate along the edge of gravity lows. By analogy to the YFP landforms, these may form as a consequence of relatively thin-skinned deformation as underlying thrust faults follow a décollement horizon between 5 and 10 km depth (Casale and Pratt, 2015).

<u>Sigmoidal Rises</u>

We observe 19 lense or sigmoidal shaped rises bounded by thrust fault-related landforms verging outward from the center of the rise. We felt confident to take measurements for 10 of these sigmoidal rises. They have an average length-to-width ratio of ~3.3 and ranged in length from ~ 10 km up to ~200 km. Larger rises are characterized by clearly identifiable fault surface breaks along their boundaries and plateau like uplift within these boundaries. For example, in Figure 6 the sigmoidal rise shown has a 21 km plateau bounded between oppositely verging thrust faults. Additional faults and/or anticlines cross cut through the plateau, frequently occurring sub-parallel to one of the bounding landforms. Within the plateaus, it was also common to find linear, narrow landforms connecting to one another at irregular angles with no apparent planimetric geometric relationship to the bounding faults. Arrows in the figure point to two examples of these smaller interior landforms. Smaller rises were smooth within their interior. Both large and small rises were more common south of 80° N.

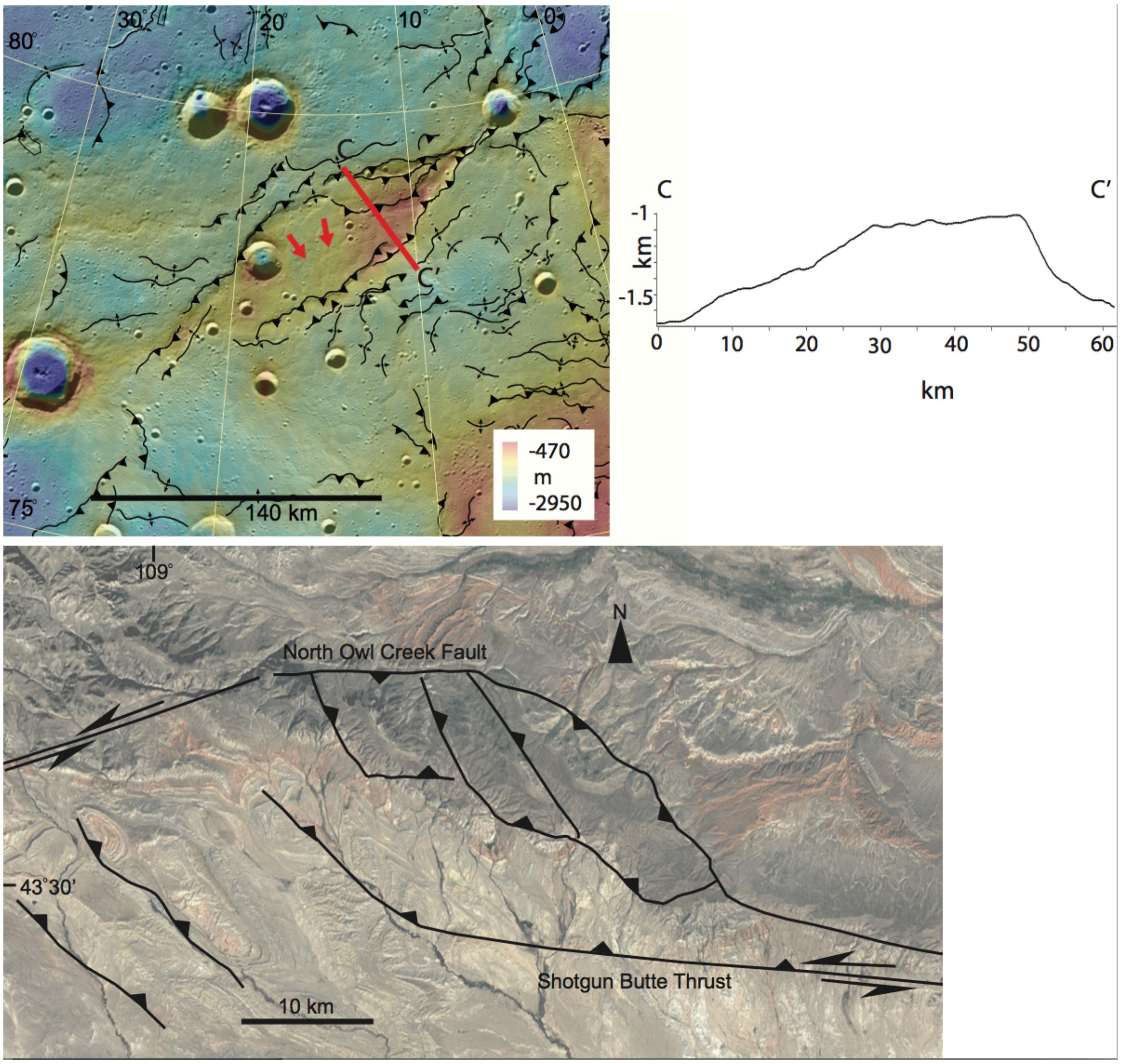

Figure 3.6 This figure shows an example of a large sigmoidal rise in the northern plains, a possible Earth analogue to this rise, and a topographic profile across the example shown for Mercury. (A) This 200 km long rise is displayed in an MDIS global mosaic overlain with MLA topography using a orthographic projection centered at 78° N, 15° W. Structural interpretation indicates that the rise is bounded by thrust fault-related landforms verging away from the center of the rise. (B) Similarly, the Owl Creek Pop Up Structure, shown in a Google Earth image overlain with structural interpretation (Paylor and Yin, 1993), shows a map pattern of thrust faults verging outward from the center of

the rise and interior landforms sub-parallel to one of bounding landforms. (C) Rises are also both characterized by a plateau, shown here in a topographic profile taken across the sigmoidal rise shown in (A). The profile line corresponds to the red line in (A). The plateau has ~1 km of relief and is ~20 km wide.

We interpret large sigmoidal rises to be stepovers, zones of slip transfer between faults, and smaller sigmoidal uplifts to be restraining bends, jogs along the length of a fault which concentrate compressional stresses (Mann, 2007). Both landforms are associated with strike and oblique slip along fault surfaces. Massironi et al. (2015) identified similar landforms in the mid-latitudes on Mercury and thoroughly described common strike slip kinematics on the planet. They do not identify any sigmoidal rise as large as the example shown in Figure 6a. If this structure does imply oblique slip, then that slip predates the emplacement of the craters on both ends and interior to the structure. These craters do not display evidence of strike-slip.

Large stepovers like the one shown develop as two faults grow towards each other. Modeling shows that parallel anticlines and small polygonal shears develop in the interior of the rise when relatively little overlap exists between the fault tips before linkage (McClay and Bonora, 2001; Mitra and Paul, 2005). Both interior anticlines and shears are observed within two large stepover structures identified ~ 75° N. This style of linkage is similar to the Owl Creek Pop Up Structure near Laramie, WY (Figure 6c). Here, the Shotgun Butte Thrust and North Owl Creek Fault transfer shortening between two low-angle thrust systems. Three sub-parallel anticlines cross cut the rise (Paylor and Yin, 1993). Although it is unclear how deep these low angle faults root, they are projected to just over 1 km in cross sections produced by Paylor and Yin (1993), and steeply dipping faults are only locally produced and necessary to produce the pop up between the two low angle thrusts.

Evenly-Spaced Parallel Ridges

The final type of thrust fault-related compound landforms that we identify within the northern plains is parallel, evenly spaced topographic highs. We located 26 sets of three or more parallel ridges, and felt confident in measuring the characteristic lengths and widths of 22 of these systems of ridges. Width was recorded as the distance between the two ridges at either end of the systems. Although there is a wide distribution of lengths and widths, the ratios of length-to-width are approximately narrowly distributed and slightly skewed right with a mean of 2.8, median of 2.0, and standard deviation of 0.7. Short, narrow ridge systems are composed of parallel to subparallel anticlines. Longer, broader ridge systems contain parallel to subparallel anticlines and anticlines above fault traces, with all faults verging in the same direction and anticlines with the same sense of asymmetry. These individual landforms increase in elevation in the direction of vergence, regardless of whether their overall trend was linear or arcuate. In most cases, the ridges appear to have extremely smoothed topography, indicating that they may be older than other nearby landforms, but some, such as the Le Dauphine Rupes system have crisp morphologies with clear surface breaking faults, dramatically asymmetric slopes, and few superposing craters (Figure 8). In Figures 7a and 7b, we show a topographic profile and structural map of the Le Dauphine Rupes system where topography increases slightly to the northeast, the direction of vergence.

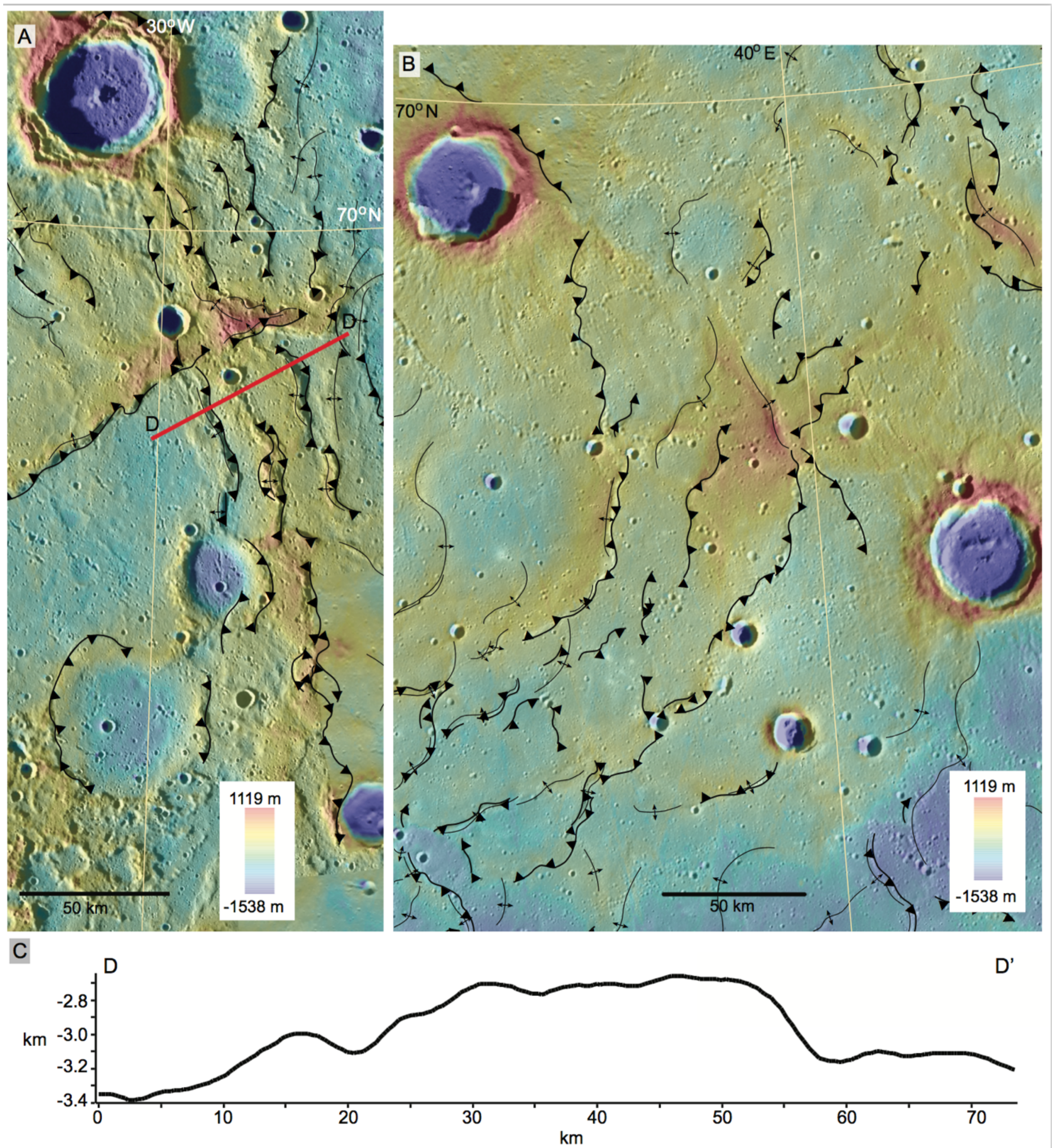

Figure 3.7 This figure shows an image of a system of linear parallel ridges, a contrasting system of ridges with arcuate morphology, and a topographic profile across the system of linear ridges. (A) The Le Dauphine Rupes fault system is shown in a global mosaic overlain with MLA topography in orthographic projection centered at 68° N, 28° W. Our structural mapping indicates that the landforms in this system verge to the northeast. The line across which we created a topographic profile is shown in red. (B) An unnamed fault

system near Rivera crater exhibits a curvilinear plan form. This system is displayed with a global mosaic overlain with MLA topography in orthographic projection centered at 66° N, 35° E. The curved map patterns exemplify arcuate systems of parallel ridges. (C) This topographic profile was taken across the Le Dauphine Rupes fault system shown in (A). Topography associated with system extends for almost 50 km laterally and ~500 m vertically, and the profile rises in elevation to the right (East).

We interpret these systems of parallel ridges to be (1) fold and thrust belts in the case that the system is composed of linear ridges or (2) rings within or bordering ancient impact basins when the system is composed of arcuate ridges. Massironi et al. (2015) also classified the Le Dauphine Rupes system as a fold and thrust belt containing some transpressional landforms. Periodically spaced landforms, traditionally termed wrinkle ridges, have been recognized on Venus (Bilotti and Suppe, 1999), Mars (Watters, 1988), Earth (Watters, 1989) and the Moon (Yue et al., 2015). Models suggest that evenly spaced thrusts resulting in evenly spaced ridges in fold and thrust belts correspond to rapid shortening rates (Couzens-Schultz et al., 2003). These rates produce narrow thrust sheets in which evenly spaced ramp anticlines propagate within a passive roof duplex. Strong décollements also promote foreland propagation of structures (Couzens-Schultz et al., 2003) where often topography increases into the foreland. The remarkably even spacing of these systems on Mercury resembles the faults of the upper Lesser Himalayan Duplex. Long et al. (2010) proposed that the faults within this duplex root into a single shallow quartzite layer. Given that these landforms on Mercury are observed less often than other compound landforms, they may represent fault propagation through regions where thinner regolith underlies the northern plains volcanic units, and thus faults root to a stronger décollement. As most appear to be older landforms, they may also reflect shortening from the earliest history of Mercury when global contraction was operating at its highest resolvable rate (Crane and Klimczak, 2017).

Changes in Vergence

Abrupt changes in vergence along length, a previously recognized characteristic of planetary and Earth thrust fault-related landforms (e.g. Plescia and Golombek, 1986; Byrne et al., 2014), are so commonly observed in this study that we do not record their locations. Often, multiple vergence changes are observed along a single landform (e.g. Figure 7). These alternations in anticline asymmetry are observed along linear fault scarps and along bends where landform orientation changes dramatically. The region of vergence change shows three morphologies: (1) a smooth topographic high connecting two crests of anticlines associated with thrust fault-related landforms with opposite senses of asymmetry, (2) tips of adjacent thrust fault-related landforms wrapped concave inward towards each other, developing a small depression between the tips, or (3) greatly reduced topography in the region between the two landforms creating a featureless null space. Examples of each of these morphologies are shown in Figure 7. A smooth transition between a south verging thrust fault-related landform and a northwest verging thrust fault following a crater rim illustrate the first type of transition (Figure 6, example 1). In the central portion of the image, the western tip of a northward verging and the eastern tip of a southward verging thrust fault related landform arc toward each other, creating a < 5 km wide depression (Figure 6, example 2). To the south, an ~8 km long gap with very little topography separates northward verging and southward verging thrust fault-related landforms (Figure 6, example 3).

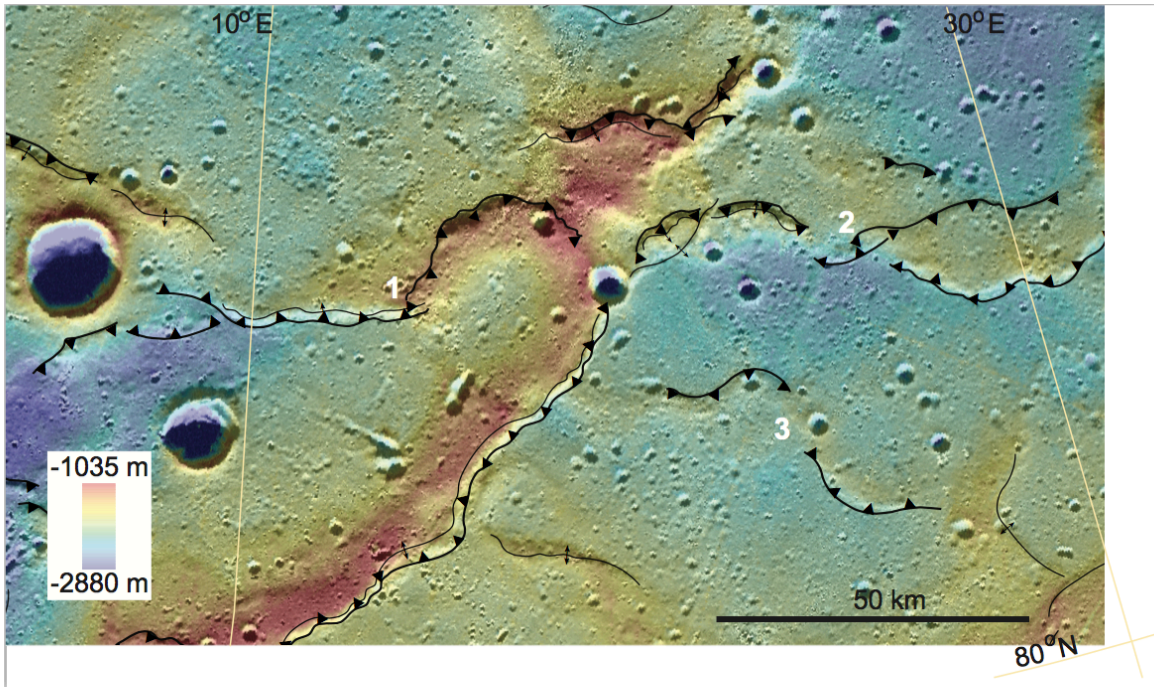

Figure 3.8 This MDIS mosaic shows three examples of the morphologies associated with alternation in vergence direction along strike. The image is overlain with MLA topography using orthographic projection centered at 80° N, 13° E. Example 1 shows a smooth transition between an anticline crest along a thrust fault-related landform and a crater rim bounded by a surface breaking thrust fault. Example 2 shows a small depression between the concave tips of multiple landforms. Example 3 shows a region between two oppositely verging landforms where no negative or positive topography has developed.

Changes in vergence have been observed on thrust fault-related landforms on Mars (Watters, 1993) and within fold and thrust belts on Earth. In the Niger Delta Fold and Thrust Belt, changes in vergence are caused by antithetic fault interactions. Faults change vergence direction rapidly here due to their propagation from a weak basement décollement (Higgins et al., 2007; Davis and Engelder, 1985). In the Big Piney La Barge

Field of the Cordilleran Thrust Belt antithetic faults also root to the same detachment surface resulting in anticlines with opposing senses of asymmetry (Greenhalgh et al., 2015). These studies conclude that the depth at which antithetic fault planes intersect determines the surface expression of the region between the oppositely verging anticlines. Faults that link only in the décollement produce none to small amounts of topography between their tips. If these faults propagate towards one another at shallow lithospheric depths, their tips may bend towards each other, forming small basins between the tips (Higgins et al., 2007). Some faults instead only intersect near the surface resulting in a fold connecting the two hanging wall anticlines and high topography (Higgins et al., 2007).

All three transition region morphologies are observed in the northern plains. In general, thrust fault-related landforms within the northern plains may exhibit an average overall orientation while many smaller segments along the thrust fault-related landform may deviate from that strike. This results in small bends along the length of the thrust fault-related landform. This observation, combined with the observations of vergence changes and the topography associated with those changes leads us to conclude that faults associated with these changes are likely rooted in a weak décollement below the northern plains. In most cases, our mapping suggests that folding precedes faulting. Individual conjugate faults may nucleate along the length of the folds and link up either in the décollement below the volcanic units or closer to the surface. As their surfaces intersect, the faults reshape the pre-existing fold producing clear changes in vergence direction, and sometimes strike, along the length of the thrust fault-related landform.

Discussion

Density of structures

We analyzed the density of thrust fault-related landforms within the northern plains (Figure 9). Each landform with a unique identifying number was divided into ~1.5 km long segments. The coordinates of the centroid of each segment were calculated, and then the number of centroids per square kilometer was computed. Anticlines associated with mapped fault traces were filtered out of the calculation, as to not weight landforms with both anticlines and traces more heavily. This method of density calculation also prevented short faults from being weighted evenly to long faults, as the numbers of segments, not faults themselves, were recorded.

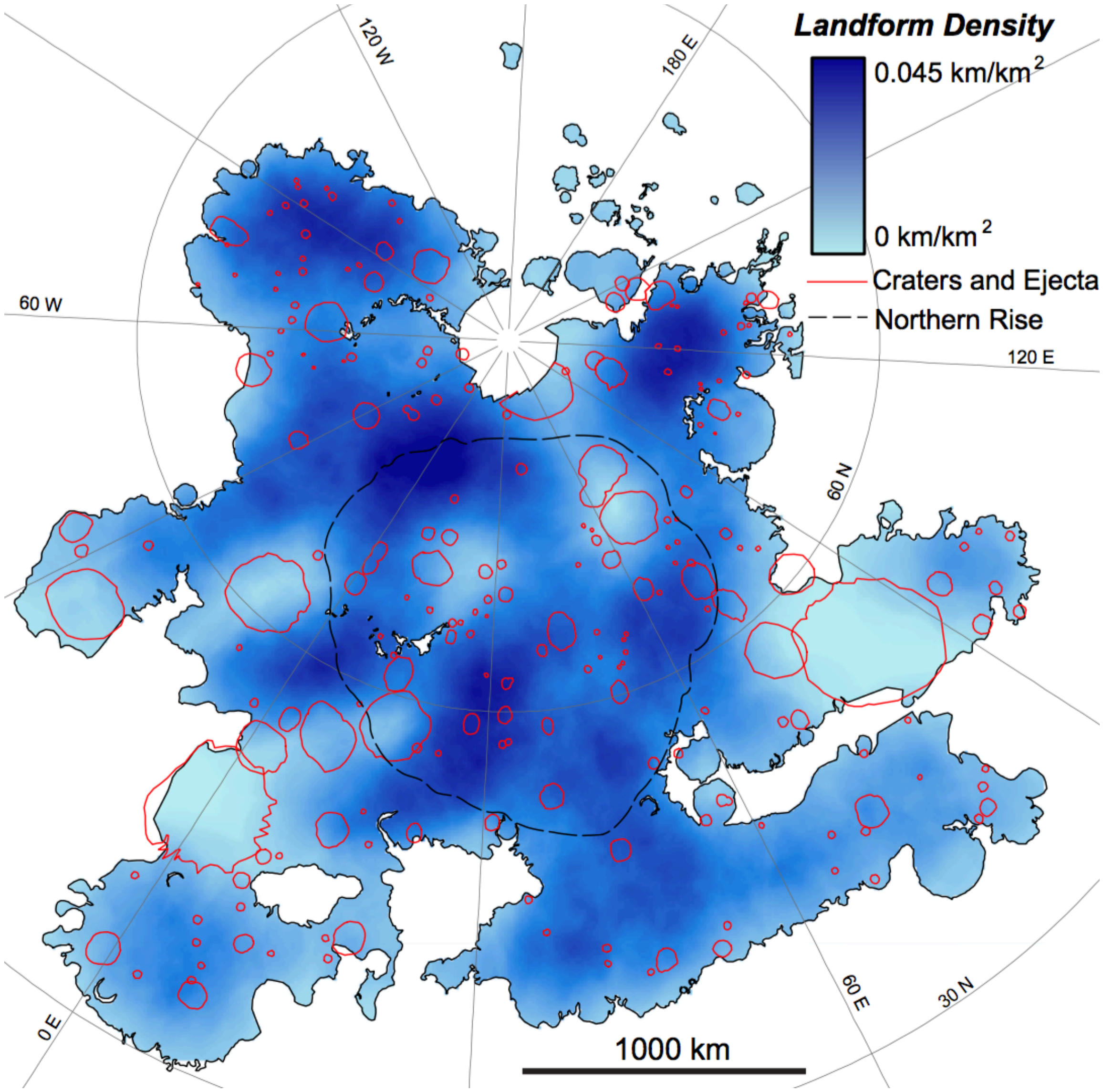

Figure 3.9 Map of density of shortening landforms across the northern plains, with higher densities displayed in darker shades of blue. Landform density is expressed in kilometers of landform length per square kilometer (km/km^2). Craters and crater ejecta are outlined in red, the northern rise is outlined in a black dashed line, and the northern plains are outlined in solid black. Map is shown in stereographic projection centered at 30° E, 66° N. We observe denser regions of landforms to be found near the pole and in locations that lack large impact craters. We observe regions with fewer landforms to be those dominated by impacts. In particular, regions near the Mansurian craters Stieglitz, Gaudi,

Rustaveli, Sor Juana, Abedin, and Sousa (dated by Kinczyk et al., 2016) host very few thrust fault-related landforms. We do not observe any patterns in landform density associated with the northern rise.

The density of thrust-fault related landforms is greatly reduced near large superposing craters such as Rustaveli and Sousa, which can be attributed to resurfacing and superposition of the associated ejecta blanket above thrust fault-related landforms. A higher density of landforms is also observed north of 70° N. Regions of greater landform density occur where few or small impact craters have been recorded, and thus, little resurfacing of those landforms has occurred. Because impact cratering reduces away from the ecliptic (Knibbe and van Westrenen, 2017), it is no surprise that the poles have fewer impacts.

We also compare the density of structures to the northern rise (Zuber et al., 2012). The northern rise is a dome-shaped uplift with a peak elevation of ~1.5 km and diameter of ~950 km estimated to postdate the northern plains emplacement (shown in Figure 9). We do not observe any trends in density associated with the northern rise, which further supports that the uplift of the northern rise postdated the growth of the landforms in the northern plains (Dickson et al., 2012; Klimczak et al., 2012).

<u>Orientation of structures</u>

One aim of this study was to analyze the orientations of thrust fault-related landforms in the northern plains. This analysis was conducted by observing patterns recorded in representative rose diagrams across the plains. Again, fault traces and anticlines not associated with fault traces were divided into 1.5 km segments, and the azimuth of each was calculated. As with the density calculation, the separation of anticlines and anticlines associated with fault traces and the division of landforms into segments was done to prevent weighting our calculations toward landforms with both anticlines and surface break traces or toward short landforms. We divided the northern plains into 20-degree by 20-degree bins. This bin size was chosen because it was large enough to (1) capture enough data points in each bin to feel confident in the calculated diagrams and (2) to prevent an effect of circularity from the largest impact craters. For example, if thrust fault-related landforms as part of a ghost crater were the only landforms in a bin, then the rose diagram would be expected to be nearly perfectly circular. However, if the bin size is larger than the diameters of the large ghost craters, then orientations attributed to any regional or global stress field as opposed to pre-existing topography would be detectable. We wrote computer code using R to sort azimuths into bins of 20° and created rose diagrams color coded by our confidence in the represented landform orientations. Where more segments were recorded, we felt more confident in prescribing the orientations indicated by the rose diagrams, and where fewer segments were recorded, we felt less confident in the orientations. We quantify our confidence only in the number of azimuths recorded (Figure 10).

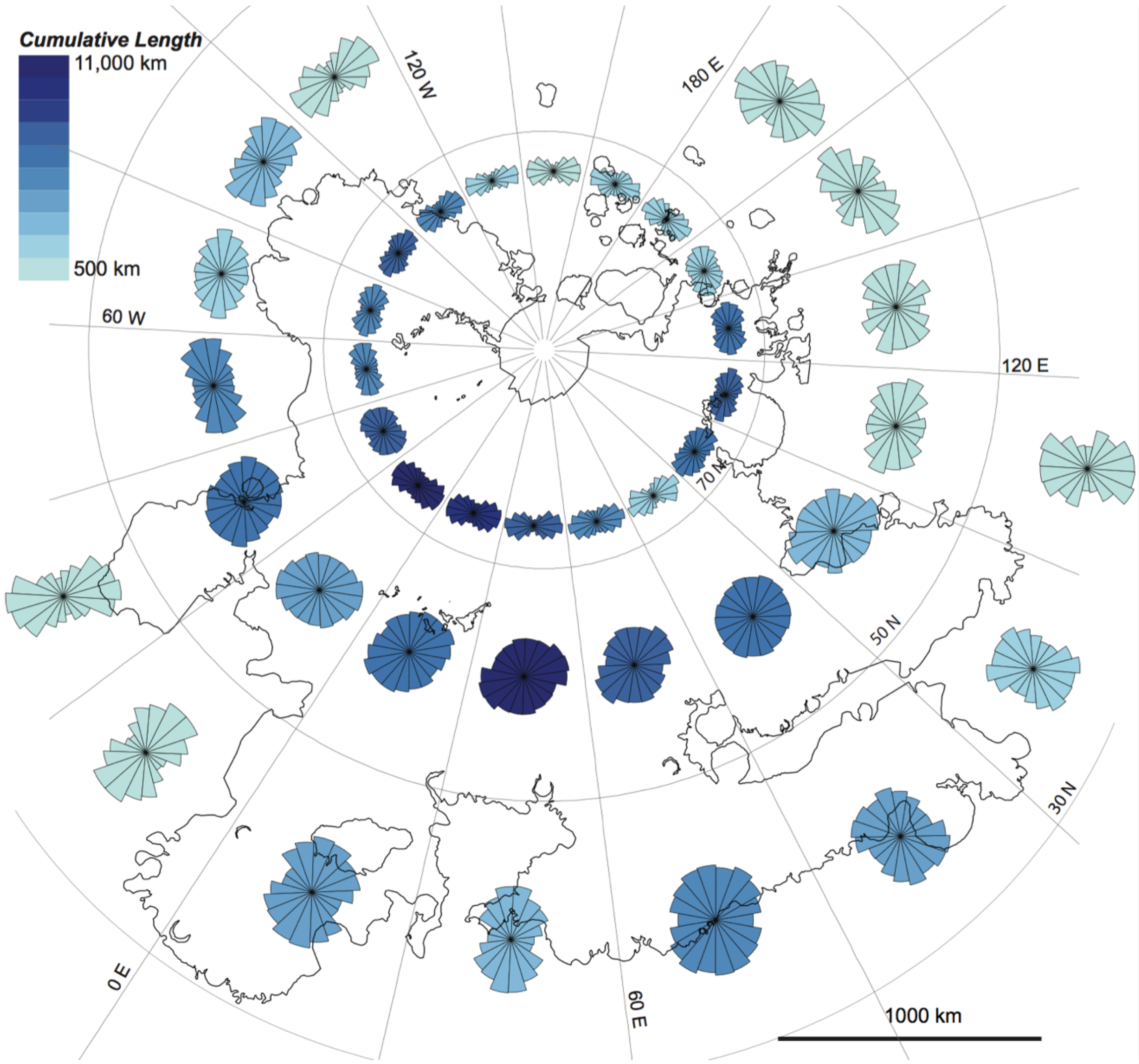

Figure 3.10 This map shows orientations of thrust fault-related landforms across the northern plains. Rose diagrams representing fault orientations within 20° latitude by 20° longitude bins are shown in blue and are oriented poleward. Deeper blues indicate more fault segments from which azimuths could be calculated, and therefore convey more confidence in the diagram. The map is shown in stereographic projection centered at 30° E, 66° N.

Rose diagrams generated from the orientations of fault segments showed a distinct bulls-eye pattern centered at the North Pole. From 90 to 70° N, faults are primarily oriented east-west. From 70 to 50° N, faults show no preferred orientation. In some bins in this latitude range, rose diagrams also appear to reflect mainly east-west landform orientations; however, these diagrams represent bins where only the northernmost portion of the bin contained northern plains units. Therefore, the patterns in these rose diagrams more closely reflect orientation trends from the 90 to 70° N latitudinal band. Between 50 and 30° N, landforms are predominantly oriented north-south.

Although we recognize that a multitude of global and regional-scale processes, such as tidal despinning, subsidence, reorientation, and changes in orbital parameters may have the potential to influence orientations of thrust faults, especially when operating in concert with global contraction, fault patterns have historically been discussed with a focus on tidal despinning. Many studies predict latitude dependent landform orientations if stresses related to tidal despinning contributed to the growth of the tectonic fabric (e.g. Pechmann and Melosh, 1979; Dombard and Hauck, 2008; Beuthe, 2010; Klimczak et al., 2015). In particular, tidal despinning was proposed to result in east-west normal faulting near the poles and north-south thrust faulting near the equator (e.g., Pechmann and Melosh, 1979). The interpretations from these models assumed that Anderson's Theory of Faulting was applicable to tensile stresses near the poles; however, tensile stresses produce jointing, not faulting (Klimczak et al., 2015). Furthermore, Klimczak et al. (2015) show that normal faulting is not induced at depths greater than ~20 km near 60° latitude as a consequence of increasing overburden stresses.

If all stresses were compressive (as is implied in Anderson's Theory of Faulting), to produce east-west oriented normal faults near the poles, stresses would have to be large enough to overcome the frictional resistance to sliding and thus can be assessed with the Coulomb Criterion. We find that magma or some other fluid would have been necessary in fractures to induce failure. If the east-west oriented thrust faults associated with landforms observed near the poles are not a product of reactivated normal faults but instead initially formed due to thrust faulting, then the presence of fluid in fractures, uplift, the removal of overburden possibly from a large impact, or added stress from global contraction would have been a prerequisite to rock failure.

Subsidence concentrates maximum horizontal compressive stresses within depressed regions such as those filled with volcanic deposits. This process is expected to result in an increased frequency of thrust fault related-landforms within volcanically flooded impact basins and specific to Mercury, within the northern plains as a whole (Watters et al., 2009; Freed et al., 2012). The Caloris impact, which modified a substantial area of Mercury, is thought to have taken place before the emplacement of the smooth plains (Fassett et al., 2009). Models of reorientation of Mercury due to the loading of the Caloris basin predict horizontal tensile stresses oriented north-south in the northwestern and southeastern hemispheres (Matsuyama and Nimmo, 2009). These models also predict horizontal compressive stresses oriented north-south in the northeastern and southwestern hemispheres (Matsuyama and Nimmo, 2009). Sufficiently large stresses from reorientation alone therefore would have caused hemispheric differences in fault type, but not orientation. Some changes in orbital parameters, such as those that induce changes in tides on the Moon (Watters et al., 2015b), may have caused similar changes in solar tides for Mercury. These stresses while not great enough to cause faulting, may have contributed to changes in fault orientation. Since patterns caused by these sources have not yet been predicted for Mercury, we cannot compare them to our observations.

As has been previously suggested for Mercury (e.g. Dzurisin, 1978; Dombard and Hauck, 2008; Matsuyama and Nimmo, 2009; Klimczak et al., 2015) and for the Moon (e.g. Watters et al., 2015b) some combination of the aforementioned processes likely acted in concert to influence the type and orientations of tectonic landforms to varying degrees. The timing of these processes is critical to establishing the geologic history of Mercury, and that timing can be discerned by comparing observations of tectonic patterns with those predicted to result from stresses associated with those geologic processes, either individually or in concert. Because the northern plains have been dated to ~ 3.7 – 3.9 Ga (Denevi et al., 2013; Ostrach et al., 2015), opening mode fractures must have been present around this time in order to facilitate the movement of large amounts of volcanic materials to the surface. It is possible that pre-existing favorably oriented discontinuities were reactivated after the formation of the northern plains, and so patterns and orientations within the plains may be basement-controlled and thus reflective of earlier processes.

We propose two possible geologic histories for Mercury that may explain our observations: one in which reorientation due to the Caloris impact occurs and one in which it does not. Because the pattern of thrust fault-related landform orientations is circumpolar, the first scenario requires any major reorientation of the planet due to the Caloris impact to have predated tidal despinning or any other process that influenced the pattern of faults at the north pole. After reorientation, tidal despinning and/or these other processes established a tectonic fabric of east–west oriented lithospheric weaknesses. As impacts shaped the heavily cratered terrain, a regolith layer developed across Mercury. The opening mode fractures and normal faults associated with reorientation, tidal despinning, and/or other processes may have facilitated effusive volcanism that formed the smooth plains. A lack of smooth plains in the southern hemisphere (Denevi et al., 2013) could indicate that reorientation due to the Caloris impact caused preferential faulting and therefore opening of magma pathways in the northern hemisphere. These discontinuities also contributed to the orientations of thrust fault-related landforms that would later characterize the northern plains, either via reactivation of normal faults or as basement-influenced deformation. The deformation style of these particular landforms is discussed in more detail below.

In the second scenario, in which reorientation due to the Caloris impact did not occur, tidal despinning or any other processes influencing fault patterns cannot be temporally tied to the Caloris impact. But even in this scenario, fault reactivation and basement-controlled deformation facilitated on structures established by global contraction and tectonic processes predating plains emplacement could have influenced fault orientations within the northern plains. If however, orientations or faults within the smooth plains were not influenced by pre-existing basement faults, then the processes responsible for the observed tectonic pattern must have been active after plains emplacement.

Previous authors have also found through analysis of thrust fault-related landform orientations that tidal despinning likely played a role in the development of Mercury's global tectonic fabric (Watters et al., 2015a). Other studies have suggested that the tectonic patterns, including orientation and density of landforms, observed could have resulted from despinning along with mantle downwelling, pole reorientation, and/or changes in lithospheric thickness (e.g. King, 2008; Matsuyama and Nimmo, 2009; Beuthe, 2010). Beuthe (2010) does not find a region of strike-slip tectonics at the mid-latitudes, but instead, produces a model with a mid-latitude transition between north-south oriented thrust faults and east-west oriented thrust faults, similar to the mapping results of this work. King (2008) suggests that mantle downwelling concentrates the locations of lobate scarps, a conclusion supported by Watters et al. (2015a). We do not find any evidence to support this conclusion. Aside from evidence of faulting removed by impact cratering processes, we do not observe any pattern in fault density.

Thin-skinned vs. thick-skinned deformation in the northern plains

One goal of this study was to determine the subsurface fault architecture and tectonic style associated with deformation in the northern plains. We aimed to determine if shortening was confined to the plains units or if it extended into the basement. On Earth, if surficial units are mechanically decoupled from units below due a weak layer, deformation is accommodated in the upper units, and the style of tectonism is referred to as "thin-skinned" deformation (Chapple, 1978). The northern plains may be underlain by a weak, regolith layer developed through impact processes (Marchi et al., 2013) that was later buried by volcanism. On the contrary, if faulting roots deep into the basement, the style of tectonism is called "thick-skinned" deformation (Coward, 1983). A third style implies a structural link between the basement and upper units where faults within the basement may contribute to orientation and development of faults in the upper units, and this style of tectonism is called "basement-involved thin-skinned" deformation (Pfiffner, 2017). Basement-involved thin-skinned tectonism occurs in locations such as the Central

Apennines of Italy, the Jura fold and thrust belt in France, and the northwestern portion of the Taiwan fold and thrust belt (Tozer et al., 2001; Lacombe et al., 2003; Madritsch et al., 2008). In these mountain belts, faults in shallow layers develop above, but are linked to older (pre-existing) faults in the basement while overall displaying tectonic styles associated with thin-skinned deformation.

We observe compound landforms that by analogy with landforms seen on Earth and other planets and/or models, primarily reflect thin-skinned tectonics (see section 3). A weak layer of regolith deposited before effusive volcanism took place may have produced the décollement necessary to partition strain into the plains units only. Detachment thrust faults could propagate upward from this décollement or from the interface between volcanic units and impact crater walls and floors. Faults following crater rims, broad linear to arcuate rises of equal width, parallel evenly spaced ridges, and changes in vergence all imply the presence of faults that root to shallow décollements. Sigmoidal rises may be related to linkage of low angle thrust faults, but require steeply dipping but not necessarily deep faults for connectivity. V-shaped rises may reflect faults that root to the base of thin or thick upper units, and require fault interactions at some depth.

Aside from our analysis of analogues and models, our fault orientation analysis indicates that thrust-fault related landforms could have inherited their orientations from buried, pre-existing faults and other weaknesses that formed prior to emplacement of the northern plains but were reactivated at a later time. Sigmoidal rises interpreted to be step-overs and restraining bends likely develop their orientations from the process of transfer of slip between faults, and faults propagating along crater walls are proposed to draw their orientations and curvature from the interface of the crater wall and overlying volcanic unit itself. However, as described above, V-shaped rises, broad rises, proposed fold and thrust belts, and landforms with changes in vergence are all indicative of landforms underlain by faults rooting to shallow décollements. The regolith-related contact between the cratered terrain basement and volcanic flood units could function as one such décollement. If the orientations of thrust faults beneath these landforms reflect possible geologic processes that deformed the basement rocks and could have allowed for the emplacement of effusive volcanic deposits, then it is possible that thrust fault orientations and locations are inherited, or controlled, by basement faults. Deformation in the northern plains could therefore be more accurately represented with basement-involved thin-skinned tectonics instead of thin-skinned tectonics alone. If deformation is not related to basement faults, then the geologic processes resulting in the observed tectonic pattern must have occurred after the emplacement of the volcanic units. The degree of involvement of basement faults should be tested in the future by fitting finite-element models or forward fault-geometry models to topography.

Conclusions

We produced a detailed map of anticlines and fault scarps within the northern plains in order to describe common shortening-related landform morphologies in the region to distinguish between thin- and thick-skin deformation styles. The orientations of landforms across the northern plains helped us to establish the relative timing of northern plains emplacement with respect to processes that may have lead to the observed landform orientation, such as tidal despinning and pole reorientation.

Thrust fault-related landforms of the northern plains were mapped using MESSENGER datasets in unprecedented detail. Combining our structural interpretation of map patterns and imagery allowed for the interpretation of landform geology. Five compound landforms and one common structural characteristic were identified, all of which support a model of basement-involved thin-skinned deformation within the northern plains volcanic unit. As faults grew, they likely rooted into a regolith décollement producing pop up structures of approximately equal width and anticlines with opposing vergence. Locally, thin regolith may have allowed for a stronger décollement. The presence of this décollement combined with an early rapid pulse of global contraction, could have produced the development of relatively narrow fold and thrust belts. Flooded and buried impact craters and basins may have localized stresses along their walls and rims, contributing to the development of wrinkle ridge rings. These same craters, basins, but also other areas, especially those coinciding with gravity lows redirected fault surfaces producing v-shaped rises. As some faults propagated towards each other, sigmoidal rises interpreted as step-overs linked the faults and accommodated oblique slip. Some other geological process(es) besides global contraction, such as tidal despinning, influenced the orientations of faults underlying these landforms, contributing to latitudinal patterns in fault orientation. If the process were tidal despinning, it may have occurred very early, deforming the lithosphere to produce opening mode fractures and normal faults, and allowing for the emplacement of the northern plains. These weaknesses were later reactivated as thrust faults during global contraction, or as basement faults, they influenced the orientation and location of thrust fault propagation.

Acknowledgments

CK was funded by the Discovery Data Analysis Program under grant NNX16AK23G.

CHAPTER 4

A 3-D STRUCTURAL MODEL OF THE SADDLE MOUNTAINS, YAKIMA FOLD PROVINCE, WASHINGTON, USA: IMPLICATIONS FOR LATE TERTIARY TECTONIC EVOLUTION OF THE COLUMBIA RIVER FLOOD BASALT PROVINCE[3]

[3]Crane, K.T. and C. Klimczak. 2019. *Tectonophysics. Submitted.*
Reprinted here with permission of the publisher.

Abstract

The Yakima Fold Province (YFP) is a series of asymmetric, north-verging anticlines in the Columbia River Flood Basalt Province of south-central Washington. Ridges represent anticlinal folds produced by tectonically active thrust faults, and their proximity to the Hanford nuclear facility has motivated many studies on the timing and extent of Quaternary deformation within the folds; however, multiple generations of faults and folds in the region have recorded a history of deformation spanning ~50 Ma. In this work, we utilize ~44 km of seismic profiles, structural orientation measurements collected in the field, USGS geologic maps, and stratigraphic information collected from 13 well logs to investigate the subsurface structure of the Saddle Mountains in the northern section of the YFP. We developed a three-dimensional structural model of the mountain range and estimated displacement and strain accommodated by faulting and folding. Our resulting model requires a multi-stage deformational sequence, and indicates that ~1800 m of uplift is generated by two parallel listric faults, soling into décollements at ~4 and ~8 km depth. Patterns of displacement and orientations of strain suggest that the deeper fault is older and that it may reflect a history of clockwise rotation, making the YFP the shortening counterpart to the extensional northern Basin and Range.

Introduction

The Yakima Fold Province (YFP) is a series of sub-parallel, mostly north-verging, asymmetric anticlines in the Columbia River Flood Basalt Province of south-central Washington. The mostly east–west striking fold system lies within the western Columbia Basin, bounded to the east by the Palouse Slope and to the west by the Cascade Range

(Swanson et al., 1980). Today, the YFP is cut by the Columbia and Yakima Rivers. Rock uplift is accommodated through anticlinal folding and thrust faulting. Exposures of these structures as well as gravity, magnetic, well, geochronologic, and limited seismic data have supported our understanding of the fault geometry and timing of rock uplift (e.g. Reidel, 1984; Blakely et al., 2011; Casale and Pratt, 2015; Kelsey et al., 2018).

The east−west striking anticlinal ridges suggest north−south oriented shortening and maximum horizontal compressive stresses that have been attributed to Oregon Coast Block deformation during clockwise rotation of the North American Plate relative to the obliquely subducting Juan de Fuca Plate (e.g. McCaffrey et al., 2016; Unruh and Humphrey, 2017). Block motion models predict an Euler pole in northeastern Washington (Brocher et al., 2017) or the tri-state region of Washington, Idaho, and Oregon (McCaffrey et al., 2016; Unruh and Humphrey, 2017). These Euler Pole locations are derived from GPS measurements and structural analyses and predict that stresses and deformation increase to the west and structures align radially from the pole (Unruh and Humphrey, 2017). The block rotation models do not fully explain the mostly northward vergence of many of the anticlines within the YFP, such that more recently, a conceptual model proposing a slab tear along the Cascadia subduction zone and onset of asthenospheric flow has been invoked as an explanation for more recent north–south oriented compressive stresses (Staisch et al., 2017).

Block rotation models suggest that stresses began to build up ~15–16 Ma ago (Wells and McCaffrey, 2013; McCaffrey et al, 2013; 2016), approximately coeval with the initiation of basalt emplacement. Field studies suggest that deformation was coincident with the flow emplacement ~16 Ma (e.g. Reidel, 1984). Geochronologic studies of alluvial fans and strath terraces adjacent to the ridges propose that the majority of deformation occurred less than ~10 Ma ago, with fastest rates of uplift starting ~6 Ma ago (Kelsey et al., 2017; Staisch et al., 2018; 2017).

Structural analyses previously treated anticlines in isolation and in sequence to describe the faults and folds responsible for uplift. Cross sections derived from gravity and magnetic data and geologic maps indicate that thrust faults below the ridges extend ~8 km into basement rocks (e.g. Blakely et al., 2011; Staisch et al., 2018). Fault geometries range from smooth, arcuate fault surfaces dipping ~40°S with multiple branching conjugate thrusts (Blakely et al., 2011) to ~30° ramps interrupted by ~6 km wide flats at ~4 km depth (Staisch et al., 2018). Casale and Pratt (2015) infer from seismic data that two sub-parallel listric faults may form the ridges, with the more near-surface listric soling into a décollement below the southern slope of a ridge at ~4 km depth. The deeper fault in this two-fault model extends to a décollement at ~8 km depth. Field studies comparing folds of basalts to faults propagating through the flows also suggest deep structures (e.g. Campbell, 1989; Pratt, 2012). Conjugate thrust faults are commonly described, and fold geometry has been described as open to tight along the anticlines with folds occasionally displaying overturned limbs adjacent to thrust fault exposures (Reidel, 1984).

Our work links and expands on studies of uplift geometry and timing by developing a three-dimensional (3D) model of folded basalts and their associated faults before erosion. We interpret a dynamic, multi-stage evolution of folding and describe the relative timing and amount of uplift associated with a ridge using over 44 km of seismic profiles, well data, geologic maps, and field data. Understanding the cause and timing of uplift and the structural geometry allows for predicting modern earthquake frequencies and magnitudes. This is critical for the YFP. The Hanford Nuclear Site is located near several tectonically active Quaternary Yakima folds and the province may be structurally connected to a regional-scale mostly blind strike-slip structure, the Olympic-Wallowa Lineament that extends below the Seattle area and into the Puget Sound (Blakely et al., 2011; Pratt, 2012; Sherrod et al., 2016). Structural details also permit us to evaluate the regional tectonic context of the Cenozoic Pacific Northwest through a lens of the deformational record within the Yakima folds. Characterizing structural geometry also provides key insight into deformational processes in flood basalts, making the Yakima folds a useful analogue for folds observed in basalts on other planetary bodies (e.g., Crane and Klimczak, 2019).

Methods

Our primary goal is to interpret the history of deformation within the YFP. We illuminated specific details of structural development by generating a 3D model of faults and folds with displacement and strain visualized on these surfaces. We chose to analyze the structure of a ~65 km length of the Saddle Mountains (Figure 1) within the YFP based on availability of migrated seismic data and outcrop accessibility. The 3D model was developed by interpolating structures across 10 cross sections produced from field, seismic, well, and geologic map data.

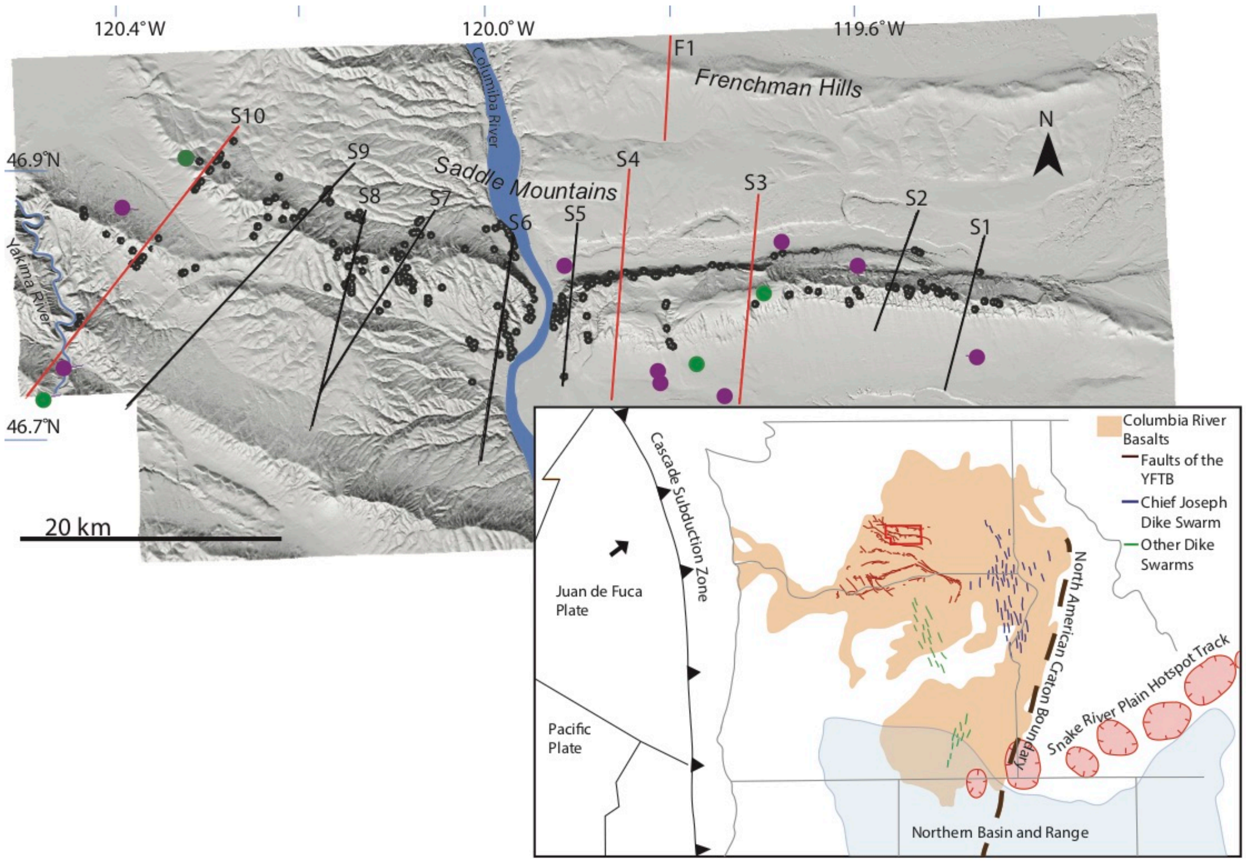

Figure 4.1 Hillshade map of our study area highlighting the Saddle Mountains with inset map of Pacific Northwest for regional tectonic context. The northern extent of the Columbia River Flood Basalt Province is shown in tan and Quaternary faults are displayed in crimson (United States Geological Survey, 2006). On the hillshade, black lines indicate cross sections without seismic profiles, and red lines indicate cross sections that contain seismic profiles. Sections S1–S10 cross the Saddle Mountains and are available in supplementary materials. Section F1 crosses the Frenchman Hills. Only structure was interpreted for this section, and it is not included in our 3D model. Purple and green circles represent respective locations of shallow and deep wells that provided stratigraphic information for cross section construction. Small black circles atop the hillshade represent locations of orientation data collected in the field. A more detailed

map with strike and dip symbology and field photos is available in the supplementary materials, and can be directly opened in Google Earth for viewing. Inset map displays regional tectonic and volcanic features such as boundaries for the Juan de Fuca Plate, Cascade Subduction Zone, Northern Basin and Range, and North American Craton (adapted from Camp, 2013 and Staisch et al., 2018).

Fieldwork

The Saddle Mountains is a ~110 km long segmented, north-verging anticline in the northern YFP. The ridge is cut by the Columbia River near Beverly, WA. East of the river, mass wasting events and drainage channel development have exposed basalt outcrop along the east−west striking anticline. West of the river, the anticline trends east−southeast and outcrop is exposed by mass wasting events and road cuts. The westernmost part of the Saddle Mountains is deflected northwest. To the south, Manastash Ridge continues east−southeast toward the Yakima River.

Three primary Columbia River Basalt members are exposed in the Saddle Mountains: the Grande Ronde Basalts (16 Ma−15.6 Ma), the Wanapum Basalts (15.6−15 Ma), and the Saddle Mountains Basalts (15.0−6 Ma; Reidel et al., 2013). Each member is comprised of chemically distinct flows described in the literature (e.g. Swanson et al., 1979). Sedimentary interbeds representing pauses in volcanism separate some flows and support identification of flow units in the field. Descriptions of a few distinct flows and sedimentary interbeds make it possible to identify the member given context from geologic maps. For example, Grande Ronde Basalts form the thickest sequences of flows, and are capped by the very light-colored sedimentary Vantage Member of the Ellensburg Formation (Reidel and Tolan, 2013). The Roza Member of the Wanapum Basalts has 2–5 mm long plagioclase phenocrysts in parts of the flow distinguishing it from other Wanapum flows and is separated from the Priest Rapids Member of the Wanapum Basalts by the Quincy diatomite deposits (Tolan et al., 2009).

We traversed the Saddle Mountains and collected orientation measurements of planes inferred to have been horizontal during basalt emplacement (Figure 2). These surfaces include sedimentary interbeds and upper contacts between sedimentary or ash layers and basalt flows. We also measured orientations of vesicle layers, major contrasts between sections of flows, flow tops, and planes perpendicular to well-developed colonnade and parallel to the long axis of oblate basalt pillows (see in Figure 2: Aubele et al., 1988; Reidel et al., 2003; Sheth, 2017). No assumptions were made about the original horizontality for flow bottoms, as these may have been emplaced atop pre-existing topography.

We collected a total of 384 measurements using Midland Valley's *Clino* application for smartphones. The location of the measurements is shown in Figure 1, the measurements are provided as *.kmz files in the supplementary material. This *Clino* application is a digital geological compass and records georeferenced measurements and photographs that can be exported directly to the associated software modeling package *Move* or Google Earth. Each measurement was recorded with the basalt member in which it was collected and the type of surface it was taken upon. We also took 300 geo-referenced photographs (provided in the supplementary *.kmz files), and recorded hundreds of field observations and sketched the geometry of the folds where exposed. The Washington Division of Geology and Earth Resources smartphone application *Washington Geology* was also utilized in the field. The application allowed us to compare our orientation measurements in real time with previously collected measurements from published geologic maps. Where our orientation measurements differed substantially from the published data, we took additional measurements to increase our confidence in our interpretation. For example, on the western side of the Columbia River near cross section S6, the 1:24,000 geologic map (Washington Geological Survey, 2017) indicates vertical bedding. From a distance, these units do indeed appear vertical, but upon inspecting the outcrop, we observed that these units only appeared vertical, but were actually only slightly dipping. A differential weathering pattern had affected their ability to be interpreted from a distance (Figure 3). For most measurements, our measurement was very similar to the published measurement, and because our dataset was more extensive than the available data, we chose not to utilize previously published basalt orientation measurements.

Figure 4.2 Field photographs exemplifying exposures and surfaces upon which orientation measurements were collected during fieldwork. (A) This westward view of

the western Saddle Mountains highlights a broad exposure of folded basalts above the Columbia River. Folded basalts appear to drape horizontal strata; however, this is an effect of the perspective at which the photo was taken. Tilted well-developed columnar basalts (B and C) were also used to inform our cross sections as planes perpendicular to their surfaces indicate the amount of rotation that has taken place. The tilt or dip of these planes is symbolized with an arrow. Similarly, oblate pillows (D) which were emplaced with the widest dimension oriented horizontally were used to determine the dip of the basalt strata.

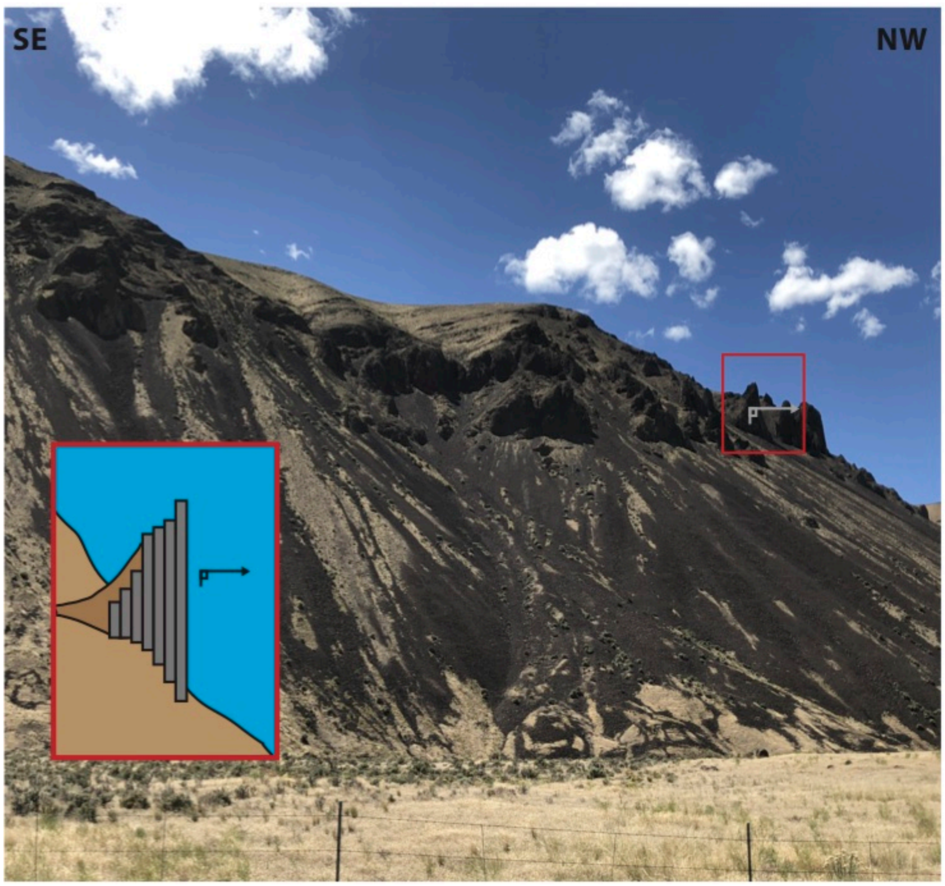

Figure 4.3 This figure shows a photo of the northern slope of the Saddle Mountains just west of the Columbia River (fence for scale) and an inset digitized field sketch. The dark basalt units appear to be vertically oriented spires from a distance, but closer observation

shows that the upward jutting rock is actually nearly horizontally oriented columnar basalt that has weathered into fin-shaped outcrops.

Seismic Interpretation and Wells

We obtained and interpreted four migrated seismic profiles. Three profiles cross the Saddle Mountains—two transect the mountains east of the Columbia River (S3 and S4) and one crosses the mountains west of the Columbia River (S10). The fourth profile crosses the Frenchman Hills (F1), the ridge directly north of the eastern section of the Saddle Mountains (Figure 1). Profile lengths are 9.5 km, 18.7 km, 11.5 km, and 14 km. For comparison, Casale and Pratt (2015) previously interpreted a ~22 km seismic profile near S5. Profiles along S3, S4, and F1 were produced by Arco Oil and Gas Company using Vibroseis equipment and shot intervals of 75 feet. They were filtered using low pass, Automatic Gain Control (AGC), and Normal Move Out (NMO) filters, and were migrated using post-stacking finite difference (30-degree) methods. The profile along S10 was produced by Shell Western E&P, Inc. using dynamite and shot intervals of 75 feet. Data was filtered using low and high pass, AGC, and NMO filters, and was migrated using a post-stacking Kirchoff migration. Seismic Exchange, Inc. provided the propriety migrated profiles and Society of Exploration Geophysicists (SGY) format files. The software was used to visualize the SGY files and convert vertical time axes to depth, a conversion process which the software can also complete using the Root-Mean-Square (RMS) velocities provided in the Arco profiles. Each of the seismic profiles extends to ~9 km depth. We also used the *Move* software to interpret the profiles.

We identified faults, folds, and specific strata within the seismic data. The upper 200 m of reflections were difficult to interpret due to the multitude of fractures and discontinuous reflections. Below a few hundred meters, interpretation was based on continuity, amplitude, and spatial relationships of reflections. Folds were identified by arcuate reflections, and faults were identified by offset reflections. Horizontal reflections adjacent to tilted reflections were interpreted to be undeformed footwall strata juxtaposed to tilted hanging wall strata. A combination of water well logs and oil and gas well logs (Figure 1, purple and green circles) provided stratigraphic information that allowed us to tie our seismic reflections to specific basalt flows.

In particular, five oil and gas wells contained specific stratigraphic information. We used this information to directly link specific basalt members with reflection characteristics and indirectly link rock descriptions from shallower nearby water wells to named units in the oil and gas wells. For example, a ~1456 m deep well drilled by Boyles Bros. with identified stratigraphy provided constraints for classifying rock units in a ~342 m deep nearby water well. Units in the water well log were also described in detail by the drillers. A combination of rock descriptions from the drillers and approximate depths from the Boyles Bros. well allowed us to interpret the stratigraphy of the drillers log. Ten water wells less than ~1 km deep allowed us to constrain the depths of surface units and distinguish boundaries between flows using rock descriptions in the well log. All wells were located using the Geologic Information Portal of the Washington State Department of Natural Resources, and locations, depths, drilling information, stratigraphic tables, and direct links to well logs are provided for each well in the supplementary material.

Four oil and gas wells contain stratigraphic information about rock units beneath the Columbia River Basalts. The Yakima Minerals Well 1-33 (Shell Oil Company, 1983) lists the Swauk Formation as the deepest unit. The Swauk Formation is primarily subquartzose sandstone dating to ~59–51 Ma (Tabor et al., 1984; Eddy et al., 2006) and may be up to 8 km thick (Eddy et al., 2006). Where the formation outcrops north and west of the Columbia River Basalts, it has been observed to be folded and unconformably overlain by the relatively undeformed Teanaway Formation of basalt and andesite (~47 Ma) and Roslyn Formation (~ 45.9 Ma, Tabor et al., 1984). The Roslyn Formation consists of thickly-bedded sandstones interbedded with coals and siltstones (Tabor et al., 1984), and is observed in four of the oil and gas well logs, including the Yakima Minerals Well 1-33, BN1-9 (Shell Western E&P, Inc., 1984), AF1-6 (Delta Petroleum Corporation, 2006), and 23-35BN (Meridian Oil, Inc., 1988). Above the Roslyn Formation, the ~33–34 Ma Wenatchee Formation consists of volcanic tuff and is recorded in the BN1-9 and AF1-6 wells. The BN1-9 and AF1-6 wells align with our seismic profile along cross section S3, and Yakima Minerals Well 1-33 and 23-35BN are located along cross section S10. We characterized the seismic reflection of the Roslyn and Swauk Formations, and were therefore able to interpret their location on the seismic profiles in sections S3, S4, and S10. In these cross sections, we observed patterns of deformation within these deeper units reflected in upper units and surface structural geometries. We were thus able to extend our interpretations of formation surfaces to other cross sections. The seismic reflections associated with the Wenatchee Formation were so discontinuous that we did not feel confident interpreting the unit across the available seismic data.

Model Development

We used Midland Valley's *Move* Software to generate our 3D model of structures within the Saddle Mountains. *Move* and similar structural geology modeling software packages allow for calculating and visualizing deformation-related parameters, especially where fault parameters vary over the study area (e.g. Bigi et al., 2013; Perrouty et al., 2014; Watkins et al., 2014; Muir, 2017; Linnros et al., 2019). *Move* allows the user to import, display, and manipulate shapefiles and field data collected with *Clino* in its graphical user interface. We imported a regional 10 m Digital Elevation Model and generated a hillshade. Two geologic maps (Reidel, 1988; Schuster, 1994) containing contacts, faults, and folds at 1:100,000 and 1:24,000 scales were loaded into *Move* followed by the structural data that we collected in the field. Field data and map information of geologic contacts, faults, and folds were projected onto the hillshade.

The combination of field data, mapped surface geology, seismic sections, and wells allowed us to construct 10 line-balanced cross sections of the Saddle Mountains (S1–S10, Figure 1). Details on observations and interpretations are provided with each cross-section in the supplementary material. *Move* contains functionality that allows the user to determine optimal cross section orientations based on imported data. The orientation data near the desired location of the cross section are plotted on a stereonet, and the plane most nearly perpendicular to the strike measurement is chosen. Field data were used to determine the orientations and locations of seven cross sections, while remaining sections are coincident with seismic profiles and near deep oil and gas wells. Structural field data and wells were projected onto cross sections within ~5 km of the data location. Data within ~5 km of cross sections but which clearly would not reflect the structures within that section were not projected. For example, data points collected in the east–west striking segment of the mountains were not projected onto profiles in the east–southeast striking segment. Topography and intersection points of contacts and structures from geologic maps were captured along cross section lines.

For cross sections containing seismic interpretations, strong reflections, strata defined by wells, and faults were identified first. Although the Frenchman Hills seismic profile was not included in the model, it was interpreted to provide additional context for the model (F1, supplementary material). Any fault visible in the seismic data but not breaking the surface was noted, and folds visible at the surface associated with those blind faults were identified. If these folds extended across other cross sections, the fault was inferred to transect these sections as well. Line-balanced cross sections were then constructed using well data, structural field measurements, and surface geology. As previously described, stratigraphy available in well logs allowed us to characterize the flow units based on the visual properties of their seismic reflections. For example, the upper portion of the Roslyn Formation was characterized by 3–4 high amplitude, continuous reflections, and the Swauk Formation was characterized by many folds along the lower portions of the seismic profiles. We used a surface creation tool within *Move* to interpolate the top of the Grande Ronde flows, tops of the Priest Rapids and Frenchman Springs Wanapum flows, and major faults observed across the sections. We then described the geometry of the faults, calculating their length, depth, shape, and range of dips. We observed the geometry of the folds associated with faults. For specific descriptions of each of the cross sections, the reader is referred to the supplementary text.

Displacement and Strain Analysis

Faults and their associated folds evolve together over time. As faults grow in length, displacement along fault surfaces increases, with maximum displacement predicted at the midpoint of the fault length (Cowie and Scholz, 1992). Layer parallel shortening and flat-ramp fault geometry result in anticlinal folding above the upper fault edge, known as fault-propagation folding (Storti et al., 1997). Fault slip and associated strain is transferred into fault-propagation folds. Flat-ramp-flat fault geometries result in fault-bend folding. Fault-bend folds consume fault slip primarily near kinks in fault geometry, not necessarily along the upper fault edge (Suppe, 1983). Displacements accommodated by faults and folding are intimately tied to one another, and both must be evaluated to produce a complete model for deformational history.

We used the model described above and *Move*'s Geomechanical Modeling Package to calculate deformation-related parameters for the Saddle Mountains. The Geomechanical Modeling Package applies mass-spring algorithm, an iterative numerical technique, to minimize the strain in a solid body of rock, and then compares the strained and strain-removed surfaces to calculate strain-related parameters (Terzopoulos et al., 1987; Provot, 1995; Baraff and Witkin, 1998; Wang, et al., 2006). We calculated the horizontal and vertical displacement, or heave and throw respectively, on the faults by defining the intersections of hanging wall and footwall strata with faults and determining the distance between these intersections. We were also able to retro-deform or "unfold and un-slip" the reconstructed surfaces of the Grande Ronde and Wanapum Columbia River Basalt flows, and therefore calculate strain, strain direction, and total rock uplift. We differentiate the amount of deformation accommodated by faulting and folding.

Because rock uplift is caused by folding and slip along thrust faults, subtracting vertical displacement due to faulting from total rock uplift discerns uplift or elevation change caused by folding alone. We mapped these values across the surfaces of the faults and folds to detect patterns in location or intensity of deformation.

Results

Structural Geometry

The series of cross sections reveals a 3D structural system of listric thrust faults, conjugate thrust faults, and varied folds (Figure 4). The main frontal thrust below the Saddle Mountains (Figure 4A) is often interpreted to break the surface (e.g. Reidel, 1988). We observe this listric thrust fault in seismic profiles to extend to ~4 km depth (4.4 km at the deepest) before soling into a décollement within the sedimentary Roslyn Formation. We recognize this fault due to offset reflections extending toward the mapped surface break. The main frontal thrust fault produces the major displacement due to faulting of the Columbia River Basalt units and minor displacement due to faulting of the Roslyn Formation. This fault spans the entire length of our model (~65 km), and likely extends tens of km beyond the model boundary. Where the fault breaks the surface, the listric geometry is characterized by dips primarily between 32°S and 53°S, with a steepest dip of 66.5°S. These dips are taken directly from the model which is constrained by dips calculated from strike lines of surface-breaking sections of the fault on the geologic maps.

A second major thrust (Figure 4B) is also observed in seismic data, but is not mapped at the surface. This fault is evidenced by offset reflections at and near ~7.5 km depth and subsurface, north-verging folds. Offset dissipates stratigraphically upward until

~4–4.5 km where the fault and folds are capped by sub-horizontal strata which may be lower Roslyn Formation or basalts of the Teanaway Formation (45–47 Ma). This deeper fault is interpreted to propagate toward the surface in some sections, and its upper edge is located below an open anticline north of the main anticline. The long-wavelength fold morphology of the entire anticline, a general upward bowing of the topography we observe in many of the cross sections, overlies this lower fault. The fault extends the length of the model, with most dips between 31°S and 51°S and a maximum dip of 70°S. The two main thrusts are parallel. This system of two main faults beneath a anticline is also observed in the Frenchman Hills seismic profile (F1, supplementary materials).

We also identify two minor faults in seismic profiles. These faults are also present in geologic maps. A backthrust in the easternmost region of our model dips approximately 40°N, rooting into the upper listric thrust. This fault slightly shallows with depth, and extends to ~2.4 km depth. The modeled length is ~21.6 km; however, the fault likely extends a few hundred meters beyond the modeled boundaries. While this fault does not break the surface, the southernmost extent of the fault is located directly beneath a southward verging mapped anticline. A second conjugate fault located in the western region of our model does break the surface. This fault is currently mapped as two faults; however, we interpret a single fault with changing dip based on surface geometry of mapped folds and faults. The eastern portion of the fault dips ~45°S. It dips more shallowly near its length midpoint (~15°S) and steepens to ~45°N in the west as the fault transitions to dipping north. It is ~30.7 km long, and extends to ~1.9 km depth.

Folding style is variable along the length of the Saddle Mountains. Folds were observed by analyzing field photos (included in supplementary *.kmz file), sketches and shapes of reconstructed flow surfaces within the larger Grande Ronde, Wanapum, and Saddle Mountains Columbia River Basalts units. In the easternmost study area, we observe open box folds. Fold axial traces align with upper fault edges for the main fault and backthrust. In particular, a south-verging fold above the eastern backthrust is prevalent in S1–S3. Farther westward toward the Columbia River, folds transition into short-wavelength structures (less than ~2 km) superimposed on a broader, anticlinal structure (tens of km in wavelength, Figure 5, S3 and S4). Deeper folds associated with the lower listric thrust fault mimic this long-wavelength structure.

Immediately west of the Columbia River, folding style abruptly changes. A north-verging anticline dominates above the upper listric thrust fault with lower-wavelength folds overlying kinks in the fault ramp (Figure 5, S6 and S8,). The longer-wavelength structure of the fold mimics the transition from the ramp into a décollement at ~4 km as well as the geometry of the deeper thrust (Figure 5, S6 and S10). A north-verging open anticline overlies a minor thrust south of the major, upper thrust and is trailed by a long-wavelength syncline. Minor synclines are observed south of the main thrust fault superposed on the larger anticlinal structure. As the upper fault edge drops below the surface in the westernmost region of our study area, the main anticlinal fold becomes more symmetrical, and the steepening, conjugate minor thrust fault produces a more exaggerated south-verging fold (Figure 5, S10).

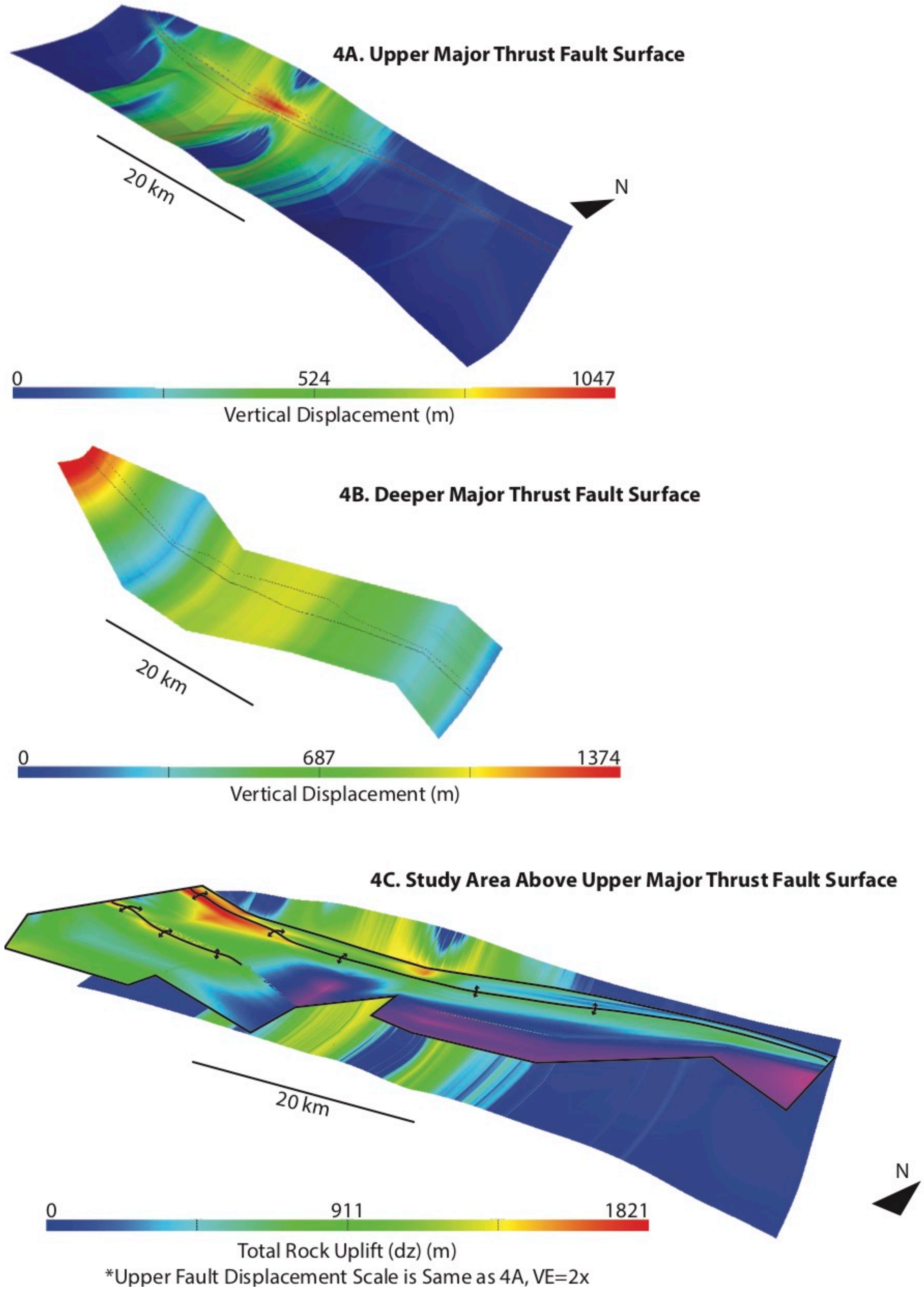
4A. Upper Major Thrust Fault Surface
20 km
N
0
524
1047
Vertical Displacement (m)
4B. Deeper Major Thrust Fault Surface
20 km
0
687
1374
Vertical Displacement (m)
4C. Study Area Above Upper Major Thrust Fault Surface
20 km
N
0
911
1821
Total Rock Uplift (dz) (m)
*Upper Fault Displacement Scale is Same as 4A, VE=2x

Figure 4.4 This figure shows reconstructed surfaces of faults and one folded basalt layer, with warmer colors indicating greater amounts of vertical displacement. (A) The major upper thrust fault displays a pattern of increased vertical displacement near its center, just west of the Columbia River. (B) The deeper major thrust fault also has a minor peak in displacement near this location, but overall displays increased vertical displacement to the west. Faint black lines indicate identified hanging wall and footwall cutoffs. (C) The reconstructed Grande Ronde horizon is plotted with coloration indicating total rock uplift, and anticline symbology to indicate major anticline hinge zones. The maximum vertical change on this surface does not align with the maximum vertical displacement on the lower fault. The maximum vertical change in this unit more closely reflects the vertical displacement on the deeper fault.

Displacement and Strain

Faults accommodate a portion of the vertical displacement within the Saddle Mountains. Displacement on each of the major faults is visualized in Figure 4 and shown in the displacement profiles in Figure 5. The major, upper listric thrust (Figure 4A) has a maximum vertical displacement of ~890 m, which occurs within the Grande Ronde member and decreases upward into the Wanapum Basalts. Specific values for vertical displacement along this and the deeper major fault are available in the supplementary materials. Displacement along the upper major thrust fault peaks near the Columbia River where the strike of the anticline shifts northwestward. Just east of the Columbia River, this fault displays a minor peak in vertical displacement of ~690 m. Two peaks in vertical displacement, one aligning directly below the eastern displacement peak of the upper listric thrust, also characterize the major, deeper listric thrust (Figures 4B and 5). The distribution of displacement about this peak is more dispersed in the deeper fault than in the upper fault. The maximum vertical displacement on the major, deeper listric fault (~1360 m) is in the farthest westernmost study area, calculated from offset of seismic reflections possibly within the Swauk Formation near 6 km depth. Vertical displacement appears to taper upwards, where less offset between seismic reflections is observed and folding becomes more apparent (near 4.5 km depth).

Offset in the Grande Ronde and Wanapum members was used to calculate maximum vertical displacement along the two minor faults (displacement along these faults is shown in Figure 5 and specific values for displacement and slip for each unit are provided in the supplementary materials). The maximum vertical displacement observed along the western, minor thrust fault is ~385 m and is located along the eastern reaches of the fault, just west of the Columbia River. The maximum vertical displacement along the backthrust in the eastern segment of the Saddle Mountains is ~106 m and is localized in the western reaches of the fault. In general, we observe little displacement along the faults in the easternmost region of our study area (Figure 5).

Folding is primarily responsible for uplift in the eastern region of the Saddle Mountains (Table 1), and has produced large anticlines in the western region (Figure 5, e.g. S10). Orientations and structures within reconstructed flows were well constrained by field observations relative to older, deeper flows. Reconstructed surfaces reflect the shorter-wavelength folds associated with the upper, major thrust and the long-wavelength influence of the lower, major thrust (Figure 4B). Anticline axial traces nearly overlie the near-surface fault edge of the major, upper thrust fault, suggesting that the style of folding is fault-propagation folding or fault-bend folding lacking a developed upper flat

(Yan et al., 2016). In either case, the continued slip at the upper fault edge has been transferred into folds.

We calculate the total rock uplift to range from 35 m to 1821 m across the study area (Figure 5). Using assessments of vertical displacement on the major, upper thrust surface, we estimate that folding and long wavelength rotation on the deeper fault are responsible for ~1539 m, ~656 m, and ~1043 m of vertical displacement in the far western region of our field area, the region surrounding the Columbia River, and the far eastern region of our field area, respectively (Table 1). In the central region of our study area, vertical displacement along the upper fault and vertical displacement on the lower fault together exceed the total rock uplift. We can therefore calculate displacement on the lower fault that is not expressed on the folded, reconstructed surface (253 m, Table 1). If all vertical displacement is consumed by faulting, then no total rock uplift is to be accounted for by folding; however, we observe folds throughout our study area. Thus, this "missing" displacement represents a minimum displacement on the deeper fault that is not expressed at the surface. If the deeper fault does not affect vertical displacement of the reconstructed surface, then all rock uplift not accounted for by the upper fault is due to folding. If all of the vertical displacement on the deeper fault is expressed at the surface, and the total rock uplift exceeds the vertical displacement on both faults, then the remainder of vertical displacement is due to folding alone.

Unaccounted for displacement on the deeper fault, 253 m near cross section S5, implies that at least 253 m of vertical displacement on this fault may also not be expressed in the reconstructed surface at other locations in our study area. We can therefore estimate that ~250 m of total rock uplift in these other locations is due to folding, not faulting, and shows us that our estimates for contribution of folding to total rock uplift are likely minimums. When accounting for the 253 m adjustment, faulting produces 1186 m, 1546, and 244 m of total rock uplift and folding produces 635 m, 0 m, and 846 m of total rock uplift in the western, central, and eastern Saddle Mountains (Table 1).

Table 4.1 This table displays estimates for total rock uplift and vertical displacement taken directly from the Grande Ronde reconstructed surface of our model and the intersection of this surface with the upper and deeper major faults. We use these values to estimate the contributions of faulting and folding to total rock uplift.

	West (near S9)	Central (near S5)	East (near S2)
Total Rock Uplift (m)	1821	1546	1090
Upper Fault Vertical Displacement (m)	282	890	47
Deeper Fault Vertical Displacement (m)	1157	909	450
Maximum Vertical Displacement Expressed by Deeper Fault, and Maximum Rock Uplift from Folding Alone (m) *(Row 1 – Row 2)*	1539	656	1043
Minimum Rock Uplift from Folding Alone (m) *(Row 1 – Row 2 + Row 3)*	382	0*	593
Folding Contribution to Rock Uplift using "missing" 253 m Vertical Displacement from Deeper Fault in S5 *(Row 5 + 253 m)*	635	0	846
Fautling Contribution from both Upper and Lower Faults to Rock Uplift using "missing" 253 m Vertical Displacement from Deeper Fault in S5 *(Row 1 – Row 6)*	1186	1546	244
Folding and Faulting Contributions to Total Rock Uplift as % based on Estimates in Rows 6 and 7	35% / 65%	0% / 100%	78% / 22%

** Mathematically, the result was -253 m; however, this value cannot physically be negative, so it must be zero.*

The east–west component of displacement is relatively consistent along the ridge, less than 300 m along the anticline crests and southern slopes. Near the Columbia River where the anticline strike changes, east–west displacement estimates reach ~500 m.

Unfolding of the reconstructed flow surface was also used to calculate strain within the study area (Figure 5). We investigated strain oriented purely north–south (S_{yy}), normal strain oriented in the direction of maximum horizontal shortening (S_3), and the azimuth of S_3. We chose these parameters because Yakima folds are typically described as north-verging—implying a north–south oriented maximum principal stress propagated from the south. Contrasting values and distributions of S_{yy} and S_3 within the study area illuminate which segments of the ridge conform to the traditional stress characterization. By measuring the azimuth of S_3, we can visualize the orientation of maximum principal stresses responsible for strain and uplift.

North–south oriented strain (S_{yy}) is concentrated in the eastern region of the Saddle Mountains (Figure 5). West of the Columbia River, S_{yy} is greatest along the southern limbs of the folds, reaching 1.0% in most places. East of the Columbia River, S_{yy} is concentrated on the crests and southern limbs of the folds, but is greater in magnitude reaching, 8.0–13%. We also calculated shortening amount and percentage for each cross section. Values for shortening amount range from ~337 m in the east to ~1500 m in the west. Shortening percentages averaged ~5%, but again, increased from ~2.5% to 8% in the west.

In the eastern Saddle Mountains, S_{yy} and S_3 align; however, in the western Saddle Mountains, S_3 is oriented north–northeast. The majority of azimuths of S_3 range from 003° to 026°, with a mean and median of 022° and 014°. West of the Columbia River, azimuths primarily range from 020° to 030°. Like S_{yy}, S_3 is localized along the crests and southern limbs of the folds. In the west, values are between 1.0% and 8.0% in most places and in the east, values are between 1.0% and 13%. These strain values indicate the primary direction of shortening is north–south and north–northeast in the eastern and western study area, respectively.

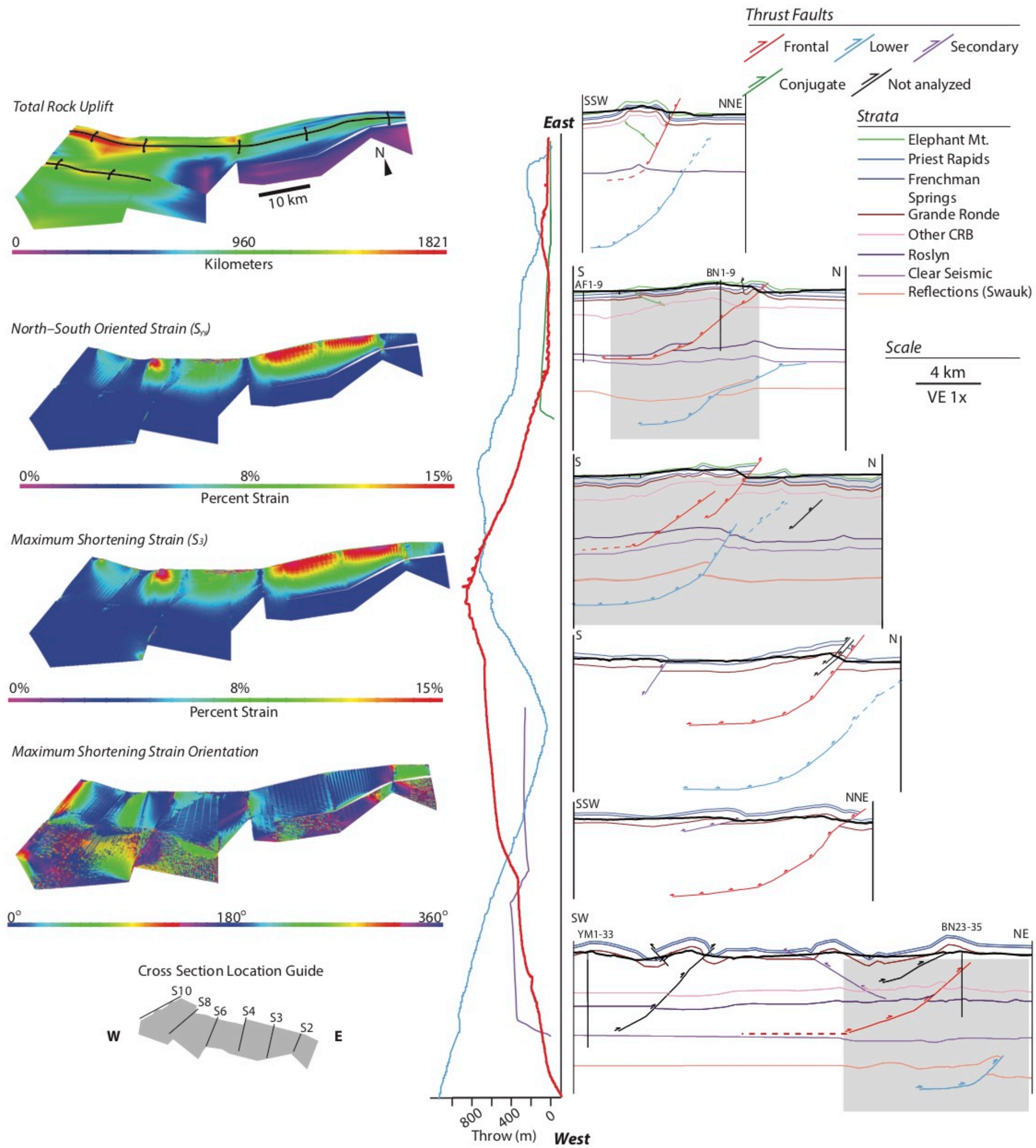

Figure 4.5 This figure shows six of our 10 line-balanced cross sections as well as the vertical displacement (throw) for each fault, total rock uplift considering folding and vertical displacement from faulting, north–south oriented strain (S_{yy}), maximum shortening strain (S_3), and orientation of maximum shortening strain visualized on the

unstrained or unfolded upper Grande Ronde flow surface. Cross sections are shown east (top) to west (bottom) and correspond to lines shown in the Cross Section Location Guide (lower left). Strata colors vary for each of the flows identified in well data, seismic data, or geologic data. Black vertical lines indicate wells with stratigraphic information and gray shading corresponds to available seismic profiles. There is no vertical exaggeration, and all cross sections utilize the same scale. In the central portion of the figure, we plot throw against the length of the study area from east (top) to west (bottom). Fault colors correspond to those in the cross sections. Peaks in displacement are visualized as maximums along these curves. At left, the unfolded surface of the upper Grande Ronde flow shows total rock uplift due to faulting and folding in the Saddle Mountains with anticline crests mapped. North–south oriented shortening is greatest in the eastern Saddle Mountains, and maximum shortening in the western Saddle Mountains is aligned north–northeast–south–southwest.

Discussion

Parallel Fault Surfaces

The fault surfaces visualized in our model reveal unexpected geometries and stress the importance of décollements on this developing tectonic landscape. We observed a fault in the western Saddle Mountains that changed vergence and dip (purple fault, Figures 5). In S10, this fault is steep and conjugate to the upper, main thrust. In S8–S9, it transitions to a south dipping thrust. The deep edge of this fault terminates near the top of the Roslyn formation which may have been utilized as a décollement horizon. Weak layers that encourage décollement formation may also promote faults which change vergence along strike (e.g. Higgins et al., 2007). The two major thrust faults may also root into décollements, as the seismic reflections indicate listric fault geometries and reflections in the hanging walls more distal from the faults appear sub-horizontal. The upper, major thrust is found to sole into the Roslyn Formation, as we did not observe offset seismic reflections associated with this fault below this formation. The fault may continue sub-horizontally within the Roslyn Formation or it may terminate within this stratum, but within our seismic window, we do not observe seismic reflections of the sub-horizontal strata above the lower folds to be offset by this fault. If this fault does plunge below the Roslyn Formation, it is not shown in our seismic data. Both faults are steeper than anticipated, and their parallel geometry is similar to one of the proposed geometries by Casale and Pratt (2015).

Many earthquakes within the YFP occur deeper than 5 km. Gomberg and others (2012) found that only one-third to one-half of earthquakes in the YFP were focused within the Columbia River Flood Basalts. They observe peaks in seismicity at 1–5 km depth and 5–10 km depth. The vast majority of these earthquakes appeared uncorrelated to fault traces, fold axes, or other mapped structures. Our results suggest that these earthquakes, particularly those focused below 5 km, may be related to deep structures such as the lower, major thrust fault, and the depths characterized by seismicity correlate with activity along identified décollements.

The parallel surfaces of the two major faults are startlingly similar, but differences in fault depth and displacement motivate questions of when and why tectonic activity occurred along the two faults. We interpret from seismic profiles that the deeper thrust fault and its associated folds are capped by relatively horizontal to mildly folded units.

Some smaller faults appear geometrically related to this deep fault, extending north of the upper fault edge, but these small faults are characterized by very little displacement of seismic reflections. The upper major thrust fault extends from the sub-horizontal strata upward toward the surface. That we do not observe the deeper thrust fault cutting through those sediments and do observe a strong geometric contrast between the pronounced anticlines associated with the lower thrust fault (after ~51 Ma, post-Swauk Formation) and the horizontal layers superposing those folds (possibly Roslyn Formation) implies a break in time between the development of folds above the lower fault and the initiation of the upper fault and Columbia River Basalt emplacement (~16 Ma). This is most apparent in S10 where exaggerated folds and large vertical displacements on the lower fault contrast with sub-horizontal strata (possibly belonging to the Swauk Formation) above. This pattern is not unique to the Saddle Mountains, and can be observed in the Frenchman Hills (F1 interpreted seismic section in the supplementary text). During the break in time between lessening of activity on the deeper major thrust and propagation of the upper major thrust (between ~52 Ma and ~16 Ma), a change in the deformational style of the deeper thrust may have occurred. Even as the upper, major thrust fault propagated to the surface, the lower fault may still have accommodated deformation. We interpret long-wavelength, upward folding mostly present in the western region of the study area to be caused by deformation along this deeper fault.

Contrasting displacement distributions on the fault surfaces imply differences in causes of deformation. The upper, major thrust has evolved as predicted by fault growth models (e.g. Cowie and Scholz, 1992). Maximum vertical displacement is located near the fault length midpoint and dissipates outward towards the fault tips (Figure 4A and

Figure 5, displacement profile). The orientation of S_3 and agreement of S_3 and S_{yy} strain values indicate that north–south oriented maximum horizontal compressive stresses were responsible for the uplift along this fault. The lower major thrust, however, shows greater displacement to the west, with a secondary peak in displacement just east of the Columbia River. The alignment of this peak with a local maximum in the displacement on the upper, major thrust indicates that the lower fault reactivated during the evolution of the upper, major thrust fault. Increased vertical displacement on the lower, major thrust fault and long-wavelength topographic development associated with that fault towards the west imply that this fault propagated in response to clockwise rotation of crustal deformation. An eastern Euler pole and clockwise block motion produced increased westward deformation.

Local History of Deformation

Our results show that the YFP has recorded a long and changing history of deformation in the Pacific Northwest. The distribution of displacement across the deeper, major thrust surface emphasizes the pattern of westward increasing strain and stresses. These stresses could have been caused by regional clockwise rotation of the North American crustal block. Strain was accommodated through anticlinal folds above the thrust fault after the deposition of the Swauk formation 59.9–49.9 Ma but before the deposition of the Roslyn Formation after 45.9 Ma (ages, Tabor et al., 1984; Cheney, 1994; Eddy et al., 2006). This estimate is consistent with the results of Eddy et al. (2006) which show that between 51.3 and 49.9 Ma west–northwest trending folding shortened the Swauk Formation. The Roslyn Formation caps the sub-horizontal cover strata lying unconformably above the folds, implying a pause in deformation after 49.9 Ma. Increased stresses reinitiated deformation before or during the emplacement of the Columbia River Basalts. The increased topography in the west observed today indicates that even as the Columbia River Basalts were emplaced, strain continued to accumulate, rotating and vertically displacing the basalts and sub-basalt units. The fault was too deep to produce short-wavelength topography, and this inefficiency spurred the development of an upper, major thrust at the top of the mildly deformed sequence.

The upper, major thrust fault accommodated mostly north–south oriented stresses after ~16 Ma. The deeper fault experienced some reactivation due to this north–south oriented shortening, but the pattern of displacement on this fault is fundamentally different from the upper, major fault. The differing patterns in faults of two contrasting ages imply that the tectonic context and thus stress orientation must have evolved over time. This change in stress orientation postdated emplacement of the Columbia River Basalts, as all of the basalt units are cut by or folded above the upper fault. Continued clockwise rotation in modern times may still be accommodated by the deeper fault, accounting for the deep earthquake foci discussed above.

We interpret that there must have been a time of north-northeast–south-southwest oriented shortening before ~50 Ma, followed by a pause in deformation. Deformation resumed sometime before the emplacement of the Columbia River Basalts at ~16 Ma. After this time, stresses reoriented north–south and rock uplift continued in a context of ongoing clockwise block rotation. We relate these events to our field observations and to regional-scale volcanic and tectonic context of the Eocene Pacific Northwest.

Connections to Regional Tectonics and Volcanism

Establishing a timeline for deformation and constraints on the direction and style of shortening has allowed us to hypothesize about tectonic influences on deformation. We connect the geologic histories of the Farallon and Juan de Fuca plates, the Chief Joseph Dike Swarm, Snake River Plain Hotspot Track, and the northern Basin and Range in a conceptual model to interpret the deformation preserved in the Yakima Folds and their structural predecessors (inset Figure 1). Each of these geologic phenomena have been connected to at least one of the others through extensive research, but because the YFP is so centrally located within the Pacific Northwest, we find that all components of this regional tectonic story are represented in its structures.

This history begins with the formation of the Siletz-Crescent terrane during the early Eocene. Paleomagnetic reconstructions and block motion models show that prior to 55 Ma, the Farallon and Kula plates were rapidly and obliquely subducting below the western North American craton (e.g. Wells et al., 1984; McCrory and Wilson, 2013). The boundary between these two plates was disturbed by a mantle plume. This rising plume triggered hotspot volcanism, producing thick, buoyant basalts with compositions reflective of the mantle source (Wells et al., 2014). As the Farallon plate continued to subduct, these basalts were accreted onto the western North American craton. The formation of the accreted terrane, now called the Siletz-Crescent terrane has been dated to 55–49 Ma (McCrory and Wilson, 2013).

Oblique, northeastward subduction of the Farallon plate, and its slab rollback, encouraged clockwise rotation of the accreted terranes (McCrory and Wilson, 2013). The rigid craton, however, resisted rotation (Wells and McCaffrey, 2013), and behaved as a rotational axis for the continued clockwise crustal motion. Clockwise rotation about this axis would have produced extension southwest of the Euler pole and west of the craton boundary, and it would have produced shortening west of the Euler pole and craton boundary. Regionally, terranes more distal from the axis would have experienced more intense deformation than terranes closer to the axis, similar to the swinging of a door about a hinge. Far from the "hinge", the northern Basin and Range display evidence of clockwise rotation during this time. Wells and Heller (1988) estimated 33% extension for the northern Basin and Range from 37 Ma to 50 Ma. These authors also estimate 39% extension since 37 Ma and 17% extension since 15 Ma, similar estimates to the 40–50% extension estimated by Colgan and Henry (2009). This implies a long history of opening and rotation in the region continuing after the accretion of the Siletz-Crescent terrane.

We propose that the westward increase in deformation observed in the lower, major thrust fault recorded this clockwise deformation. To expand our door analogy, as the door was opening in the Basin and Range, it was closing in central Washington. This closing would have been expressed through folding and thrust faulting of the sedimentary and volcanic sequences present in the region. Nearer to the door hinge, the expected deformation in the YFP region would have much less than that recorded in the Basin and Range, ~5–10% compared to the ~40% cited above.

Clockwise rotation slowed as slab rollback decelerated and the Farallon slab detached from the Juan de Fuca Plate. Block motion models show that detachment of the Farallon slab and resultant slowing subduction of the Juan de Fuca Plate occurred ~52 Ma (Caress et al., 1988), similar to when Eddy et al. (2006) estimate north-northeast–south-southwest oriented shortening (49.9 Ma). A pause in rapid rotation after 49.9 coincides with the period of interpreted tectonic quiescence in the Saddle Mountains. Reduced tectonic activity resulted in the deposition of observed sedimentary layers, such as the Roslyn Formation, atop the folds associated with the deeper major thrust.

During this pause, a slab window opened that allowed for the eastern migration of the plume that had formed the Siletz-Crescent terrane (e.g. Obrebski et al., 2010). By 19–17 Ma, the Juan de Fuca Plate had resumed oblique, northeastward subduction (Wilson, 1988; Wells and McCaffrey, 2013). The associated clockwise rotation due to rollback reinitiated. The combination of an active mantle plume and a passive crust-mantle environment encouraged volcanism in Northwestern Nevada. Camp (2013) describes that as the plume continued eastward, the plume head was decapitated along the North American craton. While the plume head migrated northward along the craton boundary, near the western boundaries of Oregon and Washington, it produced northward propagating dikes (Camp and Ross, 2004). At ~16 Ma, in the opening stress conditions near the rotational axis, the Chief Joseph Dike Swarm released the main phase of the Columbia River Basalts (Reidel et al., 2013). Smaller opening stresses near the rotational axis explain the lack of extensional tectonics associated with the swarm. The tail of the plume continued eastward forming the Snake River Plain Hotspot Track, which again reflected the deep mantle source (Graham et al., 2009). To the south, the lack of plume activity contributed to a volcanically quiet Basin and Range opening.

Strain associated with the Chief Joseph Dike Swarm are less than 1% (Camp, 2013; Morriss and Karlstrom, 2018), similar in order of magnitude to the strain displayed in the Saddle Mountains, a section of their compressional counterpart, the YFP. During this time, broad, long-wavelength topography developed primarily in the western front of the

Saddle Mountains along the deeper, major thrust. Coevally, a new fault—the upper, major thrust—began to propagate through the base of the Columbia River Basalts.

Tectonism waned after emplacement of the Grande Ronde flows, ~15 Ma, suggesting a reorientation of regional stresses. The transition to north–south oriented horizontal compressional stresses prompted the slowing of volcanism, rock uplift of the eastern Saddle Mountains, and development of shorter-wavelength folds across the entirety of the Saddle Mountains. Our cross sections show large displacements on the upper Saddle Mountains Basalts, and thus indicates that faulting must have been active after the emplacement of these members (~10 Ma, Reidel et al., 2013). Other studies also support that tectonic activity on the eastern segment of the mountains is recent, as modern as ~6 Ma (West et al., 1996; Staisch et al., 2018). During this time, the rate of convergence of the Juan de Fuca Plate with the North American Plate slowed, also reducing the speed of regional crustal clockwise rotation (McCaffrey and Wells, 2013). The north–south stresses may be indicative of toroidal flow above a torn, subducting Juan de Fuca Plate (Staisch et al., 2018 and references therein). This change in stresses and recent uplift is reflected in the displacement distribution of the upper major thrust and reactivation of the deeper major thrust.

Conclusions

We investigated the structural geometry and cause and timing of deformation for the Saddle Mountains, an anticline within the YFP. Fieldwork, seismic interpretation, and digital well and geologic data allowed us to construct a 3D model of the structures within the Saddle Mountains. This model proposes that two parallel listric thrust faults are responsible for the majority of topographic development along the ridge. The lower, major thrust fault and its associated folds recorded north–northeast–south–southwest oriented shortening prior to the emplacement of the Columbia River Basalts. Focused in the western Saddle Mountains, deformation along these structures continued after basalt emplacement, producing primarily long-wavelength topography. The upper, major thrust fault recorded more recent, north–south shortening that occurred after ~10 Ma. Folds that developed above this fault are responsible for short-wavelength topography. Parallel displacement across both faults in one region of our study area indicates that the lower fault may have been reactivated during more recent episodes of fault slip. All faults and folds record 2.5–13% strain.

Orientations and timing of this strain has allowed us to hypothesize how it may have accumulated. During the early Eocene, subduction, slab detachment, and plume activity generated a complex tectonic environment that spurred clockwise rotation of northwestern North America. This rotation was recorded in the Basin and Range and in structures beneath the present-day Yakima folds. Continued plume activity in the rotating crust generated the Columbia River Basalts, and more deformation within the folds. Reoriented stresses produced the younger north-verging folds we see today.

This work provides the basis for future research. Three-dimensional models with visualized displacement can be used to predict future seismic activity. They will also allow us to locate candidate field sites that are most likely to record kinematic indicators, such as deformed vesicles, facilitating future fieldwork. More work like this is necessary to address structural linkage between multiple folds within the YFP and to determine if parallel, listric faulting is a universal characteristic of the YFP. Our observation of deep structure and reactivation implies that there is certainly a connection between structures at multiple depths, and these structures may connect across Yakima folds. Understanding this linkage is critical for estimating seismic hazards (Last et al., 2012), as large connected fault zones pose increased hazard potential, and for contextualizing the YFP within the larger regional tectonic setting.

Acknowledgements

We thank Dr. Lydia Staisch and Dr. Harvey Kelsey for helpful review of the manuscript. Seismic Exchange, Inc. for the use of seismic profiles. Authors also acknowledge the use of the IPM and/or MOVE Software Suite granted by the Petroleum Experts Limited. We also thank the Bureau of Land Management, US Army Corps of Engineers, Department of Natural Resources, Department of Fish and Wildlife, US Bureau of Reclamation, and Mr. Gary Maughan for access to private property. Funding for research was provided by the University of Georgia Graduate School and Geology Department.

CHAPTER 5

CONCLUSIONS

Planetary interiors and exteriors are intimately connected. Formational processes like heating and cooling shape the geology we observe on the surface. In this dissertation, I focused on thrust-fault related landforms on Mercury and Earth, and analyzed those landforms to learn about how the planets evolved and were in turn, shaped by their evolutionary processes.

Investigations of Mercury

Mercury's surface contains preserved geology from billions of years ago. Faults and fault-related landforms on this planet primarily recorded global contraction, the effect of cooling on this body. This process was predicted to result in a global population of randomly oriented and distributed thrust fault-related landforms, but the rate at which this process occurred or when it begun were not geologically constrained. Tidal despinning and reorientation have also been proposed as effecting the population of structures. These processes are expected to have occurred on Mercury, with tidal despinning resulting in east–west oriented thrust faulting near the poles and north–south oriented thrust faulting near the equator when over printing on global contraction and reorientation leading to some global rotation of these landforms southward.

Chapters 2 and 3 addressed the timing and rate of global contraction and the effect of these other processes. Results of chapter 2 show that global contraction on Mercury began and operated at its most rapid rate during the Calorian, after which the process slowed gradually toward present day. An analysis of tectonic map patterns of thrust fault-related landforms in the Northern Smooth Plains of Mercury in chapter 3 showed that faults in this region root to a shallow décollement and are preferentially oriented north–south in the mid-latitudes and east–west near the poles. Centered about the north pole, this bulls eye pattern indicates that despinning must have overprinted on the effects of global contraction and that if reorientation did occur, it must have pre-dated despinning.

Investigation of Earth

We can often use one planet to learn about another. Earth analogues, like the anticlines of the Yakima Fold Province can teach us about how basalts deform and how large-scale processes like plate rotation can be expressed on a smaller scale. Planetary tectonism gives us the opportunity to learn about deformation without the impact of erosion and to see what early planetary surfaces, and perhaps an early Earth may have looked. In Chapter 4, my objective was to describe the deformation in the basalts of the YFP through a three-dimensional fault and fold model and then relate that model to the tectonic setting of the Cenozoic Pacific Northwest.

I developed this model using structural orientation measurements collected during field study, seismic profile interpretations, well logs, and geologic maps. I determined that two major faults produced the observed topography of one ridge in the YFP. Stratigraphic differences between these faults allowed me to establish a relative timeline of faulting and folding in the Yakima Fold Province region. A deep listric thrust fault cutting pre-Columbia River Flood Basalt sedimentary sequences represented ancient deformation associated with the clockwise rotation of the North American plate relative to the subducting Farallon plate. As the Farallon detached and the Juan de Fuca Plate stalled, deposition of sedimentary strata was able to take place in the YFTB. We observe these strata as horizontal unfolded layers above the deeper fault. During this gap in subduction, a plume was able to migrate eastward.

Eventually, the Juan de Fuca Plate began oblique subduction and rotation re-initiated. As the plume approached the North American craton boundary, the head detached from the tail. The tail of the plume migrated to the west, producing the snake river plane hotspot track, but the head migrated northward. This head entered a region where the crust was opening, and resulted in the release of the Columbia River Flood Basalts. An upper fault cut and deformed Columbia River Flood Basalts and reflects a more recent period of deformation. As the Juan de Fuca Plate tore, stresses were redirected northward, causing a varying pattern of deformation on the upper fault relative to the deeper fault.

Future Work

The research presented in this dissertation reflects how analyses may be used to link the interior and formational processes of a planet with its surface geology. By continuing to study surface structures, we will learn more about planetary evolution and how that evolution is expressed through tectonism. In particular, this dissertation emphasizes the importance of understanding deformational processes in basalts.

Basalt is the most common rock in the crust of our planet and has been observed on the surface of other solar system bodies like the Moon, Mercury, and Mars. Basaltic rocks make up the Earth's sub-sediment ocean floor, and are produced at divergent plate boundaries and destroyed at convergent boundary subduction zones. I believe the connection between basalts and plate boundaries is under-explored. For example, an important open question in geology is how subduction zones initiate (Stern, 2004; 2018).

Our current understanding is that subduction zones may form when oceanic crust ages, thickens, and cools. It becomes denser than the underlying asthenosphere and sinks along passive margins or pre-existing plate boundaries and fractures (Dickinson and Seely, 1979; Cloetingh et al., 1989; Turcotte and Schubert, 2014). The sinking lithosphere drags its younger, neighboring lithosphere toward the subduction zone and away from the spreading center, and this force, called *slab pull*, is thus the most important plate-tectonic process on Earth (Turcotte and Schubert, 2014). This force drives mantle convection (Hager and O'Connell, 1981).

When viewing all of plate tectonics as an effect of slab pull, it becomes clear that maximum, horizontal compressive stresses exceeding the strength of rock is not necessary for subduction zone initiation (Stern, 2004). Maximum vertical stresses like those that may be driven by gravitational instability of a dense plate may push a plate down, and thus subduction may initiate in extensional settings where pre-existing weaknesses are already orientated parallel to the plate boundary (Kemp and Stevenson, 1996). These pre-existing weaknesses and the water that can flow into weak spaces in the rock affect the ability of the rock to subduct (Ranero et al., 2003; Fujie et al., 2013; Shillington et al., 2015). Therefore, understanding the propagation of faults within basalts, and characterizing how the strength of the basalt is affected by fracturing, hydration, and serpentinization (mineralization due to hydration) is important.

The fracturing pattern inherent to basalt sequences may play a role in developing this understanding. For example, we observed columnar jointing, hackly jointing, and entablature in the Columbia River Basalts. These fractures initially formed vertically, but rotated during the folding of the basalts. Could this reorientation of fractures promote subduction zones or other plate boundary processes? Is this fracture network functioning like an accordion stretching down into subduction zones and promoting their formation? Is the lack of these fracture networks in transitionary crust why subduction zones struggle to form at passive margins?

Vertically fractured basalts were only a part of a horizontal sequence of basalt fabrics we observed. We also observed laterally continuous bands of vesicles and pillow basalts. What role, if any, could this layering play in how faults develop in basalt sequences? Vesicles must be more unstable relative to their solid, less porous counterparts. Does this mean that horizontal fault motion is primarily recorded in vesicle layers? Are these layers then not just texturally different, but mechanically different and susceptible to varying chemical weathering? These questions ultimately make one wonder if Earth's plate boundaries form as a consequence of the basalts they are able to generate and destroy. Basalts are not just the product of the plate boundary-- they are why the boundary lives.

That life is expressed through continued fracturing and reactivation. Chapter 4 work produced a model for fault networks in the Yakima Fold Province, and the pattern of displacement on the faults implied that faults were active together, responding to the same stress field but that stresses were more dispersed on the lower fault. Is this pattern a signature of reactivation? If so, what stress parameters determine where seismicity is expressed (i.e. which fault bears the burden of the next earthquake event?). When fault properties, like geometry and host rock type contrast in these environments, what can we learn about seismic and aseismic slip along these faults? Vertical fault linkage through differing rock types presents a unique opportunity to study the effect of rheological parameters on the expression of seismicity and reactivation, while controlling for location and thus, stress environment. It also allows us the opportunity to consider how stresses are partitioned vertically in the upper crust, and challenge our assumptions about how and when deep crustal stresses may be transferred and expressed into the upper crust. Answering these questions may not just allow us to study how subduction zones form, but how divergent boundaries are formed as well.

REFERENCES

Alder, S., Smith, S., & Scott, J. (2016). Fault-zone structure and weakening processes in basin-scale reverse faults: The Moonlight Fault Zone, South Island, New Zealand. *Journal of Structural Geology, 91*, 177-194.

Allemand, P., & Thomas, P. (1995). Localization of Martian ridges by impact craters: Mechanical and chronological implications. *Journal of Geophysical Research: Planets, 100*(E2), 3251-3262.

Anderson, E. M. (1951). *The dynamics of faulting and dyke formation with applications to Britain*: Hafner Pub. Co.

Aubele, J. C., Crumpler, L., & Elston, W. E. (1988). Vesicle zonation and vertical structure of basalt flows. *Journal of Volcanology and Geothermal Research, 35*(4), 349-374.

Banks, M., Xiao, Z., Braden, S., Marchi, S., Chapman, C., Barlow, N., & Fassett, C. (2016). *Revised age constraints for Mercury's Kuiperian and Mansurian systems.* Paper presented at the Lunar and Planetary Science Conference.

Banks, M. E., Watters, T. R., Robinson, M. S., Tornabene, L. L., Tran, T., Ojha, L., & Williams, N. R. (2012). Morphometric analysis of small-scale lobate scarps on the Moon using data from the Lunar Reconnaissance Orbiter. *Journal of Geophysical Research: Planets, 117*(E12). doi:10.1029/2011JE003907

Banks, M. E., Barlow, N., Klimczak, C., Xiao, Z., Watters, T. R., & Chapman, C.R. (2015a), Duration of Activity on Lobate-Scarp Thrust Faults on Mercury, *Planet. Crater Consort., 6*, abstract 1513.

Banks, M. E., Xiao, Z. Y., Watters, T. R., Strom, R. G., Braden, S. E., Chapman, C. R., . . . Byrne, P. K. (2015b). Duration of activity on lobate-scarp thrust faults on Mercury. *Journal of Geophysical Research-Planets, 120*(11), 1751-1762. doi:10.1002/2015JE004828

Baraff, D., & Witkin, A. (1998). *Large steps in cloth simulation.* Paper presented at the Proceedings of the 25th annual conference on Computer graphics and interactive techniques.

Barnouin, O. S., Zuber, M. T., Smith, D. E., Neumann, G. A., Herrick, R. R., Chappelow, J. E., . . . Prockter, L. M. (2012). The morphology of craters on Mercury: Results from MESSENGER flybys. *Icarus, 219*(1), 414-427.

Bauville, A., & Schmalholz, S. M. (2015). Transition from thin-to thick-skinned tectonics and consequences for nappe formation: numerical simulations and applications to the Helvetic nappe system, Switzerland. *Tectonophysics, 665*, 101-117.

Becker, K., Robinson, M., Becker, T., Weller, L., Edmundson, K., Neumann, G., . . . Solomon, S. (2016). *First global digital elevation model of Mercury.* Paper presented at the Lunar and Planetary Science Conference.

Beuthe, M. (2010). East–west faults due to planetary contraction. *Icarus, 209*(2), 795-817.

Bigi, S., Conti, A., Casero, P., Ruggiero, L., Recanati, R., & Lipparini, L. (2013). Geological model of the central Periadriatic basin (Apennines, Italy). *Marine and Petroleum Geology, 42*, 107-121.

Bilotti, F., & Suppe, J. (1999). The global distribution of wrinkle ridges on Venus. *Icarus, 139*(1), 137-157.

Binder, A. B., & Gunga, H.-C. (1985). Young thrust-fault scarps in the highlands: Evidence for an initially totally molten Moon. *Icarus, 63*(3), 421-441.

Bjornstad, B. N., Babcock, R. S., & Last, G. V. (2007). Flood basalts and Ice Age floods: Repeated late Cenozoic cataclysms of southeastern Washington. *Floods, Faults, and Fire: Geological Field Trips in Washington State and Southwest British Columbia, 9*, 209.

Blakely, R. J., Sherrod, B. L., Weaver, C. S., Wells, R. E., & Rohay, A. C. (2014). The Wallula fault and tectonic framework of south-central Washington, as interpreted from magnetic and gravity anomalies. *Tectonophysics, 624*, 32-45.

Blakely, R. J., Sherrod, B. L., Weaver, C. S., Wells, R. E., Rohay, A. C., Barnett, E. A., & Knepprath, N. E. (2011). Connecting the Yakima fold and thrust belt to active faults in the Puget Lowland, Washington. *Journal of Geophysical Research: Solid Earth, 116*(B7).

Bonatti, E. (1965). Palagonite, hyaloclastites and alteration of volcanic glass in the ocean. *Bulletin Volcanologique, 28*(1), 257-269.

Boyer, S. E., & Elliott, D. (1982). Thrust systems. *AAPG Bulletin*, *66*(9), 1196-1230.

Braden, S. E., & Robinson, M. S. (2013). Relative rates of optical maturation of regolith on Mercury and the Moon. *Journal of Geophysical Research: Planets, 118*(9), 1903-1914.

Brandes, C., & Tanner, D. C. (2014). Fault-related folding: A review of kinematic models and their application. *Earth-Science Reviews*, *138*, 352-370.

Brocher, T. M., Wells, R. E., Lamb, A. P., & Weaver, C. S. (2017). Evidence for distributed clockwise rotation of the crust in the northwestern United States from fault geometries and focal mechanisms. *Tectonics, 36*(5), 787-818.

Brun, J. P., & Nalpas, T. (1996). Graben inversion in nature and experiments. *Tectonics, 15*(3), 677-687.

Buczkowski, D., Schmidt, B., Williams, D., Mest, S., Scully, J., Ermakov, A., . . . Hiesinger, H. (2016). The geomorphology of Ceres. *Science, 353*(6303), aaf4332.

Butler, R. W. (1982). The terminology of structures in thrust belts. *Journal of Structural Geology*, *4*(3), 239-245.

Byrne, P. D., Klimczak, C., & Sengor, A. M. C. (2018). The tectonic character of Mercury. In S. C. Solomon, L. R. Nittler, & B. J. Anderson (Eds.), *Mercury: The View after MESSENGER* (pp. 249–286). Cambridge, United Kingdom: Cambridge University Press.

Byrne, P. K., Klimczak, C., McGovern, P. J., Mazarico, E., James, P. B., Neumann, G. A., . . . Solomon, S. C. (2015). Deep-seated thrust faults bound the Mare Crisium lunar mascon. *Earth and Planetary Science Letters, 427*, 183-190.

Byrne, P. K., Klimczak, C., Sengor, A. M. C., Solomon, S. C., Watters, T. R., & Hauck, S. A. (2014). Mercury's global contraction much greater than earlier estimates. *Nature Geoscience, 7*(4), 301-307.

Camp, V. E. (2013). Origin of Columbia River Basalt: Passive rise of shallow mantle, or active upwelling of a deep-mantle plume. *The Columbia River Flood Basalt Province: Geological Society of America Special Paper, 497*, 181-199.

Camp, V. E., & Ross, M. E. (2004). Mantle dynamics and genesis of mafic magmatism in the intermontane Pacific Northwest. *Journal of Geophysical Research: Solid Earth, 109*(B8).

Campbell, N. P. (1989). Structural and stratigraphic interpretation of. *Volcanism and Tectonism in the Columbia River Flood-Basalt Province, 239*, 209.

Cardozo, N., & Brandenburg, J. (2014a). Kinematic modeling of folding above listric propagating thrusts. *Journal of Structural Geology, 60*, 1-12.

Cardozo, N., & Brandenburg, J. (2014b). Kinematic modeling of folding above listric propagating thrusts. *Journal of Structural Geology, 60*, 1-12.

Caress, D. W., Menard, H., & Hey, R. (1988). Eocene reorganization of the Pacific-Farallon spreading center north of the Mendocino Fracture Zone. *Journal of Geophysical Research: Solid Earth, 93*(B4), 2813-2838.

Casale, G., & Pratt, T. L. (2015). Thin-or thick-skinned faulting in the Yakima fold and thrust belt (WA)? Constraints from kinematic modeling of the Saddle Mountains anticline. *Bulletin of the Seismological Society of America, 105*(2A), 745-752.

Chapple, W. M. (1978). Mechanics of thin-skinned fold-and-thrust belts. *Geological Society of America Bulletin, 89*(8), 1189-1198.

Cheney, E. S., & Lasmanis, R. (1994). Cenozoic unconformity-bounded sequences of central and eastern Washington. *Washington Division of Geology and Earth Resources Bulletin, 80*, 115-139.

Chicarro, A. F., Schultz, P. H., & Masson, P. (1985). Global and regional ridge patterns on Mars. *Icarus, 63*(1), 153-174.

Cloetingh, S., Wortel, R., & Vlaar, N. J. (1989). On the initiation of subduction zones. In *Subduction Zones Part II* (pp. 7-25). Birkhäuser Basel.

Colgan, J. P., & Henry, C. D. (2009). Rapid middle Miocene collapse of the Mesozoic orogenic plateau in north-central Nevada. *International Geology Review, 51*(9-11), 920-961.

Cordell, B. M., & Strom, R. G. (1977). Global tectonics of Mercury and the Moon. *Physics of the Earth and Planetary Interiors, 15*(2-3), 146-155.

Costa, E., & Vendeville, B. (2002). Experimental insights on the geometry and kinematics of fold-and-thrust belts above weak, viscous evaporitic décollement. *Journal of Structural Geology, 24*(11), 1729-1739.

Couzens-Schultz, B. A., Vendeville, B. C., & Wiltschko, D. V. (2003). Duplex style and triangle zone formation: insights from physical modeling. *Journal of Structural Geology, 25*(10), 1623-1644.

Coward, M. (1983). Thrust tectonics, thin skinned or thick skinned, and the continuation of thrusts to deep in the crust. *Journal of Structural Geology, 5*(2), 113-123.

Cowie, P. A., & Scholz, C. H. (1992a). Displacement-length scaling relationship for faults: data synthesis and discussion. *Journal of Structural Geology, 14*(10), 1149-1156.

Cowie, P. A., & Scholz, C. H. (1992b). Growth of faults by accumulation of seismic slip. *Journal of Geophysical Research: Solid Earth, 97*(B7), 11085-11095.

Cowie, P. A., & Scholz, C. H. (1992c). Physical explanation for the displacement-length relationship of faults using a post-yield fracture mechanics model. *Journal of Structural Geology, 14*(10), 1133-1148.

Crane, K. T., & Klimczak, C. (2017). Timing and rate of global contraction on Mercury. *Geophysical Research Letters, 44*(7), 3082-3089.

Crane, K. T., & Klimczak, C. (2019). Tectonic patterns of shortening landforms in Mercury's northern smooth plains. *Icarus, 317*, 66-80.

Crumpler, L., Head, J. W., & Campbell, D. B. (1986). Orogenic belts on Venus. *Geology, 14*(12), 1031-1034.

Dahlen, F., Suppe, J., & Davis, D. (1984). Mechanics of fold-and-thrust belts and accretionary wedges: Cohesive Coulomb theory. *Journal of Geophysical Research: Solid Earth, 89*(B12), 10087-10101.

Dahlstrom, C. D. (1970). Structural geology in the eastern margin of the Canadian Rocky Mountains. *Bulletin of Canadian Petroleum Geology, 18*(3), 332-406.

Davis, D. M., & Engelder, T. (1985). The role of salt in fold-and-thrust belts. *Tectonophysics, 119*(1-4), 67-88.

De Paola, N., Mirabella, F., Barchi, M., & Burchielli, F. (2006). Early orogenic normal faults and their reactivation during thrust belt evolution: the Gubbio Fault case study, Umbria-Marche Apennines (Italy). *Journal of Structural Geology, 28*(11), 1948-1957.

Denevi, B. W., Ernst, C. M., Meyer, H. M., Robinson, M. S., Murchie, S. L., Whitten, J. L., . . . Ostrach, L. R. (2013). The distribution and origin of smooth plains on Mercury. *Journal of Geophysical Research: Planets, 118*(5), 891-907.

Di Achille, G., Popa, C., Massironi, M., Ferrari, S., Mazzotta Epifani, E., Zusi, M., . . . Palumbo, P. (2012). *Mercury's radius change estimates revisited using high* *incidence angle MESSENGER data.* Paper presented at the EGU General Assembly Conference Abstracts.

Dickinson, W. R., & Seely, D. R. (1979). Structure and stratigraphy of forearc regions. *AAPG Bulletin*, *63*(1), 2-31.

Dickson, J. L., Head, J. W., Whitten, J. L., Fassett, C. I., Neumann, G. A., Smith, D. E., . . . Phillips, R. J. (2012). Topographic rise in the northern smooth plains of Mercury: characteristics from MESSENGER image and altimetry data and candidate modes of origin.

Dombard, A. J., & Hauck II, S. A. (2008). Despinning plus global contraction and the orientation of lobate scarps on Mercury: Predictions for MESSENGER. *Icarus, 198*(1), 274-276.

Dzurisin, D. (1978). The tectonic and volcanic history of Mercury as inferred from studies of scarps, ridges, troughs, and other lineaments. *Journal of Geophysical Research: Solid Earth, 83*(B10), 4883-4906.

Eddy, M. P., Bowring, S. A., Umhoefer, P. J., Miller, R. B., McLean, N. M., & Donaghy, E. E. (2016). High-resolution temporal and stratigraphic record of Siletzia's accretion and triple junction migration from nonmarine sedimentary basins in central and western Washington. *Bulletin, 128*(3-4), 425-441.

Egea-Gonzalez, I., Ruiz, J., Fernandez, C., Williams, J. P., Marquez, A., & Lara, L. M. (2012). Depth of faulting and ancient heat flows in the Kuiper region of Mercury from lobate scarp topography. *Planetary and Space Science, 60*(1), 193-198.

Fassett, C. I., Head, J. W., Baker, D. M., Zuber, M. T., Smith, D. E., Neumann, G. A., . . . Chapman, C. R. (2012). Large impact basins on Mercury: Global distribution, characteristics, and modification history from MESSENGER orbital data. *Journal of Geophysical Research: Planets, 117*(E12).

Fassett, C. I., Head, J. W., Blewett, D. T., Chapman, C. R., Dickson, J. L., Murchie, S. L., . . . Watters, T. R. (2009). Caloris impact basin: Exterior geomorphology, stratigraphy, morphometry, radial sculpture, and smooth plains deposits. *Earth and Planetary Science Letters, 285*(3-4), 297-308.

Ferrari, S., Massironi, M., Marchi, S., Byrne, P. K., Klimczak, C., Martellato, E., & Cremonese, G. (2015). Age relationships of the Rembrandt basin and Enterprise Rupes, Mercury. *Geological Society, London, Special Publications, 401*(1), 159-172.

Fossen, H. (2016). *Structural Geology* (2 ed.). Cambridge: Cambridge University Press.

Freed, A. M., Blair, D. M., Watters, T. R., Klimczak, C., Byrne, P. K., Solomon, S. C., . . . Melosh, H. (2012). On the origin of graben and ridges within and near volcanically buried craters and basins in Mercury's northern plains. *Journal of Geophysical Research: Planets, 117*(E12).

Fujie, G., Miura, S., Kodaira, S., Kaneda, Y., Shinohara, M., Mochizuki, K., ... & Uehira, K. (2013). Along-trench structural variation and seismic coupling in the northern Japan subduction zone. *Earth, Planets and Space*, *65*(2), 75-83.

Giacomini, L., Massironi, M., Marchi, S., Fassett, C., Di Achille, G., & Cremonese, G. (2015). Age dating of an extensive thrust system on Mercury: implications for the planet's thermal evolution. *Geological Society, London, Special Publications, 401*(1), 291-311.

Golombek, M., Anderson, F., & Zuber, M. (2001). Martian wrinkle ridge topography: Evidence for subsurface faults from MOLA. *Journal of Geophysical Research: Planets, 106*(E10), 23811-23821.

Golombek, M., Plescia, J., & Franklin, B. (1991). *Faulting and folding in the formation of planetary wrinkle ridges.* Paper presented at the Lunar and Planetary Science Conference Proceedings.

Gomberg, J., Sherrod, B., Trautman, M., Burns, E., & Snyder, D. (2012). Contemporary seismicity in and around the Yakima Fold-and-Thrust belt in eastern Washington. *Bulletin of the Seismological Society of America, 102*(1), 309-320.

Graham, D., Reid, M., Jordan, B., Grunder, A., Leeman, W., & Lupton, J. (2009). Mantle source provinces beneath the northwestern USA delimited by helium isotopes in young basalts. *Journal of Volcanology and Geothermal Research, 188*(1-3), 128-140.

Greenhalgh, S. R., McBride, J. H., Bartley, J. M., Keach, R. W., Britt, B. B., & Kowallis, B. J. (2015). Along-strike variability of thrust fault vergence. *Interpretation, 3*(3), SX1-SX12.

Grott, M., Breuer, D., & Laneuville, M. (2011). Thermo-chemical evolution and global contraction of Mercury. *Earth and Planetary Science Letters, 307*(1-2), 135-146.

Grott, M., Hauber, E., Werner, S., Kronberg, P., & Neukum, G. (2007). Mechanical modeling of thrust faults in the Thaumasia region, Mars, and implications for the Noachian heat flux. *Icarus, 186*(2), 517-526.

Hager, B. H., & O'Connell, R. J. (1981). A simple global model of plate dynamics and mantle convection. *Journal of Geophysical Research: Solid Earth*, *86*(B6), 4843-4867.

Hauck II, S. A., Dombard, A. J., Phillips, R. J., & Solomon, S. C. (2004). Internal and tectonic evolution of Mercury. *Earth and Planetary Science Letters, 222*(3-4), 713-728.

Head, J. W., Chapman, C. R., Strom, R. G., Fassett, C. I., Denevi, B. W., Blewett, D. T., . . . Murchie, S. L. (2011). Flood volcanism in the northern high latitudes of Mercury revealed by MESSENGER. *Science, 333*(6051), 1853-1856.

Higgins, S., Davies, R. J., & Clarke, B. (2007). Antithetic fault linkages in a deep water fold and thrust belt. *Journal of Structural Geology, 29*(12), 1900-1914.

Jadoon, I. A., Lawrence, R. D., & Hassan, K. S. (1994). Mari-Bugti pop-up zone in the central Sulaiman fold belt, Pakistan. *Journal of Structural Geology, 16*(2), 147-158.

Jaeger, J. C., Cook, N. G., & Zimmerman, R. (2009). *Fundamentals of rock mechanics*: John Wiley & Sons.

John, S., & Medwedeff, D. A. (1990). Geometry and kinematics of fault-propagation folding. *Eclogae Geol. Helv, 83*(3), 409-454.

Kattenhorn, S. A., & Prockter, L. M. (2014). Evidence for subduction in the ice shell of Europa. *Nature Geoscience, 7*(10), 762.

Kelly, P., Peacock, D., Sanderson, D., & McGurk, A. (1999). Selective reverse-reactivation of normal faults, and deformation around reverse-reactivated faults in the Mesozoic of the Somerset coast. *Journal of Structural Geology, 21*(5), 493-509.

Kelsey, H. M., Ladinsky, T. C., Staisch, L., Sherrod, B. L., Blakely, R. J., Pratt, T. L., . . . Wan, E. (2017). The story of a Yakima fold and how it informs Late Neogene and Quaternary backarc deformation in the Cascadia subduction zone, Manastash anticline, Washington, USA. *Tectonics, 36*(10), 2085-2107.

Kemp, D. V., & Stevenson, D. J. (1996). A tensile, flexural model for the initiation of subduction. *Geophysical Journal International*, *125*(1), 73-93.

Kinczyk, M. J., Prockter, L. M., Chapman, C. R., & Susorney, H. C. (2016). A morphological evaluation of crater degradation on Mercury: Revisiting crater classification with MESSENGER data. *Lunar Planet. Sci, 47*.

King, P. B. (1960). The anatomy and habitat of low-angle thrust faults: Am. *Jour. Sci, 258*, 115-125.

Klimczak, C. (2015). Limits on the brittle strength of planetary lithospheres undergoing global contraction. *Journal of Geophysical Research: Planets, 120*(12), 2135-2151.

Klimczak, C., Byrne, P. K., & Solomon, S. C. (2015). A rock-mechanical assessment of Mercury's global tectonic fabric. *Earth and Planetary Science Letters, 416*, 82-90.

Klimczak, C., Kling, C. L., & Byrne, P. K. (2018). Topographic Expressions of Large Thrust Faults on Mars. *Journal of Geophysical Research: Planets, 123*(8), 1973-1995.

Klimczak, C., Watters, T. R., Ernst, C. M., Freed, A. M., Byrne, P. K., Solomon, S. C., . . . Head, J. W. (2012). Deformation associated with ghost craters and basins in volcanic smooth plains on Mercury: Strain analysis and implications for plains evolution. *Journal of Geophysical Research: Planets, 117*(E12).

Knibbe, J. S., & van Westrenen, W. (2017). On Mercury's past rotation, in light of its large craters. *Icarus, 281*, 1-18.

Lacombe, O., Mouthereau, F., Angelier, J., Chu, H. T., & Lee, J. C. (2003). Frontal belt curvature and oblique ramp development at an obliquely collided irregular margin: Geometry and kinematics of the NW Taiwan fold-thrust belt. *Tectonics, 22*(3).

Linnros, H., Hansman, R., & Ring, U. (2019). The 3D geometry of the Naxos detachment fault and the three-dimensional tectonic architecture of the Naxos metamorphic core complex, Aegean Sea, Greece. *International Journal of Earth Sciences, 108*(1), 287-300.

Long, P. E., & Wood, B. J. (1986). Structures, textures, and cooling histories of Columbia River basalt flows. *Geological Society of America Bulletin, 97*(9), 1144-1155.

Long, S., McQuarrie, N., Tobgay, T., & Grujic, D. (2011). Geometry and crustal shortening of the Himalayan fold-thrust belt, eastern and central Bhutan. *Bulletin, 123*(7-8), 1427-1447.

Madritsch, H., Schmid, S. M., & Fabbri, O. (2008). Interactions between thin-and thick-skinned tectonics at the northwestern front of the Jura fold-and-thrust belt (eastern France). *Tectonics, 27*(5).

Mangold, N., Allemand, P., & Thomas, P. (1998). Wrinkle ridges of Mars: Structural analysis and evidence for shallow deformation controlled by ice-rich décollements. *Planetary and Space Science, 46*(4), 345-356.

Mann, P. (2007). Global catalogue, classification and tectonic origins of restraining-and releasing bends on active and ancient strike-slip fault systems. *Geological Society, London, Special Publications, 290*(1), 13-142.

Marchi, S., Chapman, C. R., Fassett, C. I., Head, J. W., Bottke, W., & Strom, R. G. (2013). Global resurfacing of Mercury 4.0–4.1 billion years ago by heavy bombardment and volcanism. *Nature, 499*(7456), 59.

Massironi, M., Di Achille, G., Rothery, D., Galluzzi, V., Giacomini, L., Ferrari, S., . . . Palumbo, P. (2015). Lateral ramps and strike-slip kinematics on Mercury. *Geological Society, London, Special Publications, 401*(1), 269-290.

Matsuyama, I., & Nimmo, F. (2009). Gravity and tectonic patterns of Mercury: Effect of tidal deformation, spin-orbit resonance, nonzero eccentricity, despinning, and reorientation. *Journal of Geophysical Research: Planets, 114*(E1).

Mazarico, E., Genova, A., Goossens, S., Lemoine, F. G., Neumann, G. A., Zuber, M. T., . . . Solomon, S. C. (2014). The gravity field, orientation, and ephemeris of Mercury from MESSENGER observations after three years in orbit. *Journal of Geophysical Research: Planets, 119*(12), 2417-2436.

McCaffrey, R., King, R. W., Payne, S. J., & Lancaster, M. (2013a). Active tectonics of northwestern US inferred from GPS-derived surface velocities. *Journal of Geophysical Research: Solid Earth, 118*(2), 709-723.

McCaffrey, R., King, R. W., Payne, S. J., & Lancaster, M. (2013b). Active tectonics of northwestern US inferred from GPS-derived surface velocities. *Journal of Geophysical Research: Solid Earth, 118*(2), 709-723.

McCaffrey, R., King, R. W., Wells, R. E., Lancaster, M., & Miller, M. M. (2016). Contemporary deformation in the Yakima fold and thrust belt estimated with GPS. *Geophysical Journal International, 207*(1), 1-11.

Mccauley, J. F., Guest, J. E., Schaber, G. G., Trask, N. J., & Greeley, R. (1981). Stratigraphy of the Caloris basin, Mercury. *Icarus, 47*(2), 184-202.

McClay, K., & Bonora, M. (2001). Analog models of restraining stepovers in strike-slip fault systems. *AAPG bulletin, 85*(2), 233-260.

McClay, K. R. (1992). Glossary of thrust tectonics terms. *Thrust tectonics*, 419-433.

McCrory, P. A., & Wilson, D. S. (2013). A kinematic model for the formation of the Siletz-Crescent forearc terrane by capture of coherent fragments of the Farallon and Resurrection plates. *Tectonics, 32*(3), 718-736.

Mège, D., & Reidel, S. P. (2001). A method for estimating 2D wrinkle ridge strain from application of fault displacement scaling to the Yakima folds, Washington. *Geophysical Research Letters*, *28*(18), 3545-3548.

Melosh, H., & Dzurisin, D. (1978). Mercurian global tectonics: A consequence of tidal despinning? *Icarus, 35*(2), 227-236.

Melosh, H., & McKinnon, W. (1988). The tectonics of Mercury. *Mercury, University of Arizona Press*, 374-400.

Melosh, H. J. (1989). *Impact cratering: a geologic process*. New York
Oxford: Oxford University Press; Clarendon Press.

Melosh, H. J. (1977). Global tectonics of a despun planet. *Icarus, 31*(2), 221-243.

Mitra, S., & Paul, D. (2011). Structural geometry and evolution of releasing and restraining bends: Insights from laser-scanned experimental models. *AAPG bulletin, 95*(7), 1147-1180.

Montési, L. G., & Zuber, M. T. (2003). Spacing of faults at the scale of the lithosphere and localization instability: 1. Theory. *Journal of Geophysical Research: Solid Earth, 108*(B2).

Morbidelli, A., Marchi, S., Bottke, W. F., & Kring, D. A. (2012). A sawtooth-like timeline for the first billion years of lunar bombardment. *Earth and Planetary Science Letters, 355*, 144-151.

Morriss, M., & Karlstrom, L. (2018). *The Chief Joseph Dike Swarm of the Columbia River Flood Basalts, and the legacy dataset of William H. Taubeneck.* Paper presented at the AGU Fall Meeting Abstracts.

Muir, R. (2017). Moving faults and building fracture models in a digital world—an example from Glen Coe, Scotland. *Geology Today, 33*(2), 54-59.

Neel, C., & Mueller, K. (2007). *Structural Analysis of Wrinkle-Ridge Rings on Lunae Planum and Hesperia Planum, Mars: Evidence of Buried Topography.* Paper presented at the Lunar and Planetary Science Conference.

Obrebski, M., Allen, R. M., Xue, M., & Hung, S. H. (2010). Slab-plume interaction beneath the Pacific Northwest. *Geophysical Research Letters, 37*(14).

Okubo, C. H., & Schultz, R. A. (2004). Mechanical stratigraphy in the western equatorial region of Mars based on thrust fault–related fold topography and implications for near-surface volatile reservoirs. *Geological Society of America Bulletin, 116*(5-6), 594-605.

Ostrach, L. R., Robinson, M. S., Whitten, J. L., Fassett, C. I., Strom, R. G., Head, J. W., & Solomon, S. C. (2015). Extent, age, and resurfacing history of the northern smooth plains on Mercury from MESSENGER observations. *Icarus, 250*, 602-622.

Pechmann, J. B., & Melosh, H. (1979). Global fracture patterns of a despun planet: Application to Mercury. *Icarus, 38*(2), 243-250.

Perrouty, S., Lindsay, M., Jessell, M., Aillères, L., Martin, R., & Bourassa, Y. (2014). 3D modeling of the Ashanti Belt, southwest Ghana: evidence for a litho-stratigraphic control on gold occurrences within the Birimian Sefwi Group. *Ore Geology Reviews, 63*, 252-264.

Peterson, G., Johnson, C., Byrne, P., Phillips, R., & Neumann, G. (2017). *Depth of Faulting in Mercury's Northern Hemisphere from Thrust Fault Morphology.* Paper presented at the Lunar and Planetary Science Conference.

Pfiffner, O. A. (1993). The structure of the Helvetic nappes and its relation to the mechanical stratigraphy. *Journal of structural Geology, 15*(3-5), 511-521.

Pfiffner, O. A. (2017). Thick-skinned and thin-skinned tectonics: A global perspective. *Geosciences, 7*(3), 71.

Phillips, R. J. (1991), Expected rates of Marsquakes: Scientific Rational and Requirements for a Global Seismic Network on Mars, in *Scientific Rationale and Requirements for a Global Seismic Network on Mars*, *Tech. Rep. 35-38*, pp. 35–38, LPI, Houston, TX.

Pike, R. J. (1988). Geomorphology of impact craters on Mercury. *Mercury, University of Arizona Press*, 165-273.

Plescia, J., & Golombek, M. (1986). Origin of planetary wrinkle ridges based on the study of terrestrial analogs. *Geological Society of America Bulletin, 97*(11), 1289-1299.

Pratt, T. L. (2012). Large-scale splay faults on a strike-slip fault system: The Yakima folds, Washington State. *Geochemistry, Geophysics, Geosystems, 13*(11).

Price, R., & Fermor, P. (1985). *Structure section of the Cordilleran foreland thrust and fold belt west of Calgary, Alberta. Geological Survey of Canada, Paper 84-14, 1 sheet. Price RA, Lis MG 1975. Recurrent displacements on basement-controlled faults across the Cordilleran Miogeocline in southern Canada.* Paper presented at the Geological Society of America Abstracts with Programs.

Provot, X. (1995). *Deformation constraints in a mass-spring model to describe rigid cloth behaviour.* Paper presented at the Graphics interface.

Ranero, C. R., Morgan, J. P., McIntosh, K., & Reichert, C. (2003). Bending-related faulting and mantle serpentinization at the Middle America trench. *Nature*, *425*(6956), 367.

Reidel, S., Campbell, N., Fecht, K., & Lindsey, K. (1993). *Late Cenozoic structure and stratigraphy of south-central Washington*. Retrieved from

Reidel, S. P. (1984). The Saddle Mountains; the evolution of an anticline in the Yakima fold belt. *American Journal of Science, 284*(8), 942-978.

Reidel, S. P. (1988). *Geologic map of the Saddle Mountains, south-central Washington*: Washington State Department of Natural Resources, Division of Geology and ….

Reidel, S. P., Camp, V. E., Tolan, T. L., Martin, B. S., Ross, M., Wolff, J., & Wells, R. (2013). The Columbia River flood basalt province: Stratigraphy, areal extent, volume, and physical volcanology. *The Columbia River flood basalt province: geological society of America special paper, 497*, 1-43.

Reidel, S. P., Martin, B. S., & Petcovic, H. L. (2003). The Columbia River flood basalts and the Yakima fold belt. *Western Cordillera and adjacent areas. Edited by TW Swanson. Geological Society of America Field Guide, 4*, 87-105.

Reidel, S. P., & Tolan, T. L. (2013). The late Cenozoic evolution of the Columbia River system in the Columbia River flood basalt province. *Geological Society of America Special Papers, 497*, 201-230.

Schellart, W., & Nieuwland, D. (2002). *4d modelling of pop-up structures during strike-slip faulting: some insights from analogue modelling.* Paper presented at the Geological Society of Australia Abstracts.

Schultz, R. A. (2000). Localization of bedding plane slip and backthrust faults above blind thrust faults: Keys to wrinkle ridge structure. *Journal of Geophysical Research: Planets, 105*(E5), 12035-12052.

Schultz, R. A. (2003). Seismotectonics of the Amenthes Rupes thrust fault population, Mars. *Geophysical Research Letters, 30*(6).

Schultz, R. A., Okubo, C. H., & Wilkins, S. J. (2006). Displacement-length scaling relations for faults on the terrestrial planets. *Journal of Structural Geology, 28*(12), 2182-2193.

Schultz, R. A., & Watters, T. R. (2001). Forward mechanical modeling of the Amenthes Rupes thrust fault on Mars. *Geophysical Research Letters, 28*(24), 4659-4662.

Schuster, J.E., 1994. Geologic Map of the east half of the Yakima 1:100,000 Quadrangle, Washington. Washington Division of Geology and Earth Resources: Open file report 94-12.

Shaw, J. H., Bilotti, F., & Brennan, P. A. (1999). Patterns of imbricate thrusting. *Geological Society of America Bulletin, 111*(8), 1140-1154.

Sherrod, B., Blakely, R. J., Lasher, J. P., Lamb, A., Mahan, S., Foit Jr, F., & Barnett, E. (2016). Active faulting on the Wallula fault zone within the Olympic-Wallowa lineament, Washington State, USA. *Bulletin, 128*(11-12), 1636-1659.

Sheth, H. (2018). Tectonic Deformation of Flood Basalt Provinces. In *A Photographic Atlas of Flood Basalt Volcanism* (pp. 275-286): Springer.

Shillington, D. J., Bécel, A., Nedimović, M. R., Kuehn, H., Webb, S. C., Abers, G. A., ... & Mattei-Salicrup, G. A. (2015). Link between plate fabric, hydration and subduction zone seismicity in Alaska. *Nature Geoscience*, *8*(12), 961.

Sibson, R. H. (1995). Selective fault reactivation during basin inversion: potential for fluid redistribution through fault-valve action. *Geological Society, London, Special Publications, 88*(1), 3-19.

Sibson, R. H., Robert, F., & Poulsen, K. H. (1988). High-angle reverse faults, fluid-pressure cycling, and mesothermal gold-quartz deposits. *Geology, 16*(6), 551-555.

Smith, S., Tesei, T., Scott, J., & Collettini, C. (2017). Reactivation of normal faults as high-angle reverse faults due to low frictional strength: Experimental data from the Moonlight Fault Zone, New Zealand. *Journal of Structural Geology, 105*, 34-43.

Solomon, S. C. (1976). Some aspects of core formation in Mercury. *Icarus, 28*(4), 509-521.

Solomon, S. C. (1977). The relationship between crustal tectonics and internal evolution in the Moon and Mercury. *Physics of the Earth and Planetary Interiors, 15*(2-3), 135-145.

Solomon, S. C. (1978). On volcanism and thermal tectonics on one-plate planets. *Geophysical Research Letters, 5*(6), 461-464.

Sperner, B., Müller, B., Heidbach, O., Delvaux, D., Reinecker, J., & Fuchs, K. (2003). Tectonic stress in the Earth's crust: Advances in the World Stress Map project. *Geological Society, London, Special Publications, 212*(1), 101-116.

Spudis, P. D., & Guest, J. E. (1988). Stratigraphy and geologic history of Mercury. In F. Vilas, C. R. Chapman, & M. S. Matthews (Eds.), *Mercury* (pp. 118-164). Tuscon, Arizona: University of Arizona Press.

Staisch, L., Blakely, R., Kelsey, H., Styron, R., & Sherrod, B. (2018). Crustal structure and Quaternary acceleration of deformation rates in central Washington revealed by stream profile inversion, potential field geophysics, and structural geology of the Yakima folds. *Tectonics, 37*(6), 1750-1770.

Staisch, L., Kelsey, H., Sherrod, B., Möller, A., Paces, J., Blakely, R., & Styron, R. (2018). Miocene–Pleistocene deformation of the Saddle Mountains: Implications for seismic hazard in central Washington, USA. *GSA Bulletin, 130*(3-4), 411-437.

Stern, R. J., & Gerya, T. (2018). Subduction initiation in nature and models: A review. *Tectonophysics*, *746*, 173-198.

Stern, R. J. (2004). Subduction initiation: spontaneous and induced. *Earth and Planetary Science Letters*, *226*(3-4), 275-292.

Stockmal, G. S., Lebel, D., Mcmechan, M. E., & Mackay, P. A. (2001). Structural style and evolution of the triangle zone and external Foothills, southwestern Alberta: Implications for thin-skinned thrust-and-fold belt mechanics. *Bulletin of Canadian Petroleum Geology, 49*(4), 472-496.

Storti, F., Salvini, F., & McClay, K. (1997). Fault-related folding in sandbox analogue models of thrust wedges. *Journal of Structural Geology, 19*(3-4), 583-602.

Strom, R. G., Banks, M. E., Chapman, C. R., Fassett, C. I., Forde, J. A., Head III, J. W., . . . Solomon, S. C. (2011). Mercury crater statistics from MESSENGER flybys: Implications for stratigraphy and resurfacing history. *Planetary and Space Science, 59*(15), 1960-1967.

Strom, R. G., & Neukum, G. (1988). The cratering record on Mercury and the origin of impacting objects. *Mercury, University of Arizona Press*, 336-373.

Strom, R. G., Trask, N. J., & Guest, J. E. (1975). Tectonism and Volcanism on Mercury. *Journal of Geophysical Research, 80*(17), 2478-2507.

Suppe, J. (1983). Geometry and kinematics of fault-bend folding. *American Journal of science, 283*(7), 684-721.

Suppe, J. (1990). Geometry and Kinematics of fault-propagation folding. *Ecologae Geologias Helvetiae, 83*, 409-454.

Susorney, H., Barnouin, O., Ernst, C., & Byrne, P. (2017). The surface roughness of Mercury from the Mercury Laser Altimeter: Investigating the effects of volcanism, tectonism, and impact cratering. *Journal of Geophysical Research: Planets, 122*(6), 1372-1390.

Susorney, H. C., Barnouin, O. S., Ernst, C. M., & Johnson, C. L. (2016). Morphometry of impact craters on Mercury from MESSENGER altimetry and imaging. *Icarus, 271*, 180-193.

Swanson, D., Wright, T., Camp, V., Gardner, J., Helz, R., Price, S., . . . Ross, M. (1980). *Reconnaissance geologic map of the Columbia River Basalt group, Pullman and Walla Walla quadrangles, southeast Washington and adjacent Idaho*. Retrieved from

Swanson, D. A., Wright, T., Hooper, P., & Bentley, R. (1979). *Revisions in stratigraphic nomenclature of the Columbia River Basalt Group*. Retrieved from

Tabor, R., Frizzell Jr, V., Vance, J., & Naeser, C. (1984). Ages and stratigraphy of lower and middle Tertiary sedimentary and volcanic rocks of the central Cascades, Washington: Application to the tectonic history of the Straight Creek fault. *Geological Society of America Bulletin, 95*(1), 26-44.

Tanner, D. C., Brandes, C., & Leiss, B. (2010). Structure and kinematics of an outcrop-scale fold-cored triangle zone. *AAPG bulletin, 94*(12), 1799-1809.

Terzopoulos, D., Platt, J., Barr, A., & Fleischer, K. (1987). Elastically deformable models. *ACM Siggraph Computer Graphics, 21*(4), 205-214.

Thompson, R. (1981). The nature and significance of large 'blind' thrusts within the northern Rocky Mountains of Canada. *Geological Society, London, Special Publications, 9*(1), 449-462.

Tolan, T. L., Martin, B. S., Reidel, S. P., Anderson, J. L., Lindsey, K. A., & Burt, W. (2009). An introduction to the stratigraphy, structural geology, and hydrogeology of the Columbia River Flood-Basalt Province: A primer for the GSA Columbia River Basalt Group field trips. *Geol. Soc. Am. Field Guide, 15*, 599-643.

Tosi, N., Grott, M., Plesa, A. C., & Breuer, D. (2013). Thermochemical evolution of Mercury's interior. *Journal of Geophysical Research: Planets, 118*(12), 2474-2487.

Tozer, R., Butler, R., & Corrado, S. (2002). Comparing thin-and thick-skinned thrust tectonic models of the Central Apennines, Italy. *EGU Stephan Mueller Special Publication Series, 1*, 181-194.

Trask, N. J. (1967). Distribution of lunar craters according to morphology from Ranger VIII and IX photographs. *Icarus, 6*(1-3), 270-276.

Trask, N. J. (1971). Geologic comparison of mare materials in the lunar equatorial belt, including Apollo 11 and Apollo 12 landing sites. *Geological Survey Research*, D138-D144.

Trask, N. J., & Guest, J. E. (1975). Preliminary geologic terrain map of Mercury. *Journal of Geophysical Research, 80*(17), 2461-2477.

Turcotte, D., & Schubert, G. (2014). *Geodynamics*. Cambridge, United Kingdom. Cambridge University Press.

United States Geological Survey, 2010. Modeled Combined Extent of All Columbia River Basalt Units. Water Resources NSDI Node.

United States Geological Survey, 2006. Quaternary fault and fold database for the United States.

United States Geological Survey, 2002. 10-meter DEMS in Yakima and Walla Walla Quadrangles. Earth and Space Sciences Department, University of Washington.

Unruh, J., & Humphrey, J. (2017). Seismogenic deformation between the Sierran microplate and Oregon Coast block, California, USA. *Geology, 45*(5), 415-418.

Vermilye, J. M., & Scholz, C. H. (1998). The process zone: A microstructural view of fault growth. *Journal of Geophysical Research: Solid Earth, 103*(B6), 12223-12237.

Walsh, L. S., Watters, T. R., Banks, M. E., & Solomon, S. C. (2013). *Wrinkle ridges on Mercury and the Moon: a morphometric comparison of length-relief relationships with implications for tectonic evolution.* Paper presented at the Lunar and Planetary Science Conference.

Wang, Y., Xiong, Y., Xu, K., Tan, K., & Guo, G. (2006). *A mass-spring model for surface mesh deformation based on shape matching.* Paper presented at the GRAPHITE.

Watkins, H., Bond, C. E., & Butler, R. W. (2014). Identifying multiple detachment horizons and an evolving thrust history through cross-section restoration and appraisal in the Moine Thrust Belt, NW Scotland. *Journal of Structural Geology, 66*, 1-10.

Watters, T., Solomon, S., Klimczak, C., Selvans, M., Walsh, L., Banks, M., . . . Murchie, S. (2013). *Distribution of prominent lobate scarps on Mercury: Contribution to global radial contraction.* Paper presented at the Lunar and Planetary Science Conference.

Watters, T. R. (1988). Wrinkle Ridge Assemblages on the Terrestrial Planets. *Journal of Geophysical Research-Solid Earth and Planets, 93*(B9), 10236-10254. doi:DOI 10.1029/JB093iB09p10236

Watters, T. R. (1989). *Periodically spaced anticlines of the Columbia Plateau* (Vol. 239): Geological Society of America Special Paper.

Watters, T. R. (1993). Compressional tectonism on Mars. *Journal of Geophysical Research: Planets, 98*(E9), 17049-17060.

Watters, T. R. (2004). Elastic dislocation modeling of wrinkle ridges on Mars. *Icarus, 171*(2), 284-294.

Watters, T. R., Cook, A., & Robinson, M. S. (2001). Large-scale lobate scarps in the southern hemisphere of Mercury. *Planetary and Space Science, 49*(14-15), 1523-1530.

Watters, T. R., Daud, K., Banks, M. E., Selvans, M. M., Chapman, C. R., & Ernst, C. M. (2016). Recent tectonic activity on Mercury revealed by small thrust fault scarps. *Nature Geoscience, 9*(10), 743.

Watters, T. R., & Nimmo, F. (2010). The tectonics of Mercury. *Planetary Tectonics, 11*, 15.

Watters, T. R., & Robinson, M. S. (1999). Lobate scarps and the Martian crustal dichotomy. *Journal of Geophysical Research: Planets, 104*(E8), 18981-18990.

Watters, T. R., Robinson, M. S., Beyer, R. A., Banks, M. E., Bell, J. F., Pritchard, M. E., . . . Williams, N. R. (2010). Evidence of Recent Thrust Faulting on the Moon Revealed by the Lunar Reconnaissance Orbiter Camera. *Science, 329*(5994), 936-940. doi:10.1126/science.1189590

Watters, T. R., Robinson, M. S., Bina, C. R., & Spudis, P. D. (2004). Thrust faults and the global contraction of Mercury. *Geophysical Research Letters, 31*(4).

Watters, T. R., Robinson, M. S., Collins, G. C., Banks, M. E., Daud, K., Williams, N. R., & Selvans, M. M. (2015). Global thrust faulting on the Moon and the influence of tidal stresses. *Geology, 43*(10), 851-854.

Watters, T. R., Schultz, R. A., & Robinson, M. S. (2000). Displacement-length relations of thrust faults associated with lobate scarps on Mercury and Mars: Comparison with terrestrial faults. *Geophysical Research Letters, 27*(22), 3659-3662.

Watters, T. R., Selvans, M. M., Banks, M. E., Hauck, S. A., Becker, K. J., & Robinson, M. S. (2015). Distribution of large-scale contractional tectonic landforms on Mercury: Implications for the origin of global stresses. *Geophysical Research Letters, 42*(10), 3755-3763.

Watters, T. R., Solomon, S. C., Klimczak, C., Freed, A. M., Head, J. W., Ernst, C. M., . . . Byrne, P. K. (2012). Extension and contraction within volcanically buried impact craters and basins on Mercury. *Geology, 40*(12), 1123-1126.

Watters, T. R., Solomon, S. C., Robinson, M. S., Head, J. W., André, S. L., Hauck II, S. A., & Murchie, S. L. (2009). The tectonics of Mercury: The view after MESSENGER's first flyby. *Earth and Planetary Science Letters, 285*(3-4), 283-296.

Wells, R., Bukry, D., Friedman, R., Pyle, D., Duncan, R., Haeussler, P., & Wooden, J. (2014). Geologic history of Siletzia, a large igneous province in the Oregon and Washington Coast Range: Correlation to the geomagnetic polarity time scale and implications for a long-lived Yellowstone hotspot. *Geosphere, 10*(4), 692-719.

Wells, R. E., & Heller, P. L. (1988). The relative contribution of accretion, shear, and extension to Cenozoic tectonic rotation in the Pacific Northwest. *Geological Society of America Bulletin, 100*(3), 325-338.

Wells, R. E., & McCaffrey, R. (2013). Steady rotation of the Cascade arc. *Geology, 41*(9), 1027-1030.

West, M., Ashland, F., Busacca, A., Berger, G., & Shaffer, M. (1996). Late Quaternary deformation, Saddle Mountains anticline, south-central Washington. *Geology, 24*(12), 1123-1126.

Williams, G., Powell, C., & Cooper, M. (1989). Geometry and kinematics of inversion tectonics. *Geological Society, London, Special Publications, 44*(1), 3-15.

Wilson, D. S. (1988). Tectonic history of the Juan de Fuca Ridge over the last 40 million years. *Journal of Geophysical Research: Solid Earth, 93*(B10), 11863-11876.

Wood, C., Head, J., & Cintala, M. (1977). *Crater degradation on Mercury and the Moon-Clues to surface evolution.* Paper presented at the Lunar and Planetary Science Conference Proceedings.

Wood, C. A., Higgins, W., Pau, K., & Mengoli, G. (2005). *The Lamont-Gardner Megadome Alignment: A Lunar Volcano-Tectonic Structure?* Paper presented at the 36th Annual Lunar and Planetary Science Conference.

Wright, J., Rothery, D. A., Balme, M. R., & Conway, S. J. (2018). Geological mapping of the Hokusai (H05) quadrangle of Mercury: Status update.

Yan, D. P., Xu, Y. B., Dong, Z. B., Qiu, L., Zhang, S., & Wells, M. (2016). Fault-related fold styles and progressions in fold-thrust belts: Insights from sandbox modeling. *Journal of Geophysical Research: Solid Earth, 121*(3), 2087-2111.

Yin, A. (1993). Left-slip evolution of the North Owl Creek fault system, Wyoming, during Laramide shortening. *Laramide basement deformation in the Rocky Mountain foreland of the Western United States, 280*, 229.

Young, W. C., Budynas, R. G., & Sadegh, A. M. (2002). *Roark's formulas for stress and strain* (Vol. 7): McGraw-Hill New York.

Yue, Z., Li, W., Di, K., Liu, Z., & Liu, J. (2015). Global mapping and analysis of lunar wrinkle ridges. *Journal of Geophysical Research: Planets, 120*(5), 978-994.

Zuber, M. T., Smith, D. E., Phillips, R. J., Solomon, S. C., Neumann, G. A., Hauck, S. A., . . . Johnson, C. L. (2012). Topography of the northern hemisphere of Mercury from MESSENGER laser altimetry. *Science, 336*(6078), 217-220.

APPENDIX A

SUPPLEMENTARY TEXT, CHAPTER 2

Introduction

These supplementary materials include datasets and computer code necessary for reproducing the results presented in the main text and figures of this paper and a movie, which provides additional understanding of the datasets and computational methods used to derive the radius change of Mercury that occurred during each of the planet's time-stratigraphic systems. Four datasets are available as additional downloads (from the publication file in *Geophysical Research Letters*), including three text files which contain information about craters and their morphologic and stratigraphic classifications. These three text files can be read into the fourth text file, which contains code written in the open source, free computer programming language R. The code was written by the authors and is commented in detail so that the interested reader is able to observe all steps of calculations along with written explanations of those steps. It should be noted that in order to reproduce our results using the code, the reader should add the first three provided datasets to their working directory before running the script. The two figures included illustrate the datasets of cut (Figure S1) and fault-superposing (Figure S2) craters derived from the first three datasets. The following materials also include four sections of text explaining how the area calculations were undertaken and a movie containing a graphical explanation of our calculations, which details how area ratios were used with radius change associated with faults cutting each time system's craters to derive the amount of radius change accumulated during each time system. The second section of text describes additional statistical tests to backup our approach. The third section of text provides additional details about how craters in stratigraphic relationships were mapped and organized. The fourth section describes our methods and their implications for our results in further detail than discussed in the main text.

Datasets containing information about craters and thrust faults were used in the study. A global dataset of thrust faults was obtained from Byrne et al. (2014). Kinczyk et al. (2016) shared a dataset of all craters larger than 40 km in diameter. These craters were morphologically classified. Kinczyk et al. (2016) did map many craters as small as 20 km diameter, but did not classify them into any morphologic group. These small craters were reviewed and classified as part of this research and further distinguished as cut by faults or superposing faults. Additionally, the entirety of the global mosaic was reviewed manually to locate additional 20 km or larger craters cut by or superposing faults. These craters were mapped and morphologically classified (DS 01). The set of larger, already classified craters was searched automatically to locate craters cut by faults (DS 02). Global datasets of cut and fault-superposing craters larger than 20 km were created from these efforts and used in our computations (displayed in Figures S2 and S3). These datasets were processed and computations were performed using the previously mentioned R code (DS 03).

Text S1. Area Calculations

Larger, older craters have higher probabilities of being cut by thrust faults because (1) they have existed on the surface of the planet longer and thus been exposed to longer periods of thrust fault activity and (2) they cover more of the planet's surface, increasing their geometric probability of being cut. The first component of this probability was approached using observations of stratigraphic relationships of craters of various time systems with thrust faults. To compare the geometric probabilities, the probabilities associated with surface coverage, we calculated the areas of craters associated with each time system during each time system throughout the planet's history using the ArcGIS geometry and overlay (union, dissolve, and intersect) toolboxes. The geometry toolbox was used so that accurate areas could be calculated for craters instead of areas distorted by the equirectangular projection of the map. Areas had to be recalculated during each time system because new craters superposed older craters, causing the crater areas to change over time. The surface areas of older craters decreased as younger craters were emplaced on top of them. We calculated the total surface area associated with each group of craters (craters belonging to each time system) during each period. When craters of the same age system overlapped, the superposing area was only considered once, so that an over-estimation of area did not propagate error. For example, to calculate time system areas during the Calorian, the area of any overlap between Calorian and Pre-Tolstojan or Tolstojan craters was subtracted from the previously calculated area of the Pre-Tolstojan and Tolstojan craters. Mansurian and Kuiperian craters areas were not considered for the Calorian, because during the Calorian, those craters would not have occupied any surface area. Only the dataset from Kinczyk et al. (2016) (DS 02) was used for the area calculations.

Because craters do not completely cover Mercury's surface, the areas occupied by craters during each time system by each system's craters were expressed as ratios. For example, during the Calorian, the area of Pre-Tolstojan and Tolstojan craters was ~ 2.27 x 10^7 km^2 and the area of Calorian craters was ~ 4.92 x 10^6 km^2. The areas of Mansurian and Kuiperian craters were 0 km^2 since at the time, none of these had been emplaced. Thus, the ratio of all four system areas (Pre-Tolstojan/Tolstojan to Calorian to Mansurian to Kuiperian) to each other can be expressed as 4.627:1:0:0. We then verified that thrust faulting was a global, relatively random, and uniform process at any given time (see text S2), so that during the Calorian, Pre-Tolstojan and Tolstojan craters could be assumed to be 4.627 times more likely to be cut by thrust faults than Calorian craters (and that it would be impossible for Mansurian and Kuiperian craters to be cut by faults during the Calorian).

Text S2. Additional statistical tests

In order for our results to be meaningful, we needed to verify that (1) the fault population used in the study was approximately uniformly distributed across the surface, (2) the distribution of craters across the surface is similar throughout each time system, and (3) the distributions of fault lengths within the sub-population of craters is approximately similar.

(1) Other authors have argued that because of processes like tidal despinning and variations in crustal thickness the distribution of faults across Mercury's surface is non-uniform (Watters et al., 2015; Byrne et al., 2014). In contrast, global contraction would be expected to produce a uniform distribution of faults (Melosh and McKinnon, 1988). We require the distribution of thrust faults to be more or less uniform to support the use of geometric probabilities. We created an equal-area mesh with 162 cells across Mercury's surface, and calculated the standard deviation of counts of fault midpoints in each mesh cell. We then devised a Bootstrap test, which created 100,000 artificial uniform fault distributions across Mercury's surface and calculated the standard

deviations for all the artificially produced fault-midpoint counts. The Bootstrap test allowed us to compare the known distribution of thrust faults on Mercury to many spatially uniform thrust fault distributions, so that even slight differences between observed and expected distributions could be detected. We found the standard deviation of the distribution of these rooted counts (~2.27) and compared it to our distribution of theoretical standard deviations (~0.56). For the observed fault distribution, we found that aside from ~15 of the mesh cells, the remaining 147 cells were approximately uniform (code for the test is included in DS03). The 15 clustered cells were located in the smooth plains, which did not show many stratigraphic relationships (<30 Calorian or Mansurian craters), and thus was not a concern.

(2) For our analysis, we used craters that were either automatically detected as cut by faults by the intersect function in ArcMap or that were visually found to be superposed or intersected by an unmapped fault. Although craters are not distributed randomly across the surface of Mercury (Strom et al., 2011), it was necessary to confirm that during each time system, craters were emplaced in approximately the same locations (i.e. their distributions could not be easily distinguished from each other). We constructed 95% confidence intervals for crater locations both longitudinally and latitudinally across each time system. Across latitudes, only Tolstojan craters can be distinguished from the other crater sub-populations (likely because so many of these craters existed that the confidence interval was narrowed). Longitudinally, only Kuiperian craters could be distinguished from the other distributions. Because most of the distributions of sub-populations of craters cannot be readily distinguished, we can assume that crater

populations can be treated reasonably as having equal chances of their localities being affected by global contraction.

Table A1.1 Latitudes (all values in degrees)

	Pre-T	Tolstojan	Calorian	Mansurian	Kuiperian
Mean	-3.48	-11.31	-7.22	-1.09	-5.82
St Dev.	40.59	37.80	39.13	40.02	33.94
95% Int.	-5.98, -0.99	-13.37, -9.24	-10.54, -3.90	-6.14, 3.95	-20.87, 9.23

Table A1.2 Longitudes (all values in degrees)

	Pre-T	Tolstojan	Calorian	Mansurian	Kuiperian
Mean	-8.26	-3.40	-10.20	-4.58	-59.79
St Dev.	110.87	99.84	93.34	102.37	85.89
95% Int.	-15.08, -1.45	-8.85, 2.055	-18.12, 2.28	-17.49, 8.33	-97.87, -21.71

(3) Longer thrust faults accommodate more shortening than shorter faults (Cowie and Scholz, 1992), so it is necessary to determine that no individual sub-population of craters contains all the long faults or all the short faults, but rather that each time system has a similar fault length distribution. We compared the cumulative number of faults of a given length against those lengths for three fault groups: faults that cut Pre-Tolstojan and Tolstojan craters, faults that cut Calorian craters, and faults that cut Mansurian craters. Since these curves have approximately the same slope (~ 0.01, Figure S1), we can assume that the distributions of fault lengths within the fault sub-populations are

approximately equal, even if their absolute count is not. This indicates that an equal ratio of small-to-long faults cut each sub-population of craters. For this reason, it is not necessary to break up the faults based on length nor quantify the strain for each individual fault.

Table A1.3 Cumulative Fault Length Distributions

Bin (< x km)	PTT-cumu	M-cumu	C-cumu	All-cumu
0	2196	70	322	5925
50	1323	35	206	3291
100	452	9	80	1034
150	200	4	41	383
200	112	2	25	177
250	53	1	11	69
300	30	1	4	48
350	20	1	4	33
400	12	1	3	22
450	10	0	2	17
500	8	0	0	12
550	4	0	0	6
600	3	0	0	4
650	2	0	0	3
700	2	0	0	3
750	2	0	0	3
800	0	0	0	1
850	0	0	0	1
900	0	0	0	1
950	0	0	0	0

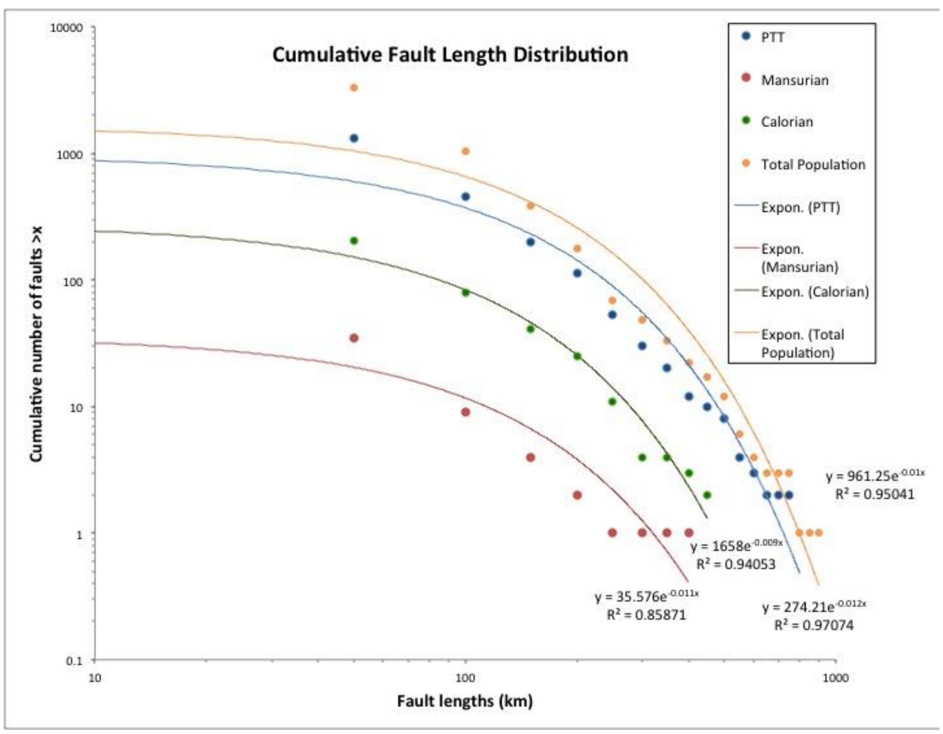

Figure A1.1 Cumulative fault length distributions are shown for faults cutting Mansurian (red), Calorian (green), and Pre-Tolstojan or Tolstojan craters (blue). The cumulative fault length distribution for the entire fault population regardless of stratigraphic relationship with craters is shown in orange. Exponential best-fit models are given for each fault population, as well as the associated R^2 values. The slopes of these lines (exponent of e) exhibit a tight range of values from 0.009 to 0.012, indicating similar length distributions across the four populations. The curves were calculated using the data displayed in the table above. For simplicity, cumulative counts of faults longer than given lengths were organized into 50 km bins. Binning generated artifacts, like the horizontal pattern of points representing the longest fault, in the fault length distribution plot.

Text S3. Specifics on Crater Selection

For our analyses of stratigraphic relationships of craters and faults, we carefully selected craters crosscut by faults and craters that superpose faults. Kinczyk et al. (2016) morphologically classified craters as small as 40 km, but they mapped craters as small as 20 km in diameter. We used the "select by location" function in ArcMap to select all craters that were intersected by faults. We morphologically classified craters that were intersected by faults, but were not classified in the original dataset (i.e. those smaller than 40 km in diameter). All intersected craters were loaded into their own shapefile. In the attribute table for this shapefile, we added a column called "Status". Craters cut by faults were coded as "0" and craters that superposed faults were coded as "1". To find the craters that superposed faults, as well as additional unmapped craters larger than 20 km and in stratigraphic relationships with faults, we visually inspected the entire planet on a scale of 1:2,000,000. We divided the planet into 10° x 10° bins. To inspect craters within each bin, we first used the global morphology mosaic, and the East and West illumination high incidence angle mosaics (http://messenger.jhuapl.edu/Explore/Images.html#global-mosaics). Unmapped craters in stratigraphic relationships with faults were organized into their own shapefile, and again, their stratigraphic status was coded. Thrust fault-related landforms were considered to cross-cut a crater if they cut the ejecta blanket, rim, and/or floor of the crater. We also marked thrust fault-related landforms that were superposed by ejecta blankets and classified the associated crater as superposing a fault.

Text S4. Details of Methods and Implications For Results

Our analysis uses all thrust fault-related landforms in stratigraphic relationships with craters constituting 2,588 out of the total fault population (~ 6,000), regardless of location, orientation, or formation mechanism, were used to identify craters in stratigraphic relationships with such landforms. These landforms are characterized by steeply sloping scarp faces and long, shallowly sloping back limbs, which together are thought to represent an anticline or monocline that formed as surface expression above deep-seated thrust faults. Wrinkle ridges are a qualitatively defined class of thrust fault-related landform, which are generally characterized as broad and symmetrical, and therefore represent a structure more similar to an anticline (Strom et al., 1975). We use all these structures because our analysis investigates the history of thrust faulting as a means of learning about global contraction, and thus, thrust faulting must be the process investigated. Secondly, because global contraction is a long-lived process, any local processes that formed sub-populations of thrust faults, would have taken place in the context of global contraction. Therefore, global contraction would have still influenced the growth of these sub-populations of thrusts. Finally and most importantly, there is no method of distinguishing thrust fault-related landforms from the processes that form them. This is why we do not use the previously applied term "wrinkle ridge" and combine all structures that occur in smooth plains units into this category (see reasons presented in Byrne et al. (2014) for using the term "smooth plains structure").

We show via a bootstrap test described in Text S2 that the distribution of thrust fault-related landforms on Mercury is approximately uniform, and therefore our analysis may be conducted. Previous studies have shown that the orientations of thrust fault-related landforms are not uniform, and that landforms in the equatorial and mid-latitudes are preferentially oriented North to South, given some uncertainty with illumination conditions on Mercury (Byrne et al., 2014). This orientation distribution may be due to an influence of tidal despinning on global contraction, which may have modified the global stress field such that a temporal overlap of the two processes would have produced the observed preferential orientation of thrust faults (Klimczak et al., 2015). After this period of despinning, global cooling caused volumetric contraction, reactivating the thrust faults and further developing their associated landforms (Dombard and Hauck, 2008). The preferred orientations of landforms do not impact our results, as faults are only used to determine cross-cutting relationships with craters.

We attributed all thrust fault related landforms in some part to global contraction and did not statistically represent other formation processes. Previous authors have published on alternative formation processes to certain thrust fault-related landforms on Mercury but these studies did not conduct specific analyses to substantiate in how far these alternative processes played a role to form the landforms. For example, thrust fault-related landforms in the southern hemisphere have been proposed to grow from stresses associated with mantle convection and structures located in smooth plains have been related to subsidence. To our knowledge, these hypotheses have not been tested and no strain calculations have been published for us to use, and so we cannot further sub-divide Mercury's thrust fault population into faults related to global contraction and those formed by other processes.

Landforms described as "wrinkle ridges" have previously been proposed to form from processes other than global contraction. We did not address such landforms as separate population of fault-related landform, since no work in the literature quantified in how far other processes have played a role in their formation. In addition, global contraction was given as one reason to have substantially contributed to the development of similar thrust fault-related landforms contained in mare units on the Moon (Byrne et al*.,* 2015). All thrust faults are found in, and thus are part of the global contractional tectonic regime, and so reflect shortening strain rates and shortening strain percentages from global contraction, even in the context of other, overlapping tectonic processes.

Interpreting stratigraphic relationships between thrust fault-related landforms and craters is a complex process that requires detailed observation and consideration of timing of fault growth. Individual faults can have stratigraphic relationships with multiple craters; however, our analysis focused on the craters themselves, with faults simply being used to classify those craters into two groups: craters representing a time and place with active thrust faulting or craters representing a time and place without active thrust faulting. Therefore, our analysis is unaffected by a crater being cut by faults multiple times or by a crater superposing a fault and also being cut by a fault. These craters could have been cut during any time following emplacement and some or all of a potentially pre-existing fault may have been erased. When only looking at the crosscutting relationships on the crater floors, any strain that may or may not have been accommodated prior to the impact was erased by the impact. Therefore, all the currently observed strain on a crater floor occurred after the impact. The timing relationship interpreted at each individual cross-cut crater may neglect that some portion of the fault could have existed prior to the impact event (and there is no way of accounting for it other than acknowledging that fact), which is why we (1) complemented the analysis of cross-cut craters with the analysis of the superposing craters (where all of the fault existed prior to emplacement) and (2) assess all existing stratigraphic relationships of scarps and craters found on Mercury to obtain a statistical/quantitative answer. Slip can also happen at different locations along a fault. It is also possible that a fault superposed by a crater could grow at locations exterior to the crater after impact; however, because our sample size of craters and faults is so large, this would have to be an extremely common occurrence along most faults for this process to impact our results. If the fault growth along such a fault were substantial, eventually, the deformation within the crater would become visible, and the crater would be recorded as "cut" by the fault.

Assessing these relationships with observations was not straightforward in the case of every crater. For example, in Figure 1g within the main text, a thrust fault-related landform appears to crosscut the ejecta blanket of a crisp Kuiperian crater. In many cases, a thrust fault-related landform cutting an ejecta blanket would have caused that crater to be classified as “cut”; however, in this case, the crater rim, terraces, and floor are not modified by the fault and when observed at smaller scales, the ejecta blanket superposes and so mutes the scarp face. Away from the ejecta blanket, the scarp remains steep with a crisp surface break. This was often the case with younger Mansurian and Kuiperian craters with clearly identifiable ejecta blankets (such as that shown in Figure 1f). Because these craters were often smaller than their older counterparts, their ejecta blankets may not have been large enough to completely erase fault-related topography near their rims.

Preservation bias may also have affected our results, as the oldest thrust fault-related landforms may not have been preserved. A few preserved cross-cutting relationships show that thrust fault-related landforms on Mercury formed as early as the Pre-Tolstojan or Tolstojan systems, but that this occurrence was at a few isolated localities. There are very few Tolstojan or Pre-Tolstojan craters that are observed to superpose thrust fault-related landforms, compared to the greater proportions of Calorian, Mansurian, and Kuiperian craters that superpose thrust fault-related landforms. It is possible that other Pre-Tolstojan and Tolstojan craters superposed thrust-fault related landforms that have not been preserved; however, had the formation of stratigraphic relationships between craters and thrust fault-related landforms been a common occurrence in the Pre-Tolstojan and Tolstojan, we would expect the proportion of preserved Pre-Tolstojan and Tolstojan craters superposing thrust-fault related landforms to be greater. Instead, we observe 1192 out of 1196 of these old craters to be cross-cut by faults. Because many ancient crater rims are preserved, it is unlikely that similarly large linear landforms such as fault scarps would not be preserved. Both landforms have very little topography compared to their length dimensions (see crater diameter-to-rim height relationship (Pike, 1988) and fault-scaling relationships (Susorney et al., 2016)). We also note that if thrust faulting were an ancient process not active in more recent times, we would not observe younger craters cross-cut by thrust fault-related landforms. Our observations that the proportion of superposing craters increases in each time system, but that some cross-cut craters remain (with the exception of the Kuiperian) indicates that thrust faulting is a long lived process that has operated at different rates during each period of Mercury’s history.

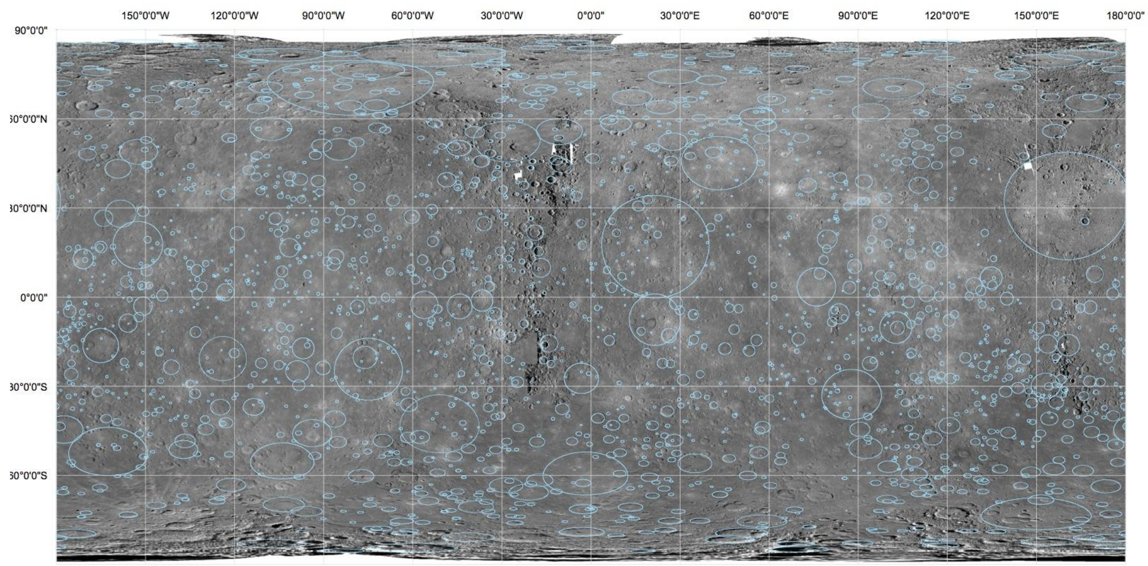

Figure A1.2 All craters larger than 20 km in diameter cut by thrust faults are outlined in blue. Here, we do not show differentiation between craters of various morphologic classes

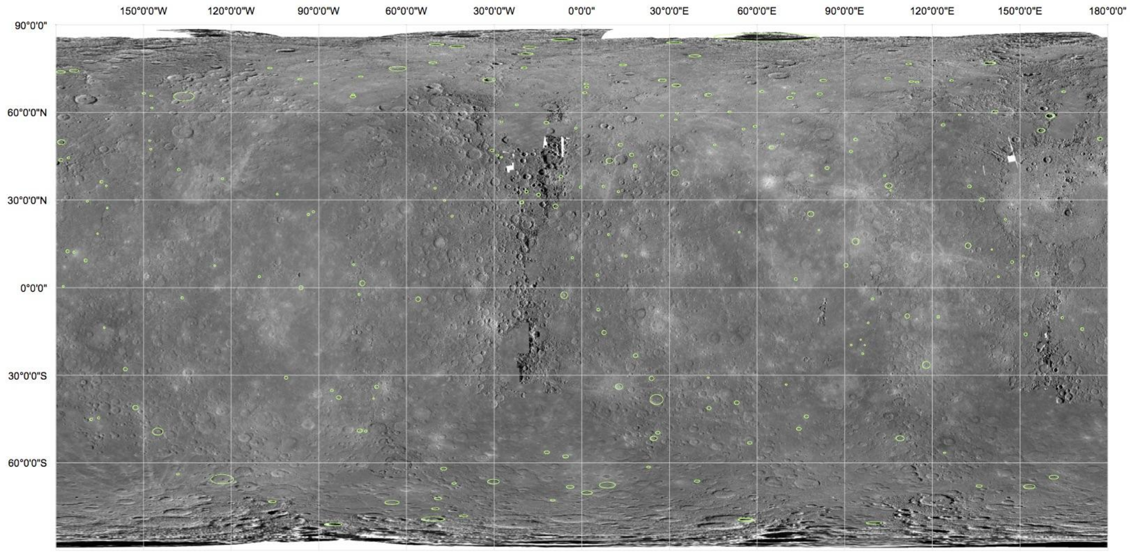

Figure A1.3 All craters larger than 20 km in diameter that superpose thrust faults are outlined in green. Again, none of these craters are classified morphologically in this map.

<u>Data</u>

Datasets may be downloaded from the supplementary materials available with the publication of this article in *Geophysical Research Letters.*

Dataset S1. This table includes over 600 rows containing data about all craters greater than 20 km originally unclassified into morphologic classes by Kinczyk et al. (2016) that are cut by or superpose faults. Craters that superpose faults were not able to be located automatically, and so these were added to this dataset manually by searching the entire planet visually. The latitude and longitude of the crater center, diameter, crater class (classified specifically for this study), and stratigraphic status (cut or uncut, classified by the authors) are all included as columns.

Dataset S2. This table includes over 2000 rows containing data about the craters cross-cut by faults. The columns include the latitudes and longitudes of the crater center, diameter, and crater class (classified by Kinczyk et al. (2016)) are all included as columns. The ArcGIS function "select by location" was used to locate all craters intersected, or cut, by thrust faults.

Dataset S3. Code, written using the computer language R, that reads in three crater datasets and organizes craters into two new crater datasets: all cut craters and all fault-superposing craters. Two of the datasets are available as supplementary materials, and the third, a complete set of all mapped and age-classified craters, is available from Kinczyk et al. (2016). The code then computes the percent of craters that are cut and are classified within each time system. We then normalize these percentages so that they total 100%, thereby allowing us to directly compare the degree of thrust faulting activity that affected craters of each time system (during that or any subsequent time system). The area ratios discussed above are hard coded, and so are not derived within this code.

The code then computes the amount of radius change accumulated by faults within terrains of each time system, but not necessarily accumulated *during* the time system associated with those terrains, by multiplying the previously calculated percentages by the total assumed radial change amount in km. This allows us to take into account that although a fault may cut a crater morphologically classified within a particular time system, that fault may have formed and grown during that or any subsequent time system. We also calculate the upper and lower bounds for radius change associated with each time system terrain using total radius changes of 3.1 km and 7.1 km. These amounts are then multiplied by the area ratios to calculate the amount of change accommodated by thrust faults within each time system's craters during each time system beginning with the most recent system, the Kuiperian.

We are then able to total the amount of radius change accumulated during each time system. Using the total radius change assumed and current radius of Mercury, the code computes the original radius prior to radial contraction, compares this amount to the change associated with the time system, and thereby, computes a strain percentage associated with the Mansurian and Calorian. The code then calculates average strain rate during each time system by comparing the total radius change accommodated during each system to the length of those systems and radius of Mercury (equation below). Because variation exists between estimates of total radius change (e.g. Di Achille et al., 2012; Watters et al., 2013; Byrne et al., 2014) and estimates of lengths of time systems (e.g. Spudis and Guest, 1988; Banks et al., 2016), the code computes lower bounds, averages, and upper bounds for each combination of radial contraction and time system length using the equation below. Minimum and maximum strain rate values associated with possible time system lengths and amounts of radius change are given in the tables below. Plots, which translate to the components of Figure 2, are then generated. For any time system x:

$$\boldsymbol{strain\ rate_x} = \frac{\boldsymbol{radius\ change_x}}{\boldsymbol{t_x * 3.1556952 * 10^{16} * R_o}}$$

$\boldsymbol{t_x}$ ≔ time system length in Ga

$\boldsymbol{R_o}$ ≔ radius prior to global contraction

The second major section of the code computes the lengths of time for topographic development and slip rates discussed in the implications section. It computes the shortening associated with each fault from values for their topography (Adventure and Enterprise Rupes), and then, using the strain rates derived in the first section of the code, computes the growth time and slip rates for the two faults.

Table A1.4 Calorian Strain Rates (s^{-1})

	Maximum Length= 2 Ga (*Spudis and Guest*, 1988; *Banks et al.*, 2016)	Minimum Length=0.4 Ga (*Spudis and Guest*, 1988)
ΔR= 3.1 km	7.58×10^{-21}	3.79×10^{-20}
ΔR= 5.1 km	1.32×10^{-20}	6.59×10^{-20}
ΔR= 7.1 km	1.83×10^{-20}	9.16×10^{-20}

Table A1.5 Mansurian Strain Rates (s^{-1})

	Maximum Length= 3.3 Ga (*Spudis and Guest*, 1988; *Braden and Robinson*, 2013)	Minimum Length= 0.9 Ga (*Spudis and Guest*, 1988; *Banks et al.*, 2016)
ΔR= 3.1 km	$7.59x10^{-21}$	$2.78x10^{-20}$
ΔR= 5.1 km	$1.25x10^{-20}$	$4.572857x10^{-20}$
ΔR= 7.1 km	$1.73x10^{-20}$	$6.36x10^{-20}$

Movie S1. This video displays a step-by-step graphical explanation of our radius change per time system calculation. We begin with the current estimate of km of radius change accommodated by the four groups of faults, fault cutting each time system's craters. We back calculate how many km of change each group would have accommodated during each time system by relating each time system's area to the area of other time system terrains. At the start of the Calorian, all radius change estimated for Mercury has been accumulated within faults cutting all four terrains, and thus, no radius change remains to be accumulated in the Pre-Tolstojan and Tolstojan systems.

APPENDIX B

SUPPLEMENTARY R CODE, CHAPTER 2

```
# Please note that this working directory should be modified depending
on where supplementary
# files are stored.

c0c <- read.table('crane-ds01.txt', header=TRUE, sep=',')

mc <- read.table('crane-ds03.txt', header=TRUE, sep=',')

# I need to clear out the rows from mc that are going to be repeats in
c0c
# Class 0 craters were all initially age 0 or not created, so all rows
with 0 age values can be eliminated.
mc <- mc[mc$CTR_CLASS != '0', ]

# Combine the class 0 craters and the multiclass craters. This group
represents cut
# and fault-superposing craters.
cc <- rbind(c0c, mc)

# Check values; this plot checks to see that the numbers of craters
belonging to each class seems reasonable
cc.counts <- table(cc$CTR_CLASS)
barplot(cc.counts)

# Craters that are cut by faults
cutCraters <- cc[cc$Status == '0', ]
# Craters that superpose faults
fsCraters <- cc[cc$Status == '1', ]

# Read in the file of all craters total
# THIS FILE MUST BE AQUIRED FROM KINCZYK ET AL. [2016]
ac <- read.table('crane-ds02.txt', header=TRUE, sep=',')

n.cut.12 <- sum(cutCraters$CTR_CLASS == '1' | cutCraters$CTR_CLASS ==
'2' )
n.cut.3 <- sum(cutCraters$CTR_CLASS == '3')
n.cut.4 <- sum(cutCraters$CTR_CLASS == '4')
n.cut.5 <- sum(cutCraters$CTR_CLASS == '5')

total.craters <- nrow(ac)
total.craters

# Some craters are unclassified or classified as 'ghost' (class 6)
craters. To get an understanding
of how many classified craters belong to which systems, we'll filter
these out and find our percentages
total.craters.class <- sum(ac$CTR_CLASS == '1' | ac$CTR_CLASS == '2' |
ac$CTR_CLASS == '3' | ac$CTR_CLASS == '4' | ac$CTR_CLASS == '5')
total.craters.class
```

```
# PT/T percent cut
n.cut.12/total.craters.class*100
# C percent cut
n.cut.3/total.craters.class*100
# M percent cut
n.cut.4/total.craters.class*100
# K percent cut
n.cut.5/total.craters.class*100

per.cut.and.c12 <- n.cut.12/total.craters
per.cut.and.c3 <- n.cut.3/total.craters
per.cut.and.c4 <- n.cut.4/total.craters
per.cut.and.c5 <- n.cut.5/total.craters

# In comparative terms, what percent of faults in relationships with
craters cut
# craters of each age. I'll find this by normalizing the above
percentages to 100% or 1

per.12faults <- per.cut.and.c12/sum(per.cut.and.c12, per.cut.and.c3,
per.cut.and.c4, per.cut.and.c5)
per.3faults <- per.cut.and.c3/sum(per.cut.and.c12, per.cut.and.c3,
per.cut.and.c4, per.cut.and.c5)
per.4faults <- per.cut.and.c4/sum(per.cut.and.c12, per.cut.and.c3,
per.cut.and.c4, per.cut.and.c5)
per.5faults <- per.cut.and.c5/sum(per.cut.and.c12, per.cut.and.c3,
per.cut.and.c4, per.cut.and.c5)

# Percent faults expected associated with PT/T, C, M, and K systems
per.12faults
per.3faults
per.4faults
per.5faults

# ------ NOTE: Area ratios --------
# Area ratios were calculated in arc map and will appear below as
"magic" numbers.
# However, if interested in seeing the original files or how
calculated, check the
# areas text file in supplementary materials or contact corresponding
author
# ---------------------------

# ----- Radius Change and Strain calculations -----------

# Assuming 5.1 km of radius change (radius change accommodated by
faults in PT/T, C, M, and K terrains)
st.12 <- 5.1*per.12faults
st.3 <- 5.1*per.3faults
st.4 <-5.1*per.4faults
st.5 <- 5.1*per.5faults

st.12
st.3
st.4
st.5
```

```
# Because of 0 km is accumulated by K faults, we can't discuss how many more times radius change
# was accumulated by other fault populations during this time because anything times 0 is 0
K.total <- 0

# Mansurian radius changes accommodated by M, C, and PT/T fault groups followed by total Mansurian system change
st.4.M <- st.4 * 1
st.3.M <- st.4 * 3.25
st.12.M <- st.4 * 14.9
M.total <- st.4.M + st.3.M + st.12.M
M.total

# Strain associated with this change
M.total/2445.1*100

# Calorian radius changes accommodated by C and PT/T fault groups followed by total Calorian system change
st.3.C <- st.3 * 1 - st.3.M
st.12.C <- st.3.C * 4.627
C.total.limit <- 5.1- M.total
C.total <- st.3.C + st.12.C
C.total

# Strain associated with this change
C.total/2445.1*100

# Pre-tolstojan and Tolstojan radius changes
st.12.PTT <- st.12 - st.12.M - st.12.C
# Note that because the radius change slightly exceeds 5.1 km, there must not be any change left to accumulate during the PT/T
P.total <- 0


# Using the upper bound of 7.1 km of radius change, note that bounds are symmetric -------------------------

st.12.u <- 7.1*per.12faults
st.3.u <- 7.1*per.3faults
st.4.u <-7.1*per.4faults
st.5.u <- 7.1*per.5faults
# If interested, subtract the original st.x values from these values to find error bounds

# Mansurian UB radius change
st.4.M.u <- st.4.u * 1
st.3.M.u <- st.4.u * 3.25
st.12.M.u <- st.4.u * 14.9
M.total.u <- st.4.M.u + st.3.M.u + st.12.M.u
# If interested, subtract the original st.x.M values from these values to find error bounds

# Strain associated with this change
M.total.u/2447.1*100
```

```
# Calorian UB radius change
st.3.C.u <- st.3.u * 1 - st.3.M.u
st.12.C.u <- st.3.C.u * 4.627
C.total.u <- st.12.C.u + st.3.C.u
# If interested, subtract the original st.x.C values from these values
to find error bounds

# Strain associated with this change
C.total.u/2447.1*100

# Pre-tolstojan and Tolstojan Change
P.total <- 0

# ------------ Strain rates -----------------
#These strain rates can be re-calculated for given lengths of time
systems by replacing the
# lengths of time systems in each x.strainrate calculation. This value
is the number in
# billion years given before the variable "s". Ex. 2.25 in m.strainrate

# seconds per 1 billion year
s <- 31556952000000000

# PT/T strain rates (prior to the onset of faulting)
excessprecal.strain.rate.lb21 <- (2.1)/(.6*s*2443.1)
excessprecal.strain.rate.lb21
excessprecal.strain.rate.ub21 <- (2.1)/(.1*s*2447.1)
excessprecal.strain.rate.ub21

excessprecal.strain.rate.lb14 <- (1.7)/(.6*s*2443.1)
excessprecal.strain.rate.lb14
excessprecal.strain.rate.ub14 <- (1.7)/(.1*s*2447.1)
excessprecal.strain.rate.ub14


#LOWER BOUNDS
lb.c.strainrate <- 1.169751/(.65*s*2443.1)
lb.m.strainrate <- 1.93/(2.25*s*2443.1)
lb.k.strainrate <- 0

#ESTIMATE
c.strainrate <- C.total/(.65*s*2445.1)
c.strainrate
m.strainrate <- M.total/(2.25*s*2445.1)
m.strainrate

#UPPER BOUNDS
ub.c.strainrate <- C.total.u/(.65*s*2447.1)
ub.m.strainrate <- M.total.u/(2.25*s*2447.1)
# If interested, subtract the original x.strainrate values from these
values to find error bounds

byrne_sg_c <- c(lb.c.strainrate, c.strainrate, ub.c.strainrate)
byrne_sg_m <- c(lb.m.strainrate, m.strainrate, ub.m.strainrate)

#There will also need to be values calculated for different time system
lengths and different
```

```
#radius change estimates.
# -------------------
#Byrne radius change with Banks 2016 time systems
lb.c.strainrate.byrnebanks <- 1.169751/(2*s*2443.1)
lb.m.strainrate.byrnebanks <- 1.93/(1.6*s*2443.1)
lb.k.strainrate.byrnebanks <- 0

#ESTIMATE
c.strainrate.byrnebanks <- C.total/(2*s*2445.1)
c.strainrate.byrnebanks
m.strainrate.byrnebanks <- M.total/(1.6*s*2445.1)
m.strainrate.byrnebanks

#UPPER BOUNDS
ub.c.strainrate.byrnebanks <- C.total.u/(2*s*2447.1)
ub.m.strainrate.byrnebanks <- M.total.u/(1.6*s*2447.1)
# If interested, subtract the original x.strainrate values from these
values to find error bounds

byrne_banks_c <- c(lb.c.strainrate.byrnebanks, c.strainrate.byrnebanks,
ub.c.strainrate.byrnebanks)
byrne_banks_m <- c(lb.m.strainrate.byrnebanks, m.strainrate.byrnebanks,
ub.m.strainrate.byrnebanks)

# ----------------------------------------------------------------------
# DiAchille radius change estimates with 2.4, 3, and 3.6 as total
changes
# Assuming 3 km of radius change (radius change accommodated by faults
in PT/T, C, M, and K terrains)
st.12.da <- 3*per.12faults
st.3.da <- 3*per.3faults
st.4.da <-3*per.4faults
st.5.da <- 3*per.5faults

st.12.da
st.3.da
st.4.da
st.5.da

# Because of 0 km is accumulated by K faults, we can't discuss how many
more times radius change
# was accumulated by other fault populations during this time because
anything times 0 is 0
K.total.da <- 0

# Mansurian radius changes accommodated by M, C, and PT/T fault groups
followed by total Mansurian system change
st.4.M.da <- st.4.da * 1
st.3.M.da <- st.4.da * 3.25
st.12.M.da <- st.4.da * 14.9
M.total.da <- st.4.M.da + st.3.M.da + st.12.M.da
M.total.da

# Strain associated with this change
M.total.da/2443*100
```

```
# Calorian radius changes accommodated by C and PT/T fault groups
followed by total Calorian system change
st.3.C.da <- st.3.da * 1 - st.3.M.da
st.12.C.da <- st.3.C.da * 4.627
C.total.limit.da <- 3- M.total.da
C.total.da <- st.3.C.da + st.12.C.da
C.total.da

# Strain associated with this change
C.total.da/2443*100

# Pre-tolstojan and Tolstojan radius changes
st.12.PTT.da <- st.12.da - st.12.M.da - st.12.C.da
# Note that because the radius change slightly exceeds 5.1 km, there
must not be any change left to accumulate during the PT/T
P.total <- 0


# Using the upper bound of 3.6 km of radius change, note that bounds
are symmetric -------------------------

st.12.u.da <- 3.6*per.12faults
st.3.u.da <- 3.6*per.3faults
st.4.u.da <-3.6*per.4faults
st.5.u.da <- 3.6*per.5faults
# If interested, subtract the original st.x values from these values to
find error bounds

# Mansurian UB radius change
st.4.M.u.da <- st.4.u.da * 1
st.3.M.u.da <- st.4.u.da * 3.25
st.12.M.u.da <- st.4.u.da * 14.9
M.total.u.da <- st.4.M.u.da + st.3.M.u.da + st.12.M.u.da
# If interested, subtract the original st.x.M values from these values
to find error bounds

# Strain associated with this change
M.total.u.da/2443.6*100

# Calorian UB radius change
st.3.C.u.da <- st.3.u.da * 1 - st.3.M.u.da
st.12.C.u.da <- st.3.C.u.da * 4.627
C.total.u.da <- st.12.C.u.da + st.3.C.u.da
# If interested, subtract the original st.x.C values from these values
to find error bounds

# Strain associated with this change
C.total.u.da/2443.6*100

# Pre-tolstojan and Tolstojan Change
P.total <- 0


# DiAchille radius change estimates w S+G time systems
#LOWER BOUNDS
lb.c.strainrate.dasg <- 0.9566274/(.65*s*2442.4)
lb.m.strainrate.dasg <- 1.494386/(2.25*s*2442.4)
```

```
lb.k.strainrate.dasg <- 0

#ESTIMATE
c.strainrate.dasg <- C.total.da/(.65*s*2443)
c.strainrate.dasg
m.strainrate.dasg <- M.total.da/(2.25*s*2443)
m.strainrate.dasg

#UPPER BOUNDS
ub.c.strainrate.dasg <- C.total.u.da/(.65*s*2443.6)
ub.m.strainrate.dasg <- M.total.u.da/(2.25*s*2443.6)
# If interested, subtract the original x.strainrate values from these
values to find error bounds

deachille_sg_c <- c(lb.c.strainrate.dasg, c.strainrate.dasg,
ub.c.strainrate.dasg)
deachille_sg_m <- c(lb.m.strainrate.dasg, m.strainrate.dasg,
ub.m.strainrate.dasg)

# DiAchille radius change estimates w Banks time systems
#LOWER BOUNDS
lb.c.strainrate.dab <- 0.9566274/(2*s*2442.4)
lb.m.strainrate.dab <- 1.494386/(1.6*s*2442.4)
lb.k.strainrate.dab <- 0

#ESTIMATE
c.strainrate.dab <- C.total.da/(2*s*2443)
c.strainrate.dab
m.strainrate.dab <- M.total.da/(1.6*s*2443)
m.strainrate.dab

#UPPER BOUNDS
ub.c.strainrate.dab <- C.total.u.da/(2*s*2443.6)
ub.m.strainrate.dab <- M.total.u.da/(1.6*s*2443.6)
# If interested, subtract the original x.strainrate values from these
values to find error bounds

deachille_banks_c <- c(lb.c.strainrate.dab, c.strainrate.dab,
ub.c.strainrate.dab)
deachille_banks_m <- c(lb.m.strainrate.dab, m.strainrate.dab,
ub.m.strainrate.dab)


# ----------------------------------------------------------------------
--------------------------
# Watters 2013 radius change estimates with 1, 1.25, and 1.5 as total
changes
# Assuming 3 km of radius change (radius change accommodated by faults
in PT/T, C, M, and K terrains)
st.12.w <- 1.25*per.12faults
st.3.w <- 1.25*per.3faults
st.4.w <-1.25*per.4faults
st.5.w <- 1.25*per.5faults

st.12.w
st.3.w
st.4.w
```

```
st.5.w

# Because of 0 km is accumulated by K faults, we can't discuss how many
more times radius change
# was accumulated by other fault populations during this time because
anything times 0 is 0
K.total.w <- 0

# Mansurian radius changes accommodated by M, C, and PT/T fault groups
followed by total Mansurian system change
st.4.M.w <- st.4.w * 1
st.3.M.w <- st.4.w * 3.25
st.12.M.w <- st.4.w * 14.9
M.total.w <- st.4.M.w + st.3.M.w + st.12.M.w
M.total.w

# Strain associated with this change
M.total.w/2441.25*100

# Calorian radius changes accommodated by C and PT/T fault groups
followed by total Calorian system change
st.3.C.w <- st.3.w * 1 - st.3.M.w
st.12.C.w <- st.3.C.w * 4.627
C.total.limit.w <- 1.25 - M.total.w
C.total.w <- st.3.C.w + st.12.C.w
C.total.w

# Strain associated with this change
C.total.w/2441.25*100

# Pre-tolstojan and Tolstojan radius changes
st.12.PTT.w <- st.12.w - st.12.M.w - st.12.C.w
# Note that because the radius change slightly exceeds 1.25 km, there
must not be any change left to accumulate during the PT/T
P.total <- 0


# Using the upper bound of 1.5 km of radius change, note that bounds
are symmetric -------------------------

st.12.u.w <- 1.5*per.12faults
st.3.u.w <- 1.5*per.3faults
st.4.u.w <-1.5*per.4faults
st.5.u.w <- 1.5*per.5faults
# If interested, subtract the original st.x values from these values to
find error bounds

# Mansurian UB radius change
st.4.M.u.w <- st.4.u.w * 1
st.3.M.u.w <- st.4.u.w * 3.25
st.12.M.u.w <- st.4.u.w * 14.9
M.total.u.w <- st.4.M.u.w + st.3.M.u.w + st.12.M.u.w
# If interested, subtract the original st.x.M values from these values
to find error bounds

# Strain associated with this change
M.total.u.w/2441.5*100
```

```
# Calorian UB radius change
st.3.C.u.w <- st.3.u.w * 1 - st.3.M.u.w
st.12.C.u.w <- st.3.C.u.w * 4.627
C.total.u.w <- st.12.C.u.w + st.3.C.u.w
# If interested, subtract the original st.x.C values from these values
to find error bounds

# Strain associated with this change
C.total.u.w/2441.5*100

# Pre-tolstojan and Tolstojan Change
P.total.w <- 0


# Watters 2013 radius change estimates w S+G time systems
#LOWER BOUNDS
lb.c.strainrate.wsg <- 0.3985947/(.65*s*2441)
lb.m.strainrate.wsg <- 0.6226609/(2.25*s*2441)
lb.k.strainrate.wsg <- 0

#ESTIMATE
c.strainrate.wsg <- C.total.w/(.65*s*2441.25)
c.strainrate.wsg
m.strainrate.wsg <- M.total.w/(2.25*s*2441.25)
m.strainrate.wsg

#UPPER BOUNDS
ub.c.strainrate.wsg <- C.total.u.w/(.65*s*2441.5)
ub.m.strainrate.wsg <- M.total.u.w/(2.25*s*2441.5)
# If interested, subtract the original x.strainrate values from these
values to find error bounds

watters_sg_c <- c(lb.c.strainrate.wsg, c.strainrate.wsg,
ub.c.strainrate.wsg)
watters_sg_m <- c(lb.m.strainrate.wsg, m.strainrate.wsg,
ub.m.strainrate.wsg)

# Watters radius change estimates w Banks time systems
#LOWER BOUNDS
lb.c.strainrate.wb <- 0.3985947/(2*s*2441)
lb.m.strainrate.wb <- 0.6226609/(1.6*s*2441)
lb.k.strainrate.wb <- 0

#ESTIMATE
c.strainrate.wb <- C.total.w/(2*s*2441.25)
c.strainrate.wb
m.strainrate.wb <- M.total.w/(1.6*s*2441.25)
m.strainrate.wb

#UPPER BOUNDS
ub.c.strainrate.wb <- C.total.u.w/(2*s*2441.5)
ub.m.strainrate.wb <- M.total.u.w/(1.6*s*2441.5)
# If interested, subtract the original x.strainrate values from these
values to find error bounds
```

```
watters_banks_c <- c(lb.c.strainrate.wb, c.strainrate.wb,
ub.c.strainrate.wb)
watters_banks_m <- c(lb.m.strainrate.wb, m.strainrate.wb,
ub.m.strainrate.wb)



# ------------------- Rough Figure 2 components -------------------
#OLD STRAIN RATE PLOT
#strains <- c(excessprecal.strain.rate, lb.c.strainrate, c.strainrate,
ub.c.strainrate, lb.m.strainrate, m.strainrate, ub.m.strainrate, 0)
#ages <- c(4.250, 3.575,3.575,3.575, 2.125,2.125, 2.125,0.500)
#plot(ages, strains, xlim=c(4.5, 0), ylim=c(0,6*10^-20), xaxs='i',
yaxs='i', xlab='Ga', ylab='strain rate')
#NEW STRAIN RATE PLOT
strain_rates <- c(excessprecal.strain.rate.lb21,
excessprecal.strain.rate.ub21, excessprecal.strain.rate.lb14,
excessprecal.strain.rate.ub14)
ages <- c(4.5, 3.91, 4.5, 3.91)
plot(ages, strain_rates, xlim=c(4.5, 0), ylim=c(0,2.8*10^-19),
xaxs='i', yaxs='i', xlab='Ga', ylab='strain rate')
ages_sg_cm <- c(3.9, 3.9, 3.9, 3.25, 3.25, 3.25)
ages_banks_cm <- c(1.9, 1.9, 1.9, 0.3, 0.3, 0.3)


strain_rates_byrnesg <- c(byrne_sg_c, byrne_sg_m)
points(ages_sg_cm, strain_rates_byrnesg, col='black', pch=16)

strain_rates_byrnebanks <- c(byrne_banks_c, byrne_banks_m)
points(ages_banks_cm, strain_rates_byrnebanks, col='gray', pch=16)

strain_rates_dasg <- c(deachille_sg_c, deachille_sg_m)
points(ages_sg_cm, strain_rates_dasg, col='black', pch=12)

strain_rates_dabanks <- c(deachille_banks_c, deachille_banks_m)
points(ages_banks_cm, strain_rates_dabanks, col='gray', pch=12)

strain_rates_w <- c(watters_sg_c, watters_sg_m)
points(ages_sg_cm, strain_rates_w, col='black', pch=24)

strain_rates_wbanks <- c(watters_banks_c, watters_banks_m)
points(ages_banks_cm, strain_rates_wbanks, col='gray', pch=24)

dev.new()
# Radius change plots
ages2 <- c(3.9, 3.9, 3.9, 3.25, 3.25, 3.25, 1, 1, 1, 0)
M.total.l <- M.total - (M.total.u - M.total)
radius <- c(2443.1, 2445.1, 2447.1, 2443.1-(3.1-M.total.l), 2445.1-
(5.1-M.total), 2447.1-(7.1-M.total.u), 2440, 2440, 2440, 2440)
#th.radius.1 comes from Grott 2011 figure 1b and th.radius.2 comes from
figure 1c
th.ages.1 <- c(0, 2.5, 3.5, 4.25, 4.5)
th.radius.1 <- c(2440, 2444, 2445, 2445, 2446)
th.ages.2 <- c(0, 1.5, 3, 4.25, 4.375, 4.5)
th.radius.2 <- c(2440, 2442.3, 2444.2, 2442.3, 2441.8, 2442.3)

plot(ages2, radius, xlim=c(4.5, 0), xlab='Ga', ylab='radius (km)')
```

```
points(th.ages.1, th.radius.1, col='red')
points(th.ages.2, th.radius.2, col='blue')

# Cumulative strain graphs (as percentages)
# use ages 2
dev.new()
C.total.l <- C.total - (C.total.u - C.total)
percentages <- c(0,0,0, C.total.l/3.1*100, C.total/5.1*100,
C.total.u/7.1*100, 100, 100, 100, 100)

th.per.1 <- c(100, 33.3, 16.67, 16.67, 0)
th.ages.3 <- c(0, 1.5, 3, 4.5)
th.per.2 <- c(100, 54.8, 0, 0)

plot(ages2, percentages, xlim=c(4.5, 0), xlab='Ga', ylab='cumulative %
contraction')
points(th.ages.1, th.per.1, col='red')
points(th.ages.3, th.per.2, col='blue')

# ---------------- Implications, Fault growth rate and Slip rate ------
# Examples
# Adventure Rupes 1.3 km relief, 270 km long, D=1.863 km
# Enterprise Rupes of 3 km relief, 800 km long, D=6 km (1.3/sin(30))

# Surface area of Mercury
A <- 4*pi*(2440^2)

short.advent <- cos(pi/6)*1.863*270

#Strain associated with adv rupes
st.advent <- short.advent / A

time.advent <- st.advent/c.strainrate
time.advent.ub <- st.advent/ub.c.strainrate

# convert from seconds to billion years

time.advent.gy <- time.advent/31556952000000000
time.advent.years <- time.advent.gy * 1000000000

time.advent.gy.ub <- time.advent.ub/31556952000000000
time.advent.years.ub <- time.advent.gy.ub * 1000000000

time.advent.years
time.advent.years - time.advent.years.ub

# Enterprise Rupes Calculation
short.ent <- cos(pi/6)*6*800
st.ent <- short.ent/A
time.ent <- st.ent/c.strainrate
time.ent.ub <- st.ent/ub.c.strainrate

time.ent.gy <- time.ent/31556952000000000
time.ent.years <- time.ent.gy * 1000000000

time.ent.gy.ub <- time.ent.ub/31556952000000000
time.ent.years.ub <- time.ent.gy.ub * 1000000000
```

```
time.ent.years
time.ent.years - time.ent.years.ub

#Slip rates
D.advent.mm <- 1.863 * 10^6
D.ent.mm <- 6 * 10^6

slip.advent <- D.advent.mm/time.advent.years
slip.ent <- D.ent.mm/time.ent.years

slip.advent
slip.ent


#------------------ Uniformity of fault data ---------------------
#setwd('~/Documents/Paper/revision')
#set your own working directory

#Midpoints should contain the file of fault midpoints which can be
retrieved from Byrne et al, 2014
#midpoints <- read.table('mid_w_coords.csv', sep=',', header=TRUE)

# Q is the number of quadrilaterals per hemisphere
# z is the number of zones, taken from figure 2 in Bailey 195x

Q <- 81
z <- 5
lat_int <- 90/z

lats <- seq(-90, 90, lat_int)

# We need the number of quadrilaterals per latitude band (we have 5
bands or zones)
q1 <- round(Q*sin(18 * pi/180), digits=0)

q2 <- round(Q*(sin(36*pi/180) - sin(18 * pi/180)), digits=0)

q3 <- round(Q*(sin(54*pi/180) - sin(36 * pi/180)), digits=0)

q4 <- round(Q*(sin(72*pi/180) - sin(54 * pi/180)), digits=0)

q5 <- round(Q*(sin(90*pi/180) - sin(72 * pi/180)), digits=0)

q1
q2
q3
q4
q5

#Where do the longitudes that break up those quadrilaterals fall?


lons1 <- seq(-180, 180, 360/q1)
lons2 <- seq(-180, 180, 360/q2)
lons3 <- seq(-180, 180, 360/q3)
lons4 <- seq(-180, 180, 360/q4)
```

```
lons5 <- seq(-180, 180, 360/q5)

mpsn5 <- which(midpoints$latitude >= lats[1] & midpoints$latitude <
lats[2])
cn5 <- cut(midpoints[mpsn5, ]$longitude, breaks=lons5)
cn5 <- sqrt(as.matrix(table(cn5)))

mpsn4 <- which(midpoints$latitude >= lats[2] & midpoints$latitude <
lats[3])
cn4 <- cut(midpoints[mpsn4, ]$longitude, breaks=lons4)
cn4 <- sqrt(as.matrix(table(cn4)))

mpsn3 <- which(midpoints$latitude >= lats[3] & midpoints$latitude <
lats[4])
cn3 <- cut(midpoints[mpsn3, ]$longitude, breaks=lons3)
cn3 <- sqrt(as.matrix(table(cn3)))

mpsn2 <- which(midpoints$latitude >= lats[4] & midpoints$latitude <
lats[5])
cn2 <- cut(midpoints[mpsn2, ]$longitude, breaks=lons2)
cn2 <- sqrt(as.matrix(table(cn2)))

mpsn1 <- which(midpoints$latitude >= lats[5] & midpoints$latitude <
lats[6])
cn1 <- cut(midpoints[mpsn1, ]$longitude, breaks=lons1)
cn1 <- sqrt(as.matrix(table(cn1)))

mpsp1 <- which(midpoints$latitude >= lats[6] & midpoints$latitude <
lats[7])
cp1 <- cut(midpoints[mpsp1, ]$longitude, breaks=lons1)
cp1 <- sqrt(as.matrix(table(cp1)))

mpsp2 <- which(midpoints$latitude >= lats[7] & midpoints$latitude <
lats[8])
cp2 <- cut(midpoints[mpsp2, ]$longitude, breaks=lons2)
cp2 <- sqrt(as.matrix(table(cp2)))

mpsp3 <- which(midpoints$latitude >= lats[8] & midpoints$latitude <
lats[9])
cp3 <- cut(midpoints[mpsp3, ]$longitude, breaks=lons3)
cp3 <- sqrt(as.matrix(table(cp3)))

mpsp4 <- which(midpoints$latitude >= lats[9] & midpoints$latitude <
lats[10])
cp4 <- cut(midpoints[mpsp4, ]$longitude, breaks=lons4)
cp4 <- sqrt(as.matrix(table(cp4)))

mpsp5 <- which(midpoints$latitude >= lats[10] & midpoints$latitude <=
lats[11])
cp5 <- cut(midpoints[mpsp5, ]$longitude, breaks=lons5)
cp5 <- sqrt(as.matrix(table(cp5)))

all_counts <- c(cn5, cn4, cn3, cn2, cn1, cp1, cp2, cp3, cp4, cp5)

sd(all_counts)
```

```
#  Note that out of 164 bins, there is only 11 bins of data that
contain rooted counts greater than 10 (outliers).


get_fake_sd <- function() {

u <- runif(6024, 0, 1)
v <- runif(6024, 0, 1)

theta <- 2*pi*u - pi
phi <- acos((2*v)-1) - (pi/2)

theta <- as.matrix(theta)
phi <- as.matrix(phi)

fake <- cbind(phi*180/pi, theta*180/pi)
colnames(fake) <- c('latitude', 'longitude')
fake <- as.data.frame(fake)

mpsn5 <- which(fake$latitude >= lats[1] & fake$latitude < lats[2])
cn5 <- cut(fake[mpsn5, ]$longitude, breaks=lons5)
cn5 <- sqrt(as.matrix(table(cn5)))

mpsn4 <- which(fake$latitude >= lats[2] & fake$latitude < lats[3])
cn4 <- cut(fake[mpsn4, ]$longitude, breaks=lons4)
cn4 <- sqrt(as.matrix(table(cn4)))

mpsn3 <- which(fake$latitude >= lats[3] & fake$latitude < lats[4])
cn3 <- cut(fake[mpsn3, ]$longitude, breaks=lons3)
cn3 <- sqrt(as.matrix(table(cn3)))

mpsn2 <- which(fake$latitude >= lats[4] & fake$latitude < lats[5])
cn2 <- cut(fake[mpsn2, ]$longitude, breaks=lons2)
cn2 <- sqrt(as.matrix(table(cn2)))

mpsn1 <- which(fake$latitude >= lats[5] & fake$latitude < lats[6])
cn1 <- cut(fake[mpsn1, ]$longitude, breaks=lons1)
cn1 <- sqrt(as.matrix(table(cn1)))

mpsp1 <- which(fake$latitude >= lats[6] & fake$latitude < lats[7])
cp1 <- cut(fake[mpsp1, ]$longitude, breaks=lons1)
cp1 <- sqrt(as.matrix(table(cp1)))

mpsp2 <- which(fake$latitude >= lats[7] & fake$latitude < lats[8])
cp2 <- cut(fake[mpsp2, ]$longitude, breaks=lons2)
cp2 <- sqrt(as.matrix(table(cp2)))

mpsp3 <- which(fake$latitude >= lats[8] & fake$latitude < lats[9])
cp3 <- cut(fake[mpsp3, ]$longitude, breaks=lons3)
cp3 <- sqrt(as.matrix(table(cp3)))

mpsp4 <- which(fake$latitude >= lats[9] & fake$latitude < lats[10])
cp4 <- cut(fake[mpsp4, ]$longitude, breaks=lons4)
cp4 <- sqrt(as.matrix(table(cp4)))

mpsp5 <- which(fake$latitude >= lats[10] & fake$latitude <= lats[11])
cp5 <- cut(fake[mpsp5, ]$longitude, breaks=lons5)
```

```
cp5 <- sqrt(as.matrix(table(cp5)))

all_counts <- c(cn5, cn4, cn3, cn2, cn1, cp1, cp2, cp3, cp4, cp5)

return(sd(all_counts))

}

#Expect a long run-time here. We did 100,000 repetitions to be safe,
but closer to 100 would have been sufficient.
fake_sds <- replicate(100000, get_fake_sd())
```

APPENDIX C

SUPPLEMENTARY R CODE, CHAPTER 3

```
#In running this code, you should set your own working directory and
include the text files published with the paper as supplementary
materials (AFH2, AFH4, AFH5, AFNP, and their FT equivalents in that
directory.
#setwd('~/Documents/project2/vertices')
AFH2 <- read.table('AFH2.txt', sep=',', header=TRUE)
AFH4 <- read.table('AFH4.txt', sep=',', header=TRUE)
AFH5 <- read.table('AFH5.txt', sep=',', header=TRUE)
AFNP <- read.table('AFNP.txt', sep=',', header=TRUE)

FTH2 <- read.table('FTH2.txt', sep=',', header=TRUE)
FTH4 <- read.table('FTH4.txt', sep=',', header=TRUE)
FTH5 <- read.table('FTH5.txt', sep=',', header=TRUE)
FTNP <- read.table('FTNP.txt', sep=',', header=TRUE)

# The following lines remove segments of structure from the anticline
files that are parallel to structures in the faults files so that these
structures are not more heavily weighted.
H2_duplicates <- unique(FTH2$FID)
H2_duplicates <- as.vector(H2_duplicates, mode='numeric')
AFH2.culled <- AFH2[! AFH2$FID %in% H2_duplicates, ]
FTH2 <- FTH2[-4]
H2 <- rbind(AFH2.culled, FTH2)
```

The following lines remove segments of structure from the anticline files that are parallel to structures in the faults files so that these structures are not more heavily weighted.

```
H4_duplicates <- unique(FTH4$FID)
H4_duplicates <- as.vector(H4_duplicates, mode='numeric')
AFH4.culled <- AFH4[! AFH4$FID %in% H4_duplicates, ]
FTH4 <- FTH4[-4]
H4 <- rbind(AFH4.culled, FTH4)
```

The following lines remove segments of structure from the anticline files that are parallel to structures in the faults files so that these structures are not more heavily weighted.

```
H5_duplicates <- unique(FTH5$FID)
H5_duplicates <- as.vector(H5_duplicates, mode='numeric')
AFH5.culled <- AFH5[! AFH5$FID %in% H5_duplicates, ]
FTH5 <- FTH5[-4]
H5 <- rbind(AFH5.culled, FTH5)
```

The following lines remove segments of structure from the anticline files that are parallel to structures in the faults files so that these structures are not more heavily weighted. They also insure that the segments considered are only contained in the smooth plains units, which are coded with a “0” in their terrain attribute.

```
FTNP.culled <- FTNP[FTNP$Terrain == '0', ]
NP_duplicates <- unique(FTNP$FID)
NP_duplicates <- as.vector(NP_duplicates, mode='numeric')
AFNP.culled <- AFNP[! AFNP$FID %in% NP_duplicates, ]
FTNP <- FTNP.culled[-3]
names(AFNP.culled) <- names(FTNP)
```

```
NP <- rbind(AFNP.culled, FTNP)

#Combine all of the segments that should be sorted into rose diagrams.
v <- rbind(H2, H4, H5, NP)
#install ggplot2 and its dependencies
# Export v to a csv
write.csv(v, 'v.csv', header=TRUE)

#Create and plot rose diagrmas
ggplot(v, mapping=aes(Longitude, Latitude)) +
coord_map('ortho', orientation=c(50, 45, 0)) +
stat_density2d(aes(fill=..level..), geom='polygon') +
theme_bw() +
geom_point(data=v, position='jitter', alpha= 0.2, color='white', cex=
0.1)



# Attempt to plot echelon by color
# Install plotrix and the dependencies
ggplot(v, mapping=aes(Longitude, Latitude)) +
coord_map('ortho', orientation=c(50, 45, 0)) +
stat_density2d(aes(alpha =..level..), geom='polygon') +
theme_bw() +
geom_point(data=v, position='jitter', alpha= 0.2,
color=color.scale(v$Echelon, c(0, 1, 1), c(1, 1, 0), c(1, 0, 1)), cex=
0.2)
```

APPENDIX D

SUPPLEMENTARY TEXT, CHAPTER 4

The following supplementary materials section contains details for each constructed cross section and a description of the data available to construct the cross section. An interpreted seismic profile in the Frenchman Hills is also included.

Additionally, two .kmz (Google Earth) files with georeferenced images and a .csv file with orientation measurements are also provided as supplementary materials in publication available in *Tectonophysics*. Not all 300 georeferenced images are included in the dataset, as the authors entered an agreement with the Department of the Army to only provide digital photographs of outcrop, not landscape, within the Yakima Training Center. Thus, landscape photos of western Saddle Mountains have not been included in this dataset.

For each cross section, basic information including the label number used in the text (e.g. S3), the name used during research, the end points (given in UTM zone 10), length (m), and depth (m) are included. More detailed information including well, geologic, structural, and seismic data are also included. For each cross section we include a short justification of why and how faults and folds were interpreted as well as a photo of the cross section taken from our interpretation software. Images of each cross section are available at the end of the text.

S1) Cross Section Details

Name: Royal Section

XY max: 770136.7, 5193380.7

XY min: 766987.5, 5180898.6

Length: 12482.0

Depth: 3149.2

Well Data

Number of wells	1
Names of wells	Strasser
Depth of wells	342 m
Distance of wells	~2000 m

Geologic Data

Faults	3 (2 at surface, 1 inferred)
Folds	2 (1 syncline to north, 1 anticline to S)
Units	EM, As, PR, R, Palouse, Ringold
Trends	Fold axis dips to north (asymmetry is to south). In order to maintain bed thickness across the top of the ridge, this had to be the case. The tighter part of the fold is where the anticline is marked on the geologic map, but overall the fold vergence is to the south. The syncline to the north is constrained by dip measurements in the Elephant Mt member.

Structural Data

Number of SDs	38
Max Distance	~ 4 km
Units	FS, R, PR, Rattlesnake Ridge, Quincy, Asotin, EM, Palouse,

Seismic Data

Available	No
Length	
Depth	

Were any faults drawn? How and why?

Three faults were drawn. Two are indicated on the geologic map as thrust faults that meet the surface on the northern side of the mountain. One is inferred due to the asymmetry of the mountain in this location. This asymmetry can be generated by slight displacement on the south-dipping master followed by additional displacement along a north dipping conjugate thrust. The steep dips of the faults are influenced by steep dips in the nearest seismic section and the use of strike lines to calculate fault dip at close to 70 degrees at the surface.

Were any folds drawn? How and why?

An asymmetric anticline and a symmetric syncline were drawn. The anticline was marked on the geologic map and conformed to SD measurements, but the syncline was purely supported by strike and dip measurements.

S2) Cross Section Details

Name: Section_dipdata2

XY max: 764512.8, 5195445.9

XY min: 761144.3, 5185880.5

Length: 10141.2

Well Data

Number of wells	1
Names of wells	AWS
Depth of wells	~450 m
Distance of wells	3.30 km

Geologic Data

Faults	3
Folds	3 major anticlines, 2 minor anticlines, and 1 mono-syncline
Units	Palouse, Pomona, Asotin, PR, R, FS, EM
Trends	The faults are again steep here and all thrusts, with a conjugate thrust dipping north. The tighter anticline on the north side can be achieved with a less dramatic shallowing of the fault dip at the base of the fault. This tightness is indicated by dip measurements. This structure is more asymmetric than the

	structure in the cross section to the east, suggesting a more developed conjugate thrust.

Structural Data

Number of SDs	38
Max Distance	6 km
Units	EM, PR, R, Asotin, FS

Seismic Data

Available	No
Length	
Depth	

Were any faults drawn? How and why?

Yes, 3. These faults were tied so closely to folding that they are both described together in the section below.

Were any folds drawn? How and why?

Yes, 3. The intermediate surface breaking fault indicated on the geologic map, and has a steep dip using strike lines for estimation (also supported by the steep dips of faults in the seismic section next to this section). Asymmetry in lower folds, but not in the upper folds indicates that this fault extends to depth, but the conjugate does not, and the resulting structure at the surface is a double anticline with shallow dips between hinges. The

upturned tight northern anticline is rotated by motion on the northern fault after displacement on the conjugate. Irregularities in the symmetric structure are attributed to stair-steps in the conjugate fault. The northernmost blind thrust produces a small anticline to the north.

S3) Cross Section Details

Name: Section_H456

XY max: 751535.2, 5196568.4

XY min: 749974.6, 5180004

Length: 16637.7

Well Data

Number of wells	4
Names of wells	Lemco, AF19, BN19, LL
Depth of wells	250 m, 4300 m, 5300 m, 105 m
Distance of wells	0 m, 1980 m, 1140 m, 2500 m

Geologic Data

Faults	2 major shallowing thrusts, 2 more minor thrusts, 1 very minor thrust, 1 conjugate thrust, one normal fault

Folds	1 south verging fold above the conjugate thrust, one anticline in the basement verging north above the deepest fault, one north verging anticline above the intermediate depth major thrust, a broad anticline corresponding to sequential folding above two thrusts, two synclines (one associated with the footwall of a minor thrust and one associated with the down-dropped block of the normal fault. There is also a very broad syncline trailing the south verging anticline.
Units	Pomona, PR, Mabton (not mapped), Palouse, Rosa, FS, GR, EM
Trends	The geometry broadens and the folds open as faults shallow and possible disconnect from deeper structure. Models show that more gently dipping faults produce more open folding. Some rotation may be present on the front minor thrust, linking it to the previous cross section (dipdata2) where roation occurred above the frontal thrust.

Structural Data

Number of SDs	16
Max Distance	5100 m
Units	EM, rattlesnake ridge, Rosa, FS, PR, Asotin

Seismic Data

Available	Yes
Length	9500 m
Depth	9700 m

Were any faults drawn? How and why?

Yes, three of the faults on the northern portion of the section (including the normal fault) were noted on the geologic map. These faults were noted by strike lines as having steep dips. The normal fault dipped to the north. One north verging fault was added where a small anticline needed to be accounted for and where the quality of reflection changed in the seismic data. Regions of seismic data with horizontal reflections were assumed to be in the footwall of faults or in the hanging-wall of faults where they were deposited as horizontal syntectonic or post-tectonic sediment. Dipping reflections were interpreted to be folded horizons in hanging walls. Contacts between continuous dark reflections and static (not near the edges of the seismic data) were interpreted to be faults as well where footwall rock produced dark reflections and deformed hanging wall rock produced chaotic reflections. These transitions also corresponded to predicted folds from strike and dip data, map data, and geologic data.

Were any folds drawn? How and why?

A broad north verging anticline trailed by a southern syncline is the main feature, with smaller anticlines produced by a conjugate thrust and by secondary thrusts with rotation.

S4) Cross Section Details

Name: Section 4

XY max: 741132.5, 5198936.1

XY min: 739687.2, 5180274.8

Length: 18717.2

Well Data

Number of wells	2
Names of wells	Royal, Ponderosa
Depth of wells	~ 150 m each
Distance of wells	3.5 and 3.7 km

Geologic Data

Faults	Only 1 fault was reported on the 100k geologic map, but I drew 5 north verging thrusts total.
Folds	There are three broad synclines, and five anticlines at the surface. These anticlines appear tighter at the surface than at depth, where some are very broad.
Units	Ringold, Rosa, FS, GR, Asotin, Pomona, EM, PR, Palouse
Trends	The faults all verge north, with between 40 and 60 degree dips to the south. The deepest fault roots to -7500 m, and shallows, but actually has relatively little displacement when compared with the upper thrusts. The upper thrusts all produce recognizable anticlines at the surface narrower than those at

	depth. There is almost certainly a conjugate fault, but I was not able to identify displacement in the seismic data. Thus, I have not drawn this fault.

Structural Data

Number of SDs	20
Max Distance	~3500 m
Units	GR, Ringold, Missoula, Asotin, PR, FS, Rosa,

Seismic Data

Available	Yes
Length	18717 m
Depth	9 km

Were any faults drawn? How and why?

Five thrust faults were drawn. Three were identified by clear offset of bold and characteristically identifiable reflections. The reflections were recognizable by their thickness and continuity. The deepest fault was easiest to identify as it corresponded to clearly identifiable offset in multiple bold reflections. The second deepest fault was identifiable in three bold offset layers, and the third deepest thrust fault could be identified in two bold offsets, and propagated below an anticline identified in the seismic profile. Reflections in the seismic profile clearly indicated folded layers. The northernmost thrust fault is relatively shallow and corresponds to two offset layers and

one shallow anticline in the surface. The only thrust fault that mapped to the surface (and is the shallowest thrust fault) shows the greatest displacement close to the surface. Although it has a similar dip to the surrounding thrusts, the lack of deep offset reflections indicates that the fault does not continue downward.

Were any folds drawn? How and why?

Folds were drawn where curved reflections were present in the seismic section or where the strike and dips indicated an anticline. There are two notable anticlines that need addressing apart from what was written above concerning the faults. (1) An anticline that verges south indicates the presence of a southward verging fault; however none was identified. The southern vergence (indicated by strike and dip measurements) is attributed to geologic data only and in the subsurface, reflections appear mostly horizontal. If a fault is present, it is shallow. The other anticline worth mentioning is the north verging anticline associated with the fault mapped at the surface. This fault shows maximum displacement at 500m depth and offsets reflections down to 2000 m depth.

S5) Cross Section Details

Name: East Columbia

XY max: 736889.7, 5194612.6 m

XY min: 735735, 5181414.1 m

Length: 13248.9 m

Well Data

Number of wells	1
Names of wells	Mathews
Depth of wells	67 m
Distance of wells	~700 m

Geologic Data

Faults	Two faults are marked at the surface, and one additional fault may need to be drawn below the southernmost anticline. A normal fault is at the top of the anticline. I do not show slip on the normal fault and this fault is not drawn deep because it is nearly perpendicular to the section and the fault trace at the surface is short.
Folds	The northernmost anticline is large and mostly eroded. The southernmost anticline is a mono-anticline and transitions from nearly horizontal behind the northern anticline to about a 10 degree dip to the south. This fold transitions into a mono-syncline in the Missoula deposits, which is present in all of the eastern cross sections.
Units	EM, Asotin, GR, PR, Rosa, FS
Trends	This is the easternmost cross section where the fold structure is more asymmetric than symmetric.

Structural Data

Number of SDs	35
Max Distance	
Units	

Seismic Data

Available	No
Length	
Depth	

Were any faults drawn? How and why?

One main fault was drawn, and this fault was drawn to -2000 m depth with a stair-step geometry. Fault bend folds produce fold hinges near each change in dip of their fault plane, and the dip of the plane reflects the dip in the bedding. Thus I drew a shallow ramps below the nearly horizontal mono-anticline northern limb, and bent this ramp into a flat below the hinge of that fold. I steepened the plane dip below the northernmost anticline because steeper planes produce more exaggerated folding.

Were any folds drawn? How and why?

Two anticlines were drawn based on (1) being marked on the geologic map and (2) presence of strike and dips. Using these strike and dips to constrain the dips of the units produces two distinct folds, and supports the southernmost fold being interpreted as a mono-anticline.

S6) Cross Section Details

Name: West Columbia

XY max: 731874, 5194739.7

XY min: 728908.5, 5175108.2

Length: 19854.2 m

Well Data

Number of wells	0
Names of wells	
Depth of wells	
Distance of wells	

Geologic Data

Faults	4 thrust faults (one major, three minor)
Folds	A major mono-anticline is predicted north of the frontal thrust, and a minor anticline is predicted between two of the minor northern thrusts. Two mono-anticlines are mapped south of the frontal and minor thrusts, and these bends were observed in the field.
Units	Rosa, Priest Rapids, FS, GR
Trends	

Structural Data

Number of SDs	49
Max Distance	4100 m
Units	FS, Asotin, GR, Rosa, PR

Seismic Data

Available	No
Length	
Depth	

Were any faults drawn? How and why?

Four faults were drawn. All four were northward verging thrusts. The frontal thrust was most northern. Its dip was determined by strike-line calculations and by the modelling tool. Bends in anticlines within the southern limb of the fold indicated that this fault had a stair step structure. Strike-line calculations show a minimum dip of 45 degrees. The two minor northern thrusts were not recognized in the field, and do not accommodate enough slip to juxtapose different flow units. Their dips were calculated from strike lines and ranged from 38 to 45 degrees. The southern thrust must have a noticeable amount of offset because the older Rosa units are next to younger Priest Rapids units, and both have nearly horizontal dips. The displacement may be between 100 and 200 m.

Were any folds drawn? How and why?

Folds were drawn based on strike and dip data collected in the field. There is one discrepancy in the fold as I have drawn it and how it is suggested on the 24k and 100k geologic maps. On these maps, bedding is indicated to be vertical or nearly vertical in front (to the north) of the main fold axis. I nearly mapped the units this way when I was in the field until I realized that the fins protruding from the talus slopes were fins of basalt created through differential weathering and that the layers of columnar basalt in those fins were still nearly horizontal or gently dipping to the north. I therefore, do not draw the main northern fold with steeply dipping front slope, but leave the fold with a more gentle northern slope, as suggested by what I saw in the field.

S7) Cross Section Details

Name: Saddle West

*XY max:*725270.9 m, 5195526.2 m

*XY min:*715838.8 m, 5180554.2 m

Length: 17695.4 m

Well Data

Number of wells	0
Names of wells	
Depth of wells	
Distance of wells	

Geologic Data

Faults	2 thrust faults, 1 steeply dipping and 1 shallowly dipping
Folds	4 synclines and three anticlines are present on the geologic map
Units	FS, GR, Rosa, PR
Trends	The southern thrust has a very strange map pattern, and a shallow dip (as shallow as 8 degrees in some places). The anticlines and tight syncline between them above the northern frontal thrusts predicts that the northern frontal thrust has a stair-stepped shape and steep dip near the surface.

Structural Data

Number of SDs	41
Max Distance	3700 m
Units	GR, Rosa, FS

Seismic Data

Available	No
Length	
Depth	

Were any faults drawn? How and why?

Two faults were drawn to account for two main anticlines. Both were mapped on the geologic map. The more southern thrust roots near 1000 m depth, while the northern

thrust (which is part of the frontal thrust) reaches nearly 4000 m depth. The stair-step shape of the southern thrust accounts for the asymmetry of the anticline and the folds apparent vergence to the south. After reviewing the geologic map, this fault was calculated to dip between 8 and 35 degrees in places, and verged north. The northern frontal thrust has more complicated stair-step geometry. The near surface portion dips steeply to account for the upturned units and the calculated nearly 70-degree dip. A deep step near 1000 m depth is necessary for the model to produce the additional anticline-syncline pair behind the main anticline of the thrust. The gentle slope southward of the step suggests the fault gently flattens with depth.

Were any folds drawn? How and why?

Folds were drawn where suggested by strike and dip data. This produced a gentle anticline in the southern portion of the section and an unusual dual-anticline pair separated by a tight syncline in the northern half of the section south of the main thrust. The FS unit is shown at the highest elevation surrounded by GR, and the GR unit is shown to dip inward below this highest unit. The only way to produce the GR unit constrained by these dips and the surface geology is to have some form of double anticline-system at the top of the ridge. These anticlines are also noted on the geologic map.

S8) Cross Section Details

Name: Saddle_West2

*XY max:*719642.2 m, 5195425.0 m

*XY min:*715269.0 m, 5177885.2 m

*Length:*18076.8 m

Well Data

Number of wells	0
Names of wells	
Depth of wells	
Distance of wells	

Geologic Data

Faults	2 thrusts, one more southern and one more northern.
Folds	3 anticlines, two of which are marked on the geologic map, and a third, just south of the frontal thrust, which is apparent in adjacent sections of the geologic map. This anticline may not be marked here because the evidence has eroded away, and only the syncline is obvious at the surface. There is a syncline just north of the southernmost anticline and another syncline north of the main northern anticline. A syncline-anticline pair is present in the southern part of the section and is extremely broad and almost not noticeable.

	The geometry of these folds is constrained by surface geometry and maintaining bed thickness.
Units	FS, Rosa, GR
Trends	North verging asymmetric anticlines following synclines.

Structural Data

Number of SDs	34
Max Distance	2300 m
Units	GR, Rosa, FS

Seismic Data

Available	No
Length	
Depth	

Were any faults drawn? How and why?

The southern thrust was drawn as shallowly dipping south due to strike line calculations on the geologic map. This thrust was not continued up into the upper units, because this would imply that the fault was active and surface breaking when these units were deposited. I think it is more likely that the upper units were folded, not faulted. The northern thrust was drawn with a steeper dip, as calculations from the geologic map indicated a 28 to 52 degree dip. Dip was calculated to be steeper in deeply eroded valleys

and more shallow at the front of the ridge. Thus, I propose that the fault dip changes suddenly with depth. I also chose to continue the fault upward, cutting the younger units in the frontal thrust. This keeps continuity with its neighboring cross section. The offset seems drastic, but on the geologic map, the Rosa is not far from being adjacent to the GR, completely skipping over the very thick FS unit. This implies much displacement. I did try to propagate the fault below the surface, but in the context of the Rosa being so close by, the thickness of the FS unit made this impossible.

Were any folds drawn? How and why?

The southernmost anticline, associated with the southern thrust is drawn above the low angle thrust with a north verging sense of asymmetry. The syncline to the north, just south of the frontal thrust is the same (likely) as the one in Saddle West, and the anticline just south of this is related to the northernmost anticlines in the Saddle West section. It is as if these two anticlines merge into one anticline in Saddle West 2.

S9) Cross Section Details

Name: Badger Pocket

*XY max:*718857.5 m, 5199347.4 m

*XY min:*700420.0 m, 5179575.5 m

Length: 27034.5

Well Data

Number of wells	0
Names of wells	
Depth of wells	
Distance of wells	

Geologic Data

Faults	3 north-verging, south dipping thrusts
Folds	2 syncline-anticline pairs
Units	GR, FS, Rosa
Trends	Two north verging anticlines with synclines to their north. The northern anticline is broader, and further deformed by a second thrust.

Structural Data

Number of SDs	41
Max Distance	4500 m
Units	FS, Rosa, GR, Vantage

Seismic Data

Available	No
Length	
Depth	

Were any faults drawn? How and why?

Three faults were drawn, all of which were indicated on the geologic map. The dip of the southernmost fault is shallow, between 11 and 15 degrees as calculated by strike-line method. The geometry of the fault was constructed using the fault geometry tool, and is similar to the southernmost thrusts in saddle west 2 and saddle west. Although on the geologic map these faults do not connect, their tips are very near each other, suggesting that they connect at depth. Except for their tips, the strikes and dips of the faults are very similar. The intermediate fault is drawn shallower than the other two faults. Its dip was calculated to be between 35 and 44.9 degrees, and may not represent much displacement. Although significant erosion has taken place behind the fault exposing younger units, slivers of GR are left unmoved and indicate that the fault is not major. It may have contributed to the rotation and formation of a broad anticline-syncline pair. The main thrust was calculated to dip near 29 degrees, and using the horizons from fault modelling tool, was produced with a fault depth of 4000 m.

Were any folds drawn? How and why?

The left edge (southern edge) of the cross section is characterized by a very broad anticline, which is unrelated to the broad anticline is saddlewest2. The broad syncline directly north of this anticline is related to the syncline in saddlewest2, although in this section, it is not mapped. An anticline was drawn above the southern thrust, as indicated on the geologic map and by my strike and dip measurements. Though the thrust breaks

the surface, I do not interpret that it faulted the upper part of the Frenchman springs, as this unit is mapped adjacent to the fault with a syncline, suggesting that the upper layers were folded, not faulted. An anticline syncline pair was drawn behind the main thrust.The syncline dips steeply just north of the fault. This is drawn in this way because the Rosa outcrops near by (so it was necessary to bring the Rosa close to the surface) and because the GR also outcrops nearby. The Rosa only outcrops just north of the fault, but not farther North, indicating that the GR can rise toward the surface farther away from the fault.

S10) Cross Section Details

Name: Section85266

XY max: 709217.4 m, 5202303.9 m

XY min: 692057.3 m, 5180418.2 m

Length: 27811.0 m

Well Data

Number of wells	4
Names of wells	Yakima 1-33, Burbank, Eastwood, 2335BN
Depth of wells	-4000 m, 340 m, 480 m, -3050 m
Distance of wells	1800 m, 1840 m, 3000 m, 1300 m

Geologic Data

Faults	4 shown on the map, 2 additional, all thrusts
Folds	3 anticlines, 3 syclines
Units	Rosa, FS, GR, Umtanum, PR
Trends	This cross section crosses the Kittitas Valley floor. The northern end of the cross section is near the frontal thrust surface break, except that in this particular location, the surface break of the thrust is mapped at a strange angle, dipping into a valley. I believe this may represent a separate thrust that links to main, frontal thrust, which is below the surface at the location of the cross section. This is also justified by the change in dip between the portion of the fault within the valley and the rest of the long, frontal thrust. On the south side of the valley, there is an anticline syncline pair against a south verging thrust, followed to the south by exposures of FS and GR. Because the GR is exposed in the valleys and some of the peaks, we can calculate the thickness of the FS. Another anticline-syncline pair follows above a non-surface breaking thrust fault.

Structural Data

Number of SDs	41
Max Distance	6000 m
Units	GR, Vantage, FS, Rosa, GR Umt

Seismic Data

Available	Yes
Length	11.5 km
Depth	9 km

Were any faults drawn? How and why?

Six faults were drawn. The two southernmost thrust faults verge away from each other, and their surface breaks are only 700 m apart. While the northern of these two faults (dipping south) is only 5.8 km long, the southern fault connects as a back thrust behind the main thrust of Manastash Ridge. Thus, this fault was drawn to a deeper depth and showed more displacement. The displacement was also necessary, as constrained by surface geology and two wells (Burbank and Yakima 1-33). The next thrust fault to the north, the frontal thrust of Manastash Ridge, does not break the surface. This fault actually connects Umtanum Ridge and Manastash Ridge as being underlain by a connected fault system. The dip and shape of the fault were determined using the fault building tools. Offset along the fault was predicted by surface geology and constrained by well data. The geologic map showed an extreme thinning of the FS, which is a 400 m thick unit. A more likely explanation is that a fault is present at depth, and the upper portion of the syncline and FS is exposed. The three northern faults are inter-fingering. Oppositely verging thrusts may have contributed to the formation of the Kittitas Valley. Both thrusts were constrained by strike line method calculation and the fault-building model. The northernmost fault is the frontal thrust which does not break the surface but is evidenced by folds and offset reflections in the seismic section.

Were any folds drawn? How and why?

A broad anticline was drawn above the Yakima 1-33 well as indicated by geologic map data. The Umtanum Ridge anticline was also drawn, and with a syncline just to its north. Above the northern thrusts, I also interpreted anticlines. While all folds were constrained by well data, strike and dips, and surface geology, the northernmost anticlines were also visible in the seismic section.

F1) Cross Section Details

Name: Frenchman Hills

XY max: 742284.9 m, 5209005 m

XY min: 742724.6 m, 5194454.2 m

Length: 15088 m (14000 km interpretable)

Depth: 9700 m

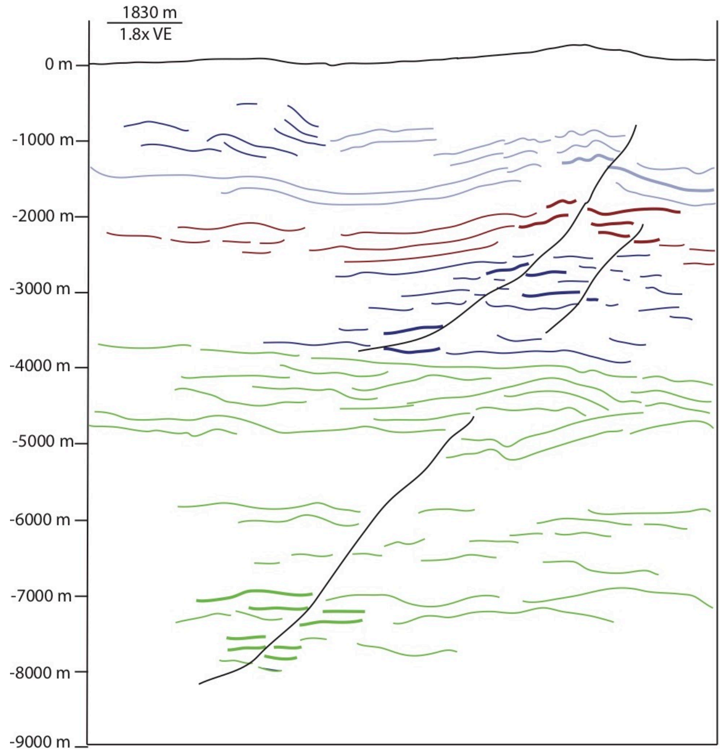

For this cross section, our goal was only to interpret the general structure (faults and folds) within the seismic data. Strong amplitude, continuous seismic reflections that played a key role in interpretation have been outlined in color and bolded where offset reflections were especially apparent. Black lines indicate interpreted thrust faults. Colors do not correlate with specific strata, but were solely used to help guide the author's eye during interpretation.

<u>Cross section Images</u>

Other datasets that accompany the cross sections, such as displacement along faults for each rock unit, are available with the article when published in *Tectonophysics.*

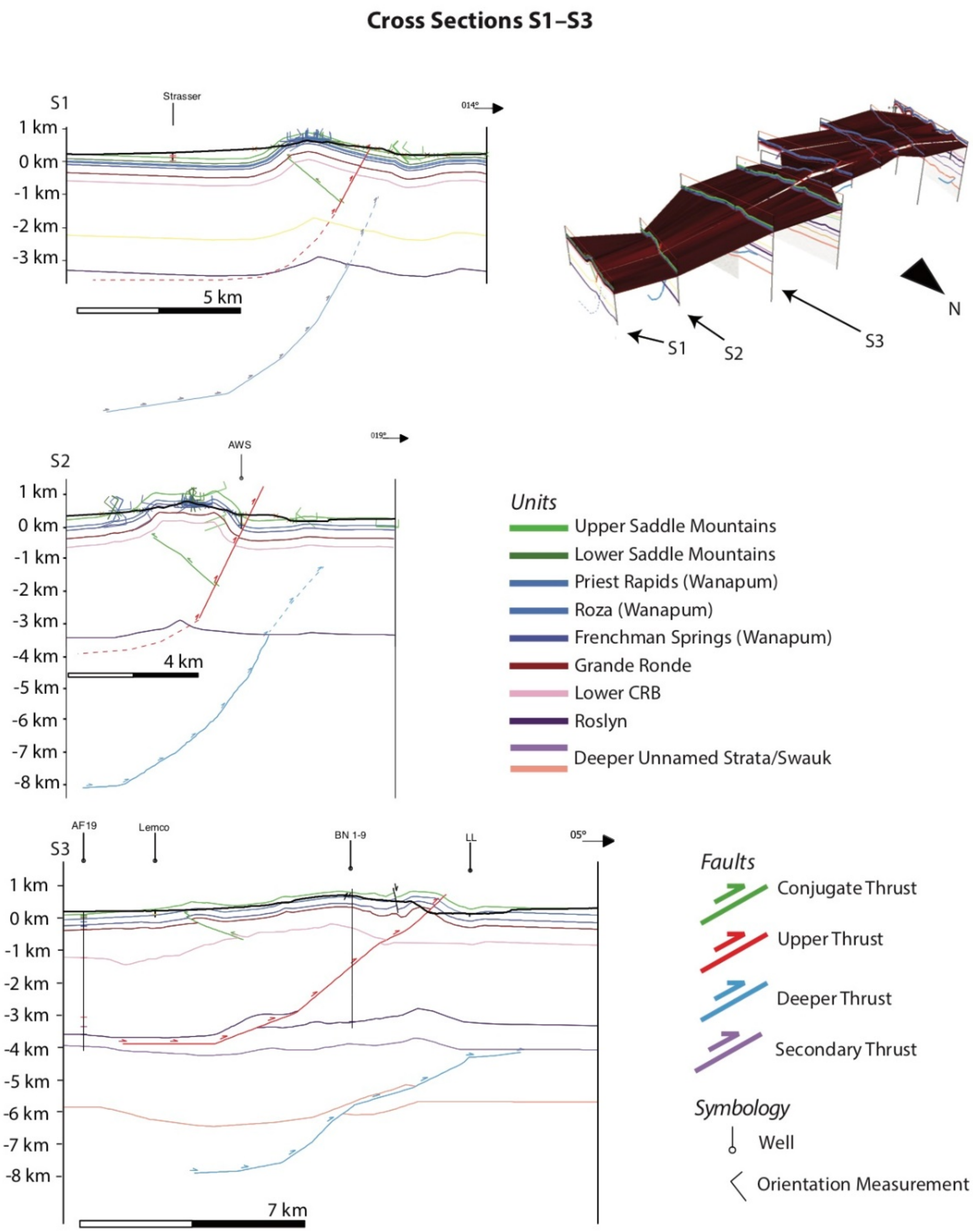

Cross Sections S4–S6

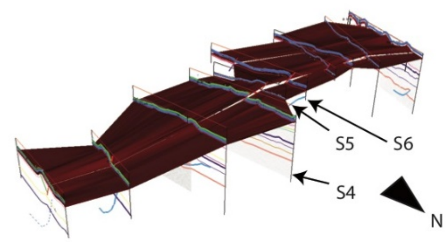

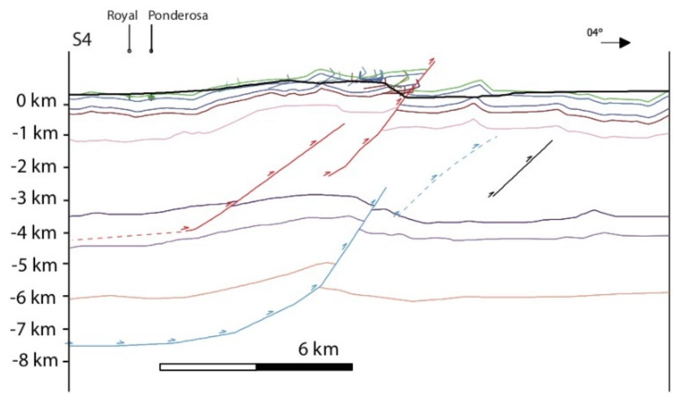

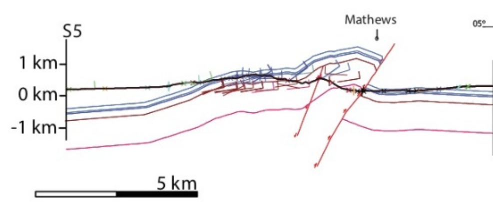

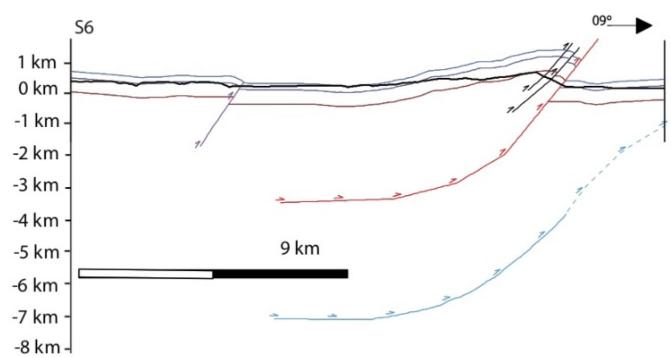

Cross Sections S7–S10